

ISTANBUL TECHNICAL UNIVERSITY ★ GRADUATE SCHOOL OF SCIENCE
ENGINEERING AND TECHNOLOGY

NANOCOMPOSITE SCAFFOLDS CONTAINING METAL NANOPARTICLES



Ph.D. THESIS

Ayşen AKTÜRK

Department of Metallurgical and Materials Engineering

Metallurgical and Materials Engineering Programme

SEPTEMBER 2020

ISTANBUL TECHNICAL UNIVERSITY ★ GRADUATE SCHOOL OF SCIENCE
ENGINEERING AND TECHNOLOGY

NANOCOMPOSITE SCAFFOLDS CONTAINING METAL NANOPARTICLES



Ph.D. THESIS

Ayşen AKTÜRK
(506112413)

Department of Metallurgical and Materials Engineering

Metallurgical and Materials Engineering Programme

Thesis Advisor: Prof. Dr. Gültekin GÖLLER
Thesis Co-Advisor: Prof. Dr. Melek EROL TAYGUN

SEPTEMBER 2020

İSTANBUL TEKNİK ÜNİVERSİTESİ ★ FEN BİLİMLERİ ENSTİTÜSÜ

METAL NANOTANECİK İÇEREN NANOKOMPOZİT YAPI İSKELELERİ



DOKTORA TEZİ

**Ayşen AKTÜRK
(506112413)**

Metalurji ve Malzeme Mühendisliği Anabilim Dalı

Metalurji ve Malzeme Mühendisliği Programı

**Tez Danışmanı: Prof. Dr. Gültekin GÖLLER
Eş Danışman: Prof. Dr. Melek EROL TAYGUN**

EYLÜL 2020

Ayşen Aktürk, a Ph.D. student of İTÜ Graduate School of Science Engineering and Technology student ID 506112413, successfully defended the dissertation entitled “NANOCOMPOSITE SCAFFOLDS CONTAINING METAL NANOPARTICLES”, which she prepared after fulfilling the requirements specified in the associated legislations, before the jury whose signatures are below.

Thesis Advisor : **Prof. Dr. Gültekin GÖLLER**
İstanbul Technical University

Co-advisor : **Prof. Dr. Melek EROL TAYGUN**
İstanbul Technical University

Jury Members : **Assoc. Prof. Dr. İpek AKIN KARADAYI**.....
İstanbul Technical University

Prof. Dr. Sebahattin GÜRME
İstanbul Technical University

Prof. Dr. Ülker BEKER

Assoc. Prof. Dr. Gökçen ALTUN ÇİFTÇİOĞLU.....
Marmara University

Prof. Dr. Cengiz KAYA
Sabancı University

Date of Submission : 25 August 2020

Date of Defense : 23 September 2020





To my mother,



FOREWORD

I would like to thank my advisor Prof. Dr. Gültekin GÖLLER for his guidance, belief and support throughout my work. I express my gratitude to my co-advisor Prof. Dr. Melek EROL TAYGUN. This thesis would not have existed without her support and guidance. I would like to present my special thanks to Prof. Dr. Sadriye KÜÇÜKBAYRAK. She was the one who gives me the opportunity to do this Ph.D. thesis and never gave up her support during this study.

I extend my sincere thanks to my Ph.D. thesis committee members, Prof. Dr. Ülker BEKER, Assoc. Prof. Dr. İpek AKIN KARADAYI, and Assoc. Prof. Dr. Gökçen Alev ALTUN ÇİFTÇİOĞLU.

Throughout this study, many people did not withhold their support in characterization studies. I would like to thank Assoc. Prof. Dr. Funda KARBANCIOĞLU GÜLER for all the supports. I believe it was a great chance to study with her. I would like to thank M. Sc. Esra ENGİN, Dr. Serkan GÜÇLÜ, Assoc. Prof. Dr. Bihter ZEYTUNCU and Chemical Engineer Oğuz ORHUN TEBER, Res. Asst. Sıddıka MERTDİNÇ and Hüseyin SEZER for the characterization studies. I am grateful to Asst. Prof. Dr. Didem OVALI, Asst. Prof. Dr. Mustafa GÜVEN GÖK and Dr. Barış YAVAŞ for their support and patience. I am also grateful to my friends Dr. Nilay BAYLAN, M. Sc. Özge ÇELEBİCAN, Res. Asst. Hava ÇAVUŞOĞLU VATANSEVER, Res. Asst. Ahsen ÜNAL and Dr. Alper YURTTAŞ for their support and friendship.

I would thank Istanbul Technical University Research Fund (BAP project: 38881) for the financial support.

During this study, I experienced the biggest loss in my life. My mother was my driving force in my life. I hope she watches that I have finished my Ph.D. study. Of course, I am very grateful to my father and brother for their love, support and patience.

September 2020

Ayşen AKTÜRK
(M.Sc. Chemical Engineer)



TABLE OF CONTENTS

	<u>Page</u>
FOREWORD	ix
TABLE OF CONTENTS	xi
ABBREVIATIONS	xiii
SYMBOLS	xv
LIST OF TABLES	xvii
LIST OF FIGURES	xix
SUMMARY	xxi
ÖZET	xxiii
1. INTRODUCTION	1
2. FABRICATION OF ANTIBACTERIAL POLYVINYLALCOHOL NANOCOMPOSITE MATS WITH SOLUBLE STARCH COATED SILVER NANOPARTICLES	7
2.1 Introduction	7
2.2 Materials and Methods	10
2.2.1 Materials.....	10
2.2.2 Preparation of silver nanoparticles.....	10
2.2.3 Preparation of electrospinning solutions	11
2.2.4 Electrospinning	11
2.2.5 Cross-linking treatment.....	11
2.2.6 Assessment of the release of Ag ⁺ ions from nanofiber mats	11
2.2.7 Antibacterial activity	12
2.2.8 Characterization studies	12
2.3 Results and Discussion.....	13
2.3.1 Silver nanoparticle production	13
2.3.2 Morphology and structural analysis of nanofibers.....	15
2.3.3 Selection of the suitable crosslinking treatment	17
2.3.4 Antibacterial activity of nanofibers.....	20
2.4 Conclusions	23
3. OPTIMIZATION OF THE ELECTROSPINNING PROCESS VARIABLES FOR GELATIN/ SILVER NANOPARTICLES/BIOACTIVE GLASS NANOCOMPOSITES FOR BONE TISSUE ENGINEERING	25
3.1 Introduction	25
3.2 Materials and Methods	27
3.2.1 Materials.....	27
3.2.2 Preparation of silver nanoparticles.....	27
3.2.3 Preparation of bioactive glass particles.....	27
3.2.4 Preparation of electrospinning solution	27
3.2.5 Electrospinning	28
3.2.6 Antibacterial tests.....	28
3.2.7 Box-Behnken design experiments	28
3.2.8 Characterization of bioactive glass and nanofiber membranes.....	30
3.3 Results and Discussion.....	30

3.3.1 Preliminary studies.....	30
3.3.2 Development of RSM models.....	32
3.3.3 Verification of experimental and model data.....	36
3.3.4 Effect of electrospinning parameters on the nanofiber diameter.....	37
3.3.5 Surface plots.....	39
3.3.6 Optimization of Gt/Ag NPs/BG nanofiber membrane fabrication.....	39
3.3.7 Characterization of 45S5 bioglass particles.....	40
3.3.8 Characterization of optimized Gt/Ag-NPs/BG nanofiber membrane.....	41
3.4 Conclusion.....	46
4. SYNTHESIS AND ANTIFUNGAL ACTIVITY OF SOLUBLE STARCH AND SODIUM ALGINATE CAPPED COPPER NANOPARTICLES	47
4.1 Introduction.....	47
4.2 Materials and Methods.....	50
4.2.1 Materials.....	50
4.2.2 Synthesis of Cu NPs.....	50
4.2.3 Characterization of Cu NPs.....	50
4.2.4 Antifungal activity of Cu NPs.....	51
4.3 Results and Discussion.....	52
4.3.1 Phase analysis.....	52
4.3.2 Morphology of Cu NPs.....	53
4.3.3 Thermal analysis.....	55
4.3.4 FTIR analysis.....	58
4.3.5 Stability of Cu nanoparticles.....	61
4.3.6 Antifungal activity of CuA NPs and CuS NPs.....	62
4.4 Conclusions.....	63
5. OPTIMIZATION OF THE FABRICATION OF POLYCAPROLACTONE NANOFIBER MATS DOPED WITH BIOACTIVE GLASS AND COPPER NANOPARTICLES FOR TISSUE ENGINEERING APPLICATIONS.....	65
5.1 Introduction.....	65
5.2 Materials and Methods.....	67
5.2.1 Preparation of copper nanoparticles.....	67
5.2.2 Preparation of bioactive glass particles.....	67
5.2.3 Preparation of PCL/Cu NP/BG solutions and electrospinning process....	68
5.2.4 Design of electrospinning experiments by Box Behnken Design (BBD).	68
5.2.5 Morphological characterization of nanofiber mats.....	69
5.2.6 Cell behavior of fibroblast cells on nanofibrous mats.....	69
5.2.7 Stability of nanofiber mats in simulated body fluid.....	70
5.3 Results and Discussion.....	71
5.3.1 Statistical results.....	71
5.3.2 Validation of experimental and predicted model data.....	72
5.3.3 Effect of parameters on the response.....	73
5.3.4 Response surface analysis.....	75
5.3.5 Cytocompatibility study.....	76
5.3.6 In vitro mineralization study and Cu ions release assessment.....	78
5.4 Conclusions.....	81
6. CONCLUSIONS.....	83
REFERENCES.....	87
CURRICULUM VITAE.....	111

ABBREVIATIONS

ANOVA	: Analysis of Variance
BBD	: Box Behnken Design
BG	: Bioactive Glass
CuA NPs	: Sodium Alginate Capped Copper Nanoparticles
CuS NPs	: Soluble Starch Capped Copper Nanoparticles
DLS	: Dynamic Light Scattering
DTA	: Differential Thermal Analysis
ECM	: Extracellular Matrix
FE-SEM	: Field Emission Scanning Electron Microscope
FTIR	: Fourier Transform Infrared Spectroscopy
GA	: Glutaraldehyde
Gt	: Gelatin
ICP	: Inductively Coupled Plasma Mass Spectrometer
RSM	: Response Surface Methodology
S-Ag NPs	: Soluble Starch Coated Silver Nanoparticles
SEM	: Scanning Electron Microscope
TGA	: Thermogravimetric Analysis
WST-1	: Water Soluble Tetrazolium Assay
XRD	: X-Ray Diffraction Analyzer



SYMBOLS

A₁	: Absorbance of Fungal Cells in the Control
A₂	: Absorbance of Fungal Cells in the Test Medium
C₀	: Constant Term
C_i	: Constant Coefficient of Linear Factor Term
C_{ii}	: Constant Coefficient of Quadratic Factor Term
C_{ij}	: Constant Coefficient of Interactive Factor Term
X_i	: Linear Factors of the Uncoded Variables
X_{ii}	: Quadratic Factors of the Uncoded Variables
X_{ij}	: Interactive Factors of the Uncoded Variables
y	: Average Fiber Diameter



LIST OF TABLES

	<u>Page</u>
Table 2.1 : The inhibition zone measurements taken after 24 h for 5S-Ag NPs loaded PVA, 7.5S-Ag NPs loaded PVA, and 10S-Ag NPs loaded PVA nanofiber mats against <i>E.coli</i> and <i>S.aureus</i>	21
Table 3.1 : The BBD design experiments and results.	34
Table 3.2 : ANOVA results for the experimental response at different levels.	34
Table 3.3 : ANOVA results after elimination of insignificant terms for the experimental response at different levels.	35
Table 3.4 : Results of validation experiments.	37
Table 3.5 : Degradation temperatures of Gt, Gt/Ag-NPs and Gt/Ag-NPs/BG nanofiber membranes.	45
Table 4.1 : Thermal analysis of soluble starch, CuS NPs, sodium alginate (NaAlg) and CuA NPs under N ₂ atmosphere.	56
Table 4.2 : Thermal analysis of soluble starch, CuS NPs, sodium alginate and CuA NPs under air atmosphere.	57
Table 5.1 : The BBD design experiments and results.	69
Table 5.2 : ANOVA results for the experimental response at different levels.	71
Table 5.3 : ANOVA results after elimination of insignificant terms for the experimental response at different levels.	72



LIST OF FIGURES

	<u>Page</u>
Figure 2.1 : (a) XRD pattern, (b) FE-SEM image and (c) DLS analysis of silver nanoparticles solution synthesized in soluble starch (S-Ag NPs).	14
Figure 2.2 : SEM images of neat PVA (a), 5S-Ag NPs loaded PVA (b), 7.5S-Ag NPs loaded PVA (c) and 10S-Ag NPs loaded PVA (d) nanofiber mats.	15
Figure 2.3 : (a) XRD pattern of the 10S-Ag NPs loaded PVA nanofiber mat, (b) FTIR spectra of neat PVA (i) and the 10S-Ag NPs loaded PVA nanofiber mats.	16
Figure 2.4 : SEM images of the uncrosslinked 10S-Ag NPs loaded PVA nanofiber mat (a), the crosslinked 10S-Ag NPs loaded PVA nanofiber mat by heat treatment (b), and glutaraldehyde immersion (c).....	18
Figure 2.5 : FTIR spectra of neat 10S-Ag/PVA (a), the cross-linked 10S-Ag/PVA by heat treatment (b), and the cross-linked 10S-Ag/PVA by glutaraldehyde immersion (c).	18
Figure 2.6 : Ag ⁺ ion releases of 10S-Ag NPs loaded PVA nanofiber mats cross-linked by heat treatment and by glutaraldehyde immersion in the SBF..	19
Figure 2.7 : SEM images of the cross-linked 10S-Ag/PVA nanocomposite by heat treatment, and the cross-linked 10S-Ag/PVA nanocomposite by glutaraldehyde immersion in different time intervals in SBF.	20
Figure 2.8 : Images of antibacterial activity of 5S-Ag NPs loaded PVA, 7.5S-Ag NPs loaded PVA and 10S-Ag NPs loaded PVA nanofiber mats crosslinked by glutaraldehyde immersion against <i>S. aureus</i> and <i>E. coli</i> .	22
Figure 3.1 : SEM images of Gt/Ag-NPs nanofibers electrospun in mixtures of Ag-NPs solution and acetic acid at volumetric ratios of 10/90 (a), 20/80 (b) and 30/70 (c) and antibacterial tests of Gt/Ag-NPs nanofibers electrospun in mixtures of Ag-NPs solution and acetic acid at volumetric ratios of 10/90 (d), 20/80 (e) and 30/70 (f).	31
Figure 3.2 : SEM images of Gt/Ag-NPs/BG nanocomposites in various electrospinning conditions based on Box-Behnken-design.....	33
Figure 3.3 : Plot of model predicted fiber diameter against experimental fiber diameter (a) and normal probability plot (b).	36
Figure 3.4 : The effect of applied voltage (a-c), flow rate (d-f) and TCD (g-i) on the diameter of electrospun Gt/Ag-NPs/BG composite nanofibers for different experimental conditions.	38
Figure 3.5 : Surface plots of the response variable (fiber diameter(nm)) for various electrospinning parameters (two factor at a time). (applied voltage-flowrate, applied voltage-TCD, flowrate-TCD).	39
Figure 3.6 : Characterization studies of BG particles including SEM analysis (a), EDS analysis (b), FTIR measurements (c), DTA analysis (d), and XRD analysis (e).	41
Figure 3.7 : (a) SEM image of the optimized Gt/Ag-NPs/ BG nanofiber membrane; (b) XRD analysis of the optimized Gt/Ag-NPs/ BG nanofiber membrane; (c) FTIR spectra of Gt nanofiber membrane (i),	

Gt/Ag-NPs nanofiber membrane (ii) and Gt/Ag-NPs/BG nanofiber membrane (iii); (d) EDS analysis of the optimized Gt/Ag-NPs/ BG nanofiber membrane.	43
Figure 3.8 : (a) TGA of Gt nanofiber membrane (i), Gt/Ag-NPs nanofiber membrane (ii) and Gt/Ag-NPs/BG nanofiber membrane (iii), (b) DTG of Gt nanofiber membrane (i), Gt/Ag-NPs nanofiber membrane (ii) and Gt/Ag-NPs/BG nanofiber membrane (iii).....	44
Figure 3.9 : Stress-strain curves of the optimized nanofiber membranes.	46
Figure 4.1 : XRD analysis of CuA NPs (a) and CuS NPs (b).	52
Figure 4.2 : SEM images of CuA NPs (a) and CuS NPs (d); Particle size distribution histograms of CuA NPs (b) and CuS NPs (e); DLS analysis of CuA NPs (c) and CuS NPs (f).	53
Figure 4.3 : DTG and DTA curves of soluble starch (a), sodium alginate (b), CuS NPs (c) and (d) CuA NPs under N ₂ atmosphere.	56
Figure 4.4 : (a) TGA of CuS NPs (i) and CuA NPs (ii) under N ₂ atmosphere, TGA of CuS NPs (iii) and CuA NPs under air atmosphere; (b) DTG and DTA analysis of CuS NPs under air atmospheres; (c) DTG and DTA analysis of CuA NPs under air atmosphere.	57
Figure 4.5 : FTIR spectra of soluble starch (a), CuS NPs (b); sodium alginate (c) and CuA NPs (d).	59
Figure 4.6 : XRD of CuA NPs (a) and CuS NPs (b) kept under open air environment for 6 weeks.	61
Figure 4.7 : Percentage inhibition of <i>C.albicans</i> (a) and <i>C.krusei</i> (b) by Cu NPs.	62
Figure 4.8 : Growth of <i>C. krusei</i> and <i>C. albicans</i> on Agar medium loaded with CuA NPs and CuS NPs microdilution test samples at different concentrations (4, 2, 1, 0.5, 0.25 mg/mL).	63
Figure 5.1 : (a) Plot of model predicted fiber diameter against experimental fiber diameter, and (b) normal probability plot.	73
Figure 5.2 : Perturbation plot for fabrication of PCL/BG/ Cu NPs nanofibers as a function of PCL concentration (a), Cu NPs ratio (b), and BG ratio (c)..	74
Figure 5.3 : Interaction plots between the formulation variables of PCL concentration, Cu NPs ratio, BG ratio.	75
Figure 5.4 : Contour and surface plots of the response variable (fiber diameter, nm) for different experimental factors(two factor at a time): a) PCL concentration and Cu NPs ratio, b) Cu NPs ratio and BG ratio.....	77
Figure 5.5 : The WST-1 assay absorbance graph of the PCL nanofiber mats containing BG and Cu NPs after 24, 48 and 72 hours.	78
Figure 5.6 : The SEM images of the PCL nanofiber mats containing BG and Cu NPs after WST-1 for 72 hours.	80
Figure 5.7 : (a) Copper ions release of the PCL-BG-0.025Cu nanofiber mat in SBF for different time intervals and (b) XRD graph of the PCL-BG-0.025Cu nanofiber mat immersed in SBF for 28 days.	81
Figure 5.8 : SEM images of the PCL/BG/0.025 Cu NPs nanofiber mat immersed in SBF for 1 day (a), 7 days (b), 14 days (c), and 28 days.	81

NANOCOMPOSITE SCAFFOLDS CONTAINING METAL NANOPARTICLES

SUMMARY

Nowadays metal–polymer nanocomposites are the subject of increased interest due to their potential to combine the features of polymers with inorganic materials. Specifically, the combination of a natural polymer (biopolymer) and metal nanoparticles is highly appealing because of the individual antibacterial activity of the metal nanoparticle components, and the possibility to generate a biodegradable and biocompatible composite. The bioactivity of composites can be achieved by using bioactive inorganics such as hydroxyapatite, bioactive glasses. This study aims to combine metal-polymer-bioactive glass to fabricate new nanocomposite materials by using electrospinning method. For this purpose, polymer solutions containing bioactive glass (45S5) particles and/or metal nanoparticles (silver and copper nanoparticles) were prepared and then, they were electrospun into nanofibers under the relevant process conditions (i.e., solution concentration, applied voltage, tip-to-collector distance, flow rate, and etc.). Gelatin as a natural polymer and poly (ϵ -caprolactone) (PCL) and polyvinyl alcohol (PVA) as synthetic polymers were employed in the experimental studies. Bioactive glass used in this study was fabricated by classical melt-derived method, while copper and silver nanoparticles were prepared by using biopolymers (soluble starch and sodium alginate) as the capping agents. Membranes were produced with a certain fiber diameter by using Box-Behnken design, which is a statistical experimental design method and characterization studies of these membranes were carried out. The crystalline structure of the produced bioactive glasses and metal nanoparticles were analyzed by X-ray diffraction (XRD) technique. Moreover, the surface morphology and the crystalline structure of the electrospun nanofibrous scaffolds were examined by the help of a scanning electron microscope (SEM) and X-ray diffractometer (XRD). Changes in the structures of the obtained nanoparticles and membranes were detected by using Fourier-transform infrared spectroscopy (FTIR), Thermogravimetric analysis (TGA) was performed to determine the thermal behavior of nanofiber membranes and copper nanoparticles. Furthermore, the in vitro degradation behavior of the scaffolds were investigated by using simulated body fluid (SBF). In addition, the bioactivity and the biocompatibility of the nanofibrous scaffolds were also investigated through in-vitro bioactivity tests and cell culture studies. Moreover, the antibacterial or antifungal effects of the obtained nanoparticles and membranes were determined. Finally, therapeutic ions release from the nanofibrous scaffolds were investigated by using inductively coupled plasma optical emission spectrometry (ICP-OES). As a result of all these characterization studies, it was concluded that the nanofiber membranes obtained in this study have a potential for tissue engineering applications.



METAL NANOTANECİK İÇEREN NANOKOMPOZİT YAPI İSKELELERİ

ÖZET

Doku mühendisliği, doku ve organ kayıplarında kimya, fizik, mühendislik ve klinik bilimlerin prensiplerinin geliştirilmesine ve uygulanmasına dayanan ve vücuttaki doku işlevlerini restore eden, sürdüren veya geliştiren yapı iskelesi adı verilen biyolojik fonksiyonel ikameler tasarlamayı amaçlayan disiplinlerarası bir alandır. Bu yaklaşımda; kolajen, glikozaminoglikanlar, retiküler lifler ve elastin dahil olmak üzere nano ölçekli boyutlardaki lifli yapılardan oluşan hücrelerin ve hücre dışı matrisinin etkileşimleri kritik öneme sahiptir. Hücre dışı matris, hücrelere belirli bir dokuya farklılaşmaları için yapısal bütünlük ve biyokimyasal bilgi sağlar. Doku mühendisliğinin araştırma alanı, hücre dışı matris moleküllerini taklit eden belirli mekanik, biyolojik ve mimari özelliklere sahip yapı iskelelerinin üretimine odaklanmıştır.

Doku mühendisliği iskelesi, hücre dışı matrisin yerini alan ve doğal bir hücre dışı matrisin oluşumu sırasında hücrelere geçici destek sağlayan üç boyutlu bir biyomalzemedir. Bir doku iskelesi tasarlanırken, üretilen malzemenin biyoyumluluğu, biyobozunurluğu, sterilize edilebilirliği ve doğal dokuya benzeyen mekanik özellikler gibi gereksinimleri sağlanmalıdır. Ek olarak, birbirine bağlı gözenek yapısı ve yüksek gözeneklilikleri; hücre bağlanmasını, çoğalmasını ve farklılaşmasını, ayrıca besinlerin taşınmasını ve atık olarak çıkan iskele bozunma ürünlerinin difüzyonunu sağlamalıdır.

Doğal insan dokularının hücre dışı matrisi, makromoleküller (yani glikozaminoglikanlar, kollajen, elastin, proteoglikanlar, retiküler lifler ve polisakkaritler) ve inorganik maddeden oluşmaktadır. Hücre dışı matris makromoleküllerinin mimarisi, uzunluk/çap oranı 100'den fazla olan ve 500 nm'den az olan lifli bir yapıya sahiptir. Bu nedenle, nanoliflerin gözenekli yapıları ile yüksek yüzey alanı/hacim oranını birleştiren nanolif matların kullanılması, doku mühendisliği uygulamalarında iskeleler geliştirmek için ideal bir seçimdir. Bugüne kadar, nanolif iskeleler, deri, kemik, kırık, bağ, iskelet kası, vasküler ve nöral dokular gibi doku mühendisliği uygulamaları için faz ayırma, kendi kendine düzenlenme ve elektrospinning dahil olmak üzere çeşitli tekniklerle üretilmektedir. Bu teknikler arasında elektrospinning, doku iskelesinde yaygın olarak kullanılan basit, ucuz ve çok yönlü bir yaklaşımdır.

İlaç salımı, yara iyileşmesi, kemik dokusu mühendisliği, üç boyutlu hücre substratı, cilt dokusu mühendisliği, tıbbi implantlar ve doku mühendisliği iskeleleri gibi spesifik uygulamalar için çeşitli sentetik polimerler, doğal polimerler ve bu polimerlerin diğer malzemelerle kombinasyonları kullanılarak elektrospinning yöntemi ile membranlar üretilmektedir. Sentetik polimerler bu uygulamalarda ana gövde görevi görür, çünkü ayarlanabilir mekanik özellikleri (viskoelastisite ve mukavemet), kolay işlenebilirliği, az maliyetli olmaları, kontrol edilebilir bozunma oranları ve farklı fizikokimyasal özellikleri sayesinde daha geniş bir özellik yelpazesi verecek şekilde uyarlanabilirler.

Biyomedikal uygulamalarda kullanılan tipik sentetik polimerler; poli (laktik asit) (PLA), poli (glikolik asit) (PGA), poli (ϵ -kaprolakton) (PCL), poli (hidroksil bütirat) (PHB), poli (laktik asit- ko-glikolik asit) (PLGA), poligliserol sebakat (PGS), poli (vinil alkol) (PVA), polietilen oksit, poliamid (PA) poliimid (PI), poli (ester amit) (PEA), poliüretan (PU), polietilen glikol (PEG) gibi polimerlerdir. Bununla birlikte, bu polimerlerin hücre tanıma özelliklerinin olmaması, biyoaktivite ve biyouyumluluk gibi özellikleri karşılayamamaları, bu polimerlerin biyomedikal amaçlarla uygulanmalarını kısıtlamaktadır. Aksine, doğal polimerler yeterli biyouyumluluk, hücre afinitesi, biyobozunurluk ve hidrofilitiklik gösterir. Polisakkaritler (nişasta, aljinat, kitin/kitosan, hiyalüronik asit türevleri, aljinat, bakteriyel selüloz, heparin, agaroz) ve proteinler (soya, kollajen, fibrin jelleri, ipek, jelatin, ipek fibroin, keratin, jelatin) doğal polimerler olarak doku mühendisliği uygulamalarında kullanılmaktadır. Bu polimerlerin dezavantajları düşük mekanik özellikleri ve yüksek bozunabilirlikleridir.

Bunlara ek olarak, sentetik biyomalzemelerin dayanıklılığını arttırmak için organik ve inorganik malzemelerden oluşan kompozit malzemeler üretilmektedir. Biyoaktif seramiklerin (hidroksiapatit (HA), kalsiyum fosfatlar, biyoaktif camlar ve biyoaktif cam bazlı kompozit malzemeler) ve nanokarbonların (karbon nanotüpler (CNT'ler), grafen oksit (GO), nanoelmaslar, fullerenerin) mekanik mukavemeti polimerlere göre daha yüksek olduğundan, polimerlerden üretilen nanolif iskelelerin mekanik özelliklerini geliştirmek için katkı malzemeleri olarak kullanılmaktadırlar. Geliştirilmiş mekanik özelliklere ek olarak, daha iyi bir hücre ekimi ve büyüme ortamı sağlayarak polimer matrisine iyi osteokondüktivite özellikleri katmaktadırlar.

Ayrıca, elektrospunlenmiş malzemeler morfolojileri nedeniyle geniş bir yüzey alanına sahip olduklarından, patojenik mikroorganizmaların yapışmasına ve üzerinde biyofilm oluşumuna yatkındırlar. Bu nedenle, metal oksit nanotanecikler (gümüş oksit (Ag_2O), çinko oksit (ZnO), titanyum dioksit (TiO_2), bakır oksit (CuO), demir (III) oksit (Fe_2O_3)), metalik nanotanecikler (gümüş, altın, bakır) ve doğal polimerler (kitosan) gibi bazı antimikrobiyal bileşenler nanolif malzemelerin antimikrobiyal performansını arttırmak için eklenmektedir.

Doku mühendisliği alanındaki elektrospinning uygulamalarında, doku mimarisine uygun yapılar elde edebilmek için elektrospinning çözelti, işlem ve ortam değişkenleri değiştirilerek kontrol edilebilir lif çaplı malzemeler üretebilmektedir. Elektrospinning değişkenleri çok çeşitli ve karmaşık olduğundan, elektrospinning işleminden önce proses çıktılarını tahmin etmek zordur. Bu nedenle, birçok araştırmacı bu değişkenleri belirlemede matematiksel ve istatistiksel yöntemler kullanılmıştır. Bu yöntemlerle, spesifik özelliklere sahip nanolif yapılar elde edilebilmektedir.

Bu bağlamda, bu doktora çalışmasında, iki farklı metalik nanotanecik (gümüş ve bakır nanotanecikler), kapaklama ve indirgeme ajanları olarak biyopolimerler (çözünabilir nişasta ve sodyum aljinat) ile sentezlenmiştir. Elde edilen nanotanecikler ve elektrospinning yöntemi kullanılarak doku mühendisliğinde kullanılacak yapı iskeleleri üretilmiş ve bu iskelelerin ayrıntılı karakterizasyonları yapılmıştır. Bu tezde yer verilen ilk makalede, çözünabilir nişasta ile kaplanmış gümüş (Ag) nanotaneciklerinin üretimine ait çalışmalara yer verilmiştir. Elde edilen Ag nanotanecikler polivinil alkol nanoliflere ilave edilmiş ve elde edilen nanoliflerin *E. coli* ve *S. aureus* bakterilerine karşı etkili olduğu tespit edilmiştir. Bu nanolif membranın yara sargı malzemesi olarak kullanılabilme potansiyeli Ag^+ iyon salım testleri ile belirlenmiştir. İkinci makalede, elde edilen Ag nanotaneciklerinin, kemik

doku mühendisliği uygulamalarında kullanılabilirliği belirlenmiştir. Biyopolimer olarak jelatin ve inorganik bileşen olarak 45S5 biyoaktif cam kullanılarak antibakteriyel özelliklere sahip nanolif membranlar elde edilmiştir. Elektrospinning işlem değişkenleri (voltaj, akış hızı ve uç toplayıcı mesafesi) kullanılarak kemik doku mühendisliği için uygun bir membran üretmek amaçlanmıştır. Nanolif boyutunu tahmin etmek için istatistiksel deneysel bir yöntem olan Box-Behnken tasarımı kullanılmış ve elektrospinning değişkenleri ile bir model oluşturulmuştur. Elde edilen nanolif yapısına ait karakterizasyon çalışmaları sonucunda, yapının trabeküler kemik uygulamaları için bir potansiyele sahip olduğu belirlenmiştir. Üçüncü makalede; bakır nanotanecikler, kapaklama maddeleri olarak çözünebilir nişasta ve sodyum aljinat kullanılarak üretilmiştir. Doku mühendisliği uygulamaları için, çözünebilir nişastanın sodyum aljinata göre daha uygun bir kapaklama maddesi olduğu sonucuna varılmıştır. Dördüncü makalede, PCL nanolif membranlara, çözünebilir nişastanın kapaklama maddesi olarak kullanıldığı bakır nanotanecik ve 45S5 biyoaktif cam katkısı yapılmıştır. Hem bu katkıların hem de polimer derişiminin etkisini belirleyebilmek için Box-Behnken tasarımı kullanılarak bir model elde edilmiştir. Kemik dokusu hücre dışı matrisi ile benzer lif boyutlarına sahip nanolif membranın üretimi için gerekli değişkenler belirlenmiştir. Yapılan sitotoksosite testleri ile yapıya katılması gereken Cu nanotanecik oranı tespit edilmiştir. Yapay vücut sıvısında bekletilmiş membranın biyoaktif özellikte olduğu ve Cu iyon salım sonuçlarının literatürle uyumlu olması nedenleriyle, elde edilen membranın kemik doku mühendisliği uygulamaları için bir potansiyele sahip olduğu düşünülmektedir.



1. INTRODUCTION

Tissue engineering is an interdisciplinary field based on the development and application of the principles of chemistry, physics, engineering and clinical sciences in cases of tissue and organ losses and aimed to design biological functional substitutes, called scaffold, that restore, maintain or improve tissue functions in the body [1-3]. In this approach, the interactions of cells and extracellular matrix (ECM) of cells composed of fibrous structures in the nanoscale range, including collagen, glycosaminoglycans, reticular fibers and elastin, are critical [3-5]. These structures provide the structural integrity and biochemical information to cells to differentiate into a specific tissue [3]. The research area of tissue engineering focused on the production of scaffolds with specific mechanical, biological and architectural properties imitating ECM molecules [1,5].

A tissue engineering scaffold is a three-dimensional biomaterial that replaces the ECM, providing temporary support for cells during the formation of a natural ECM [6,7]. Requirements such as biocompatibility, biodegradability, sterilizability, mechanical properties that resemble natural tissue should be provided to design a tissue scaffold [6]. In addition, their interconnected pores and high porosity should enable cell attachment, proliferation and differentiation, as well as transport of nutrients and diffusion of wastes and scaffolds' degradation products [7,8].

The ECM of natural human tissues consists of macromolecules (i.e., glycosaminoglycans, collagen, elastin, proteoglycans, reticular fibers and polysaccharides) and inorganic matter (connective tissue only) [3,4,9]. The architecture of ECM macromolecules possess a fibrous structure with a length/diameter ratio greater than 100 nm and a fiber diameter less than 500 nm [9-11]. Therefore, the use of nanofibrous mats that combines the high surface area to volume ratio of the nanofibers with their porous structure is an ideal choice to develop scaffolds for tissue engineering applications. To date, the nanofibrous scaffolds have been fabricated by different techniques including phase separation, self-assembly, and electrospinning for tissue engineering applications, such as skin, bone, cartilage,

ligament, skeletal muscle, vascular, and neural tissues [6,9-11]. Among these techniques, electrospinning is a simple, inexpensive and versatile approach commonly used in tissue scaffolding [6].

Various synthetic polymers, natural polymers and combinations of these polymers with other materials have been electrospun for specific applications such as drug delivery, wound healing, bone tissue engineering, three dimensional (3D) cell substrate, skin tissue engineering, medical implants and tissue engineering scaffolds [12-14]. Synthetic polymers act as the main body in electrospinning, because they can be adapted to give a wider range of properties, such as adjustable mechanical properties (viscoelasticity and strength), facile processing, cost effectiveness, controllable degradation rates and different physicochemical properties [5,14,15]. Typical synthetic polymers used in biomedical applications are poly(lactic acid) (PLA), poly(glycolic acid) (PGA), poly(ϵ -caprolactone) (PCL), poly (hydroxyl butyrate) (PHB), poly(lactic acid-co-glycolic acid) (PLGA), polyglycerol sebacate (PGS), poly(vinyl alcohol) (PVA), polyethylene oxide, polyamide (PA) polyimide (PI), poly(ester amide) (PEA), polyurethane (PU), polyethylene glycol (PEG) [1,5,14-16]. However, the absence of surface cell recognition sites of these polymers restricts their application in biomedical purposes because they cannot meet properties such as bioactivity and biocompatibility [15,17]. On the contrary, natural polymers show sufficient biocompatibility, cell affinity, biodegradability and hydrophilicity [15,17]. Polysaccharides (starch, alginate, chitin/chitosan, hyaluronic acid derivatives, alginate, bacterial cellulose, heparin, agarose) and proteins (soy, collagen, fibrin gels, silk, gelatin, silk fibroin, keratin, gelatin) are used as natural polymers in tissue engineering applications [1,5,15,16]. The disadvantages of these polymers are their low mechanical properties and high degradability [17].

Meanwhile, composite materials consist of organic and inorganic materials have been synthesized to enhance the toughness of synthetic biomaterials [18]. Since the mechanical strength of bioactive ceramics (hydroxyapatite (HA), calcium phosphates, bioactive glasses and related composite materials) and nanocarbons (carbon nanotubes (CNTs), graphene oxide (GO), nanodiamonds, fullerenes) are higher compared to that of polymers, they can also be embedded into the fibers to enhance the mechanical properties of the electrospun nanofibrous scaffolds produced from polymers [15,19,20]. In addition to improved mechanical properties, they provide good

osteoconductivity properties to the polymer matrix, which allows for a better cell seeding and growth environment [5,21].

Furthermore, since electrospun materials have a large surface area because of their morphology, they are under threat of biofilm formation by adhesion of pathogenic microorganisms [16]. For this reason, some antimicrobial ingredients such as metal oxide nanoparticles (silver oxide (Ag_2O), zinc oxide (ZnO), titanium dioxide (TiO_2), copper oxide (CuO), iron(III) oxide (Fe_2O_3)) and metallic nanoparticles (silver, gold, copper) and natural polymers (chitosan) are added to increase the antimicrobial performance of electrospun materials [5,16,22].

In a typical electrospinning process, a polymeric solution is placed into a syringe and pumped through a needle tip. An electrically charged jet which is generated by high voltage differences with positive or negative polarity between the syringe needle and a grounded collector is used to fabricate fibers [6,23,24]. As the polymer solution is exposed on the tip of the needle, the electrical charges on the polymer solution promotes its stretching, which eventually forms ultrafine fiber. During this process, the solvent associated with polymer evaporates immediately and forms a dry polymer fiber that travels in a chaotic pattern and gets deposited on the grounded collector [24]. In this process, nonwoven fibers of varying sizes from micro scale to nanoscale are produced in a way that can mimic ECM dimensions with suitable mechanical properties [15]. Due to their high porosity and surface area/volume ratio, tissue engineering scaffolds can provide cell adhesion, spread, growth and proliferation [15,25]. They are suitable for the use of both synthetic and natural polymers. Various small molecules and nanoparticles can be used as additives in membranes produced by this method. Furthermore, the properties of the obtained fibers can be adjusted by changing the electrospinning process parameters and the collector structures or by using other methods. In addition, this method can be used in a combination with other scaffold production methods [15].

In applications of electrospinning in the field of tissue engineering, tissue-specific processes can be manipulated by obtaining fibers with a controllable fiber diameter by changing the electrospinning solution parameters, process variables, and ambient parameters [3,8]. When the solution parameters are examined briefly, the main polymer and the appropriate solvent for this polymer should be selected first [26]. In

this case, the molecular weight and concentration of the polymer as well as the conductivity of the solvent affect the viscosity and surface tension [26].

The increase in polymer concentration and molecular weight causes an increase in viscosity which results an increase in fiber diameter and decrease in the formation of beads in fibers [26,27]. However, the flow of polymer solution from the capillary tube can be blocked at very high viscosities [26]. On the contrary, fiber formation does not occur under a certain critical chain entanglement concentration and in low molecular weight polymer solutions [15,27]. When evaluated in terms of solvent choice, rapid evaporation occurs in volatile solutions, whereas in solutions with high boiling temperature, beaded fiber structures are obtained as there is no complete evaporation [26]. In addition, the increase in conductivity of the solvent also affects the reduction of fiber diameter. The high dielectric constant of the solvent also makes it possible to spin at low voltage values [27].

Applied voltage is the major processing parameter that influences on the fiber diameter and the fiber morphology. The onset of fiber formation depends on reaching a critical voltage, above which contradictory results have been reported by different researchers. For instance, some studies indicated that more polymer is ejected at higher voltages and thus, fibers with larger diameters are obtained [28]. While, a decrease in the fiber diameter is observed in many studies due to the stretching of the solution at strong electric field [29]. In addition, bead formation has also been found with the further increase in the applied voltage [30]. Therefore, it can be suggested that the applied voltage has effects both on fiber diameter and fiber morphology, but these effects depend on the solution concentration, flow rate and the distance between the tip and the collector [14]. Increases in flow rates affect the wetness of the fibers and cause beaded structures [27]. It influences on velocity of the jet and thus, transfer rate of the fibers onto the collector. Accordingly, solvent will get enough time for evaporation at lower flow rates, whereas bead formation will take place at higher flow rates because of the insufficient solvent evaporation [14]. Increases in the tip to collector distance also provide more solvent evaporation and fiber production occurs at lower diameters [27].

Apart from solution parameters and process parameters, ambient conditions also affect fiber morphology [26]. For instance, the variation of temperature alters viscosity of the polymer solution (i.e., the higher the temperature, the lower the viscosity) [14]. On the

other hand, relative humidity affects evaporation of the solvent and formation of the pores on the fiber surface. When relative humidity is increased, the evaporation rate of the solvent decreases, while porosity and pore diameter of the electrospun material increases [30]. Similarly, vice versa is valid at low relative humidity. However, when the evaporation rate of the solvent is fast, the tip of the needle can be clogged after a few minutes from the onset of electrospinning process [14].

Since the electrospinning parameters are so diverse and complicated, it is difficult to estimate the process outputs before the electrospinning process [31]. For this reason, many researchers have used mathematical and statistical methods for the determination of these parameters. Nanofiber structures with various features can be obtained with these methods. For example, Khatti et al. optimized PCL concentration, applied voltage, tip to collector distance parameters to produce PCL nanofibers with maximum fiber surface area [31]. PCL nanofibers were optimized for the acetabular labrum implant by Anindyajati et al. [13]. Khan et al. achieved the maximum encapsulation effect by minimizing fiber diameter of chitosan/PCL nanofibers to which they contribute tinidazole [32]. Heidari et al. were able to produce graphene added PCL/gelatin nanocomposites for tissue engineering applications [17]. Anaraki et al. designed a polylactic acid/polyethylene glycol/multiwalled carbon nanotube electrospun nanofiber scaffold as an anticancer drug delivery system [12]. Neo et al. optimized zein nanofibers for use in the food industry [33].

In this context, in this PhD study, two different metallic nanoparticles (silver nanoparticles and copper nanoparticles) were synthesized by using biopolymers (soluble starch and sodium alginate) as the capping and reducing agents. An investigation was made on their use in tissue engineering applications by using electrospinning method. In the first article in this thesis, Ag nanoparticles coated with soluble starch were added to polyvinyl alcohol nanofibers and it was determined that this nanofiber mat had a potential to be used as wound dressing material. In the second article, the usability of the obtained Ag nanoparticles in bone tissue engineering applications was determined. Gelatin was used as the biopolymer, and 45S5 bioactive glass particles were used as the inorganic component of the obtained nanofiber mat. The electrospinning parameters which give a model to predict nanofiber size was determined by using Box-Behken design which is a statistical experimental method. In the third article, copper nanoparticles were synthesized by using soluble starch and

sodium alginate as the capping agents and it was concluded that the copper nanoparticles capped with soluble starch were suitable for tissue engineering applications. In the fourth article, soluble starch capped copper nanoparticles and 45S5 bioactive glass particles were used as the additives in poly (ϵ -caprolactone) nanofiber mats. Box-Behnken design was used to determine the polymer solution parameters for the production of the nanofiber mat which had similar fiber sizes with bone tissue extracellular matrix.



2. FABRICATION OF ANTIBACTERIAL POLYVINYLALCOHOL NANOCOMPOSITE MATS WITH SOLUBLE STARCH COATED SILVER NANOPARTICLES (¹)

2.1 Introduction

Over the last decade, great emphasis has been placed on tissue engineering, the area of wide nanomaterial applications, prompting recovery or substitution of harmed tissues by giving two or three dimensional (2D/3D) scaffolds for cell growth and resulting tissue association [34,35].

Cells in their natural environment cooperate with the extracellular matrix (ECM) components in the nanometer dimension [36]. These local ECMs have a role as platform to unite cells in tissue, to control the tissue structure and manage the cell phenotype [37]. The morphology of the obtained scaffolds ought to take after that of the ECM of local tissues with a nanofiber structure. Thus, scaffolds provide particular macro and micro structure to alter the biological and biomechanical response of the cells during the process of healing [37,38]. The long time hypothesis has been proposed that natural ECM should imitate in order to design an ideal scaffold that can multiply all of the fundamental intercellular reactions and support local responses [36]. In tissue engineering, scaffolds implanted in the bodies must regulate local cell attachment, proliferation, growth and metabolism in it through characteristics of scaffold, as it integrated with local tissue [38,39]. Therefore, significant attention has been paid to nanofibrous matrices because of their ability to interact with cells to mimic natural ECM [36].

Various processing methods for the fabrication of nanofibers such as template synthesis, bicomponent fiber production, centrifugal spinning, self-assembly, phase separation, melt blown and electrospinning have been utilized. In addition, nanofiber

¹ This chapter is based on the paper: "Aktürk, A., Erol Taygun, M., Karbancıoğlu Güler, F., Göller, G., Küçükbayrak, S. (2019). Fabrication of Antibacterial Polyvinylalcohol Nanocomposite Mats with Soluble Starch Coated Silver Nanoparticles. *Colloids and Surfaces A: Physicochemical and Engineering Aspects*, 562, 255-262."

production can be done with the combination of these methods such as pressurized gyration, in which the solution blowing and centrifugal spinning are combined in order to make more efficient production. [34,40-42]. However, there are some limitations as well as the advantages of these approaches. For example, nanofoams with desired structures are produced with a complex and long lasting process by using phase separation method. In the self-assembly method, very fine diameter fibers with low productivity are produced. As a result, electrospinning is one of the most widely reported studies in the literature [41]. Compared with other methods, electrospinning is a promising and adaptable method used to create ultrathin fiber mats due to its cost effectiveness and straightforwardness [34,36,40,43-46]. These nanofiber networks display extraordinary characteristics, such as very large surface area to volume ratio, high porosity with a small size, flexibility in surface functionalities and so forth [43,44,47-49]. Because of that, electrospun nanofibers may be good candidates for a noteworthy number of biomedical applications such as wound dressings, drug delivery systems, scaffolds for tissue engineering and antibacterial applications [43,50].

In recent years, polymer nanofibers containing functional nanoparticles have become increasingly attractive due to their promising properties and applications [46]. Among the various types of nanoparticles used to enhance polymers, silver nanoparticles (Ag NPs) are the most frequently explored, because of their electronic properties, optical, catalytic and antimicrobial activities [51]. Numerous investigators, who have had the motivation to build a synergistic nanocomposite, endeavored to synthesize silver-based antimicrobial hybrids. Therefore, hybrid nanocomposite materials containing chitosan, silicon, cotton, polyurethane, polyester and polycaprolactone have been fabricated [52]. It has recently been noted that incorporation of silver nanoparticles into nanofibers is very important because the obtained nonwoven material has very strong antimicrobial activity. Silver nanoparticle filled nanofibers will display substantially much stronger antimicrobial action than regular microfibers because of their higher surface area to volume proportion [46].

Several methods have been investigated for synthesizing silver nanostructures. These include chemical reduction, thermal degradation, UV irradiation reduction, photoreduction, electrolytic processing, gamma irradiation, polyol processing, electrochemical, photochemical, sonochemical, reverse micelles processes, microwave dielectric heating reduction, solvothermolysis, green synthesis of metal

salts and biological methods [53-55]. In these methods, chemical reduction offers the advantage of simple machinability and it is used extensively, while physical approaches require highly sophisticated tools and specific conditions [54]. Be that as it may, conventional chemical reduction strategies require toxic reducing agents or other non-aqueous organic chemicals, which are costly and not environmentally benign [54,56]. The growing awareness of the protection of the environment has led to the development of an environmentally friendly approach to the synthesis of Ag NPs using justified choices of reductive and stabilizing agents and solvents. The use of microwave heating for chemical synthesis is particularly suited to nanometal synthesis since it is faster and simpler than similar thermal transfer methods and can provide a uniform heating around the nanoparticles and help them ripening without aggregation [54]. Microwave irradiation creates very rapid nucleation zones in the solution, which essentially increases the reaction rate [53]. For this reason, a combination of a green reduction and stabilizing agent with microwave heating can provide a new route for the synthesis of Ag NPs [54].

From perspective of green synthesis, the preparation of nanoparticles inside biopolymers gives many advantages, including the ability to have a large number of hydroxyl groups capable of complexing metal ions, thus well controlling the size, shape and distribution of nanoparticles, increasing the biological composition and biodegradability, offering to produce species that are less toxic to mammalian cells [57]. Earlier reports have dealt with biopolymers like proteins such as bovine serum albumin [58], aminoacids such as L-lysine [59] and L-arginine [59], polysaccharides, such as glycogen [60], alginate [61], chitosan [62,63], starch [59,64-69], polysaccharide derivatives such as microcrystalline cellulose [70], carboxymethyl cellulose sodium [71], carboxymethyl chitosan [72], disaccharides such as maltose [73], monosaccharides such as dextrose [66] and glucose [69] were used as stabilizing and reducing agents for the synthesis of silver nanoparticles by utilizing microwave irradiation.

In the green synthesis method, non-toxic chemicals, environmentally compatible solvents and renewable materials are used. Starch, a biocompatible and biodegradable material that is widely available and cost-effective, is one of the natural polymers used in various applications such textile, paper and paper products, human and animal diets [74]. Because of both being renewable and dispersing with water, starch was used in

this study as the capping and reducing agent to obtain silver nanoparticles since it is environmental and biological friendly [75]. However, Martinez Rodriguez et al. [38] have reported that complex polymer chains and functional groups of polysaccharides promote the formation of solutions with high surface tension and viscosity which prevents the spinability of these solutions. To manage this problem, polymers with tensoactive behavior such as polyvinyl alcohol (PVA) and polyethylene oxide (PEO) have been reported to improve the spinability of polysaccharide solutions when added in different percentages into the blends [76]. That is why, PVA was selected as the biopolymer which is used for various biomedical applications [77]. To the best of our knowledge, we proposed the microwave assisted irradiation for silver nanoparticle production by using soluble starch as a green chemistry approach and incorporation of these nanoparticles into the PVA nanofiber structure for the first time. In this study, it was aimed to fabricate and characterize PVA/silver nanoparticle composite scaffolds for wound dressing applications. The impact of these silver nanoparticles on the PVA nanofiber mat and the crosslinking processes to make these nanofiber mats insoluble were evaluated and discussed in detail.

2.2 Materials and Methods

2.2.1 Materials

Silver nitrate (AgNO_3), sodium hydroxide (NaOH), soluble starch, acetone, Tryptic Soy Broth (TSB), and Tryptic Soy Agar (TSA) were all purchased from Merck. Polyvinyl alcohol (PVA, 98-99% hydrolyzed, $M_w=85000-124000$) was obtained from Acros. Glutaraldehyde (GA, 50%wt) was supplied from Sigma Aldrich. All chemicals were used as provided without further purification and all the solutions were prepared using deionized water.

2.2.2 Preparation of silver nanoparticles

Soluble starch based silver nanoparticles (S-Ag NPs) were prepared by using microwave assisted green synthesis in the present study. Firstly 0.5 wt/v% starch solution was prepared to synthesize silver nanoparticles and then 1 M AgNO_3 was added into in it. NaOH solution was used to adjust the pH of the silver containing soluble starch solution to 8.5. Finally, the obtained solution mixture was reacted in a microwave oven operated at 180 W for 1 hour.

2.2.3 Preparation of electrospinning solutions

8% (wt/v) of PVA was prepared in deionized water at 85 °C with constant stirring for 4 h. The obtained S-Ag NPs solution was added to the PVA solution at the ratios of 5% (w/w), 10% (w/w) and 15% (w/w) and the mixtures were stirred for 1 hour.

2.2.4 Electrospinning

The as-prepared solutions were transferred to a plastic syringe equipped with a flat stainless steel needle, which was connected to a high voltage supply. Voltage applied to the needle was 30 kV. They were fed from the syringe to the needle tip at a controlled flow rate of 1 ml/h by a syringe pump. Electrospinning process was performed using an electrospinning device (Nanospinner 24 Touch, Inovenso Co.) at 23 °C with a relative humidity of 47-48 %. As-spun fibers were deposited as nonwoven mats onto an aluminum foil wrapped around a grounded collector placed at a distance of 11 cm perpendicular to the needle tip. The resultant fibrous mats were dried at 37°C for a couple of days to remove residual solvent and then transferred to a desiccator prior for further investigations.

2.2.5 Cross-linking treatment

The nanofiber mats dried at 120 °C for 2h were immersed in the solution of 5% (v/v) GA/acetone solution at 37 °C for 2 h, following a post treatment at 120 °C to remove residual glutaraldehyde and to partially enhance the cross-linking. The success of cross-linking was determined by testing the dissolubility of the cross-linked mats immersed in simulated body fluid (SBF, pH 7.4) at 37°C at different time points (up to 28 days).

2.2.6 Assessment of the release of Ag⁺ ions from nanofiber mats

Briefly, nanofiber mats were added to the freshly prepared SBF at a 0.25 mg/mL ratio in sterile polyethylene containers and were stored at controlled temperature of 37 °C for various time points up to 28 days. The degradation behavior of the fibrous mats was studied as a function of immersion time in SBF. At the end of each time point, the samples were removed from SBF, gently rinsed with deionized water for three times to remove saline, and dried at 37 °C until constant weight obtained. After that, the samples were kept in desiccators for further characterization. Meanwhile, SBF was

cooled to room temperature, and the concentration of silver ions released into SBF was measured, as well.

2.2.7 Antibacterial activity

In this study, antimicrobial effects of the nanofiber mats against *Escherichia coli* ATCC 25922, *Staphylococcus aureus* ATCC 29213 were examined by using disk diffusion method. The PVA nanofiber mat was used as control. Nanofiber mats were cut as discs with diameter of 15 mm and sterilized under UV irradiation for 2 h (each side for 1 h). Bacteria were grown in TSB, by incubating at 37 ° C for 24 hours. After the incubation, bacterial concentrations of *E. coli* and *S. aureus* were adjusted approximately to 10⁶ CFU / mL and then 100μL of this bacterial suspension was spread on TSA. After that sterilized nanofiber mats were placed on the inoculated TSA. After incubation at 37 ° C for 24 hours, the antimicrobial properties of the nanofiber mats were assessed by measuring the inhibition zone diameter (including nanofiber mat) in each inoculated plate. All analysis were carried out in triplicate for each nanofiber mat.

2.2.8 Characterization studies

Dynamic light scattering (DLS) analyzer (Nanoflex particle size analyzer) and field emission scanning electron microscope (FE-SEM, JSM 7000 F, JEOL) were used to characterize the Ag NPs in terms of particle size and shape. The surface morphology and microstructure of fibrous mats were observed by using a scanning electron microscope (SEM, JSM-5410, Jeol) operated at 20 kV. Prior to the SEM measurements, all of the samples cut from the fibrous mats were coated with platinum under vacuum for 120 s by using a sputter coater (SC7620, Quorum Technologies Ltd) in order to reduce electron charging effects. The diameter of the electrospun fibers was measured by using Image J software (National Institute of Health, USA). For each experiment, average fiber diameter and its standard deviation were determined from 50 measurements of the randomly chosen fibers.

The functional groups of fibrous mats were investigated by Fourier transform infrared (FT-IR) spectroscopy. FT-IR spectra were collected using a spectrometer (Spectrum 100, Perkin Elmer) in transmittance mode in the mid-IR region (4000–650 cm⁻¹). The characteristic phases of Ag NPs and fibrous mats were identified using an X-ray diffraction analyzer (XRD, Panalytical, Xpert Pro) with Cu-Kα radiation.

XRD patterns were acquired over a 2θ range from 10° to 90° with a step size of 0.01° . The release of silver ions from fibrous mats was measured as a function of immersion time in SBF with the aid of inductively coupled plasma–mass spectrometer (ICP-OES, Perkin Elmer, Optima 2100 DV model).

2.3 Results and Discussion

2.3.1 Silver nanoparticle production

Microwave assisted synthesis of silver nanoparticles was carried out by reduction with soluble starch which can act as a reductant for silver salt in basic media. Visual observation of the specific browning color on the colloidal Ag NP solution was determined. This result identifies that the stabilized silver nanoparticles were successfully formed in soluble starch [78-80]. The characteristics of Ag nanoparticles were investigated by utilizing FE-SEM and XRD measurements. The XRD analysis of the colloidal silver nanoparticle solution given in Figure 2.1(a) showed peaks at $2\theta = 39.06^\circ, 44.67^\circ, 65.01^\circ, 77.98^\circ$ and 81.59° , which correspond the crystal planes of (111), (200), (220), (311), and (222) of face centered cubic (FCC) silver suggesting the successfully synthesis of silver nanoparticles [49,77,80-89].

The morphology and average size of the silver nanoparticles were investigated by FE-SEM and DLS. As depicted in FE-SEM micrograph given in Figure 2.1(b), the sphere shaped Ag NPs were homogenously distributed with average size of 19 ± 6 nm. However, the cumulative distribution of silver nanoparticles presented in Figure 2.1(c) exhibited a wide particle size range from 25 nm to 410 nm with average size of 71.6 nm. The remarkable difference between these particle size measurements is based on the fact that their measuring principles are different. Since the hydrodynamic volume of NPs is measured in the DLS analysis, the particle size data includes the polymer chain domain surrounding the NPs leading to overestimated particle size measurement, while the physical size of the nanoparticles was measured with the FE-SEM [80]. Based on these results, it can be interpreted that soluble starch coated the silver nanoparticles. Examination of these results demonstrates that nanoparticles are adsorbed on the surface of the amylose coil and various layered-like starch structures [90]. It is possible that the silver nanoparticles we obtained in this study would have similar reactions with Ag NPs synthesized by Valencia et al. using soluble starch at 90°C for 12 hours [91].

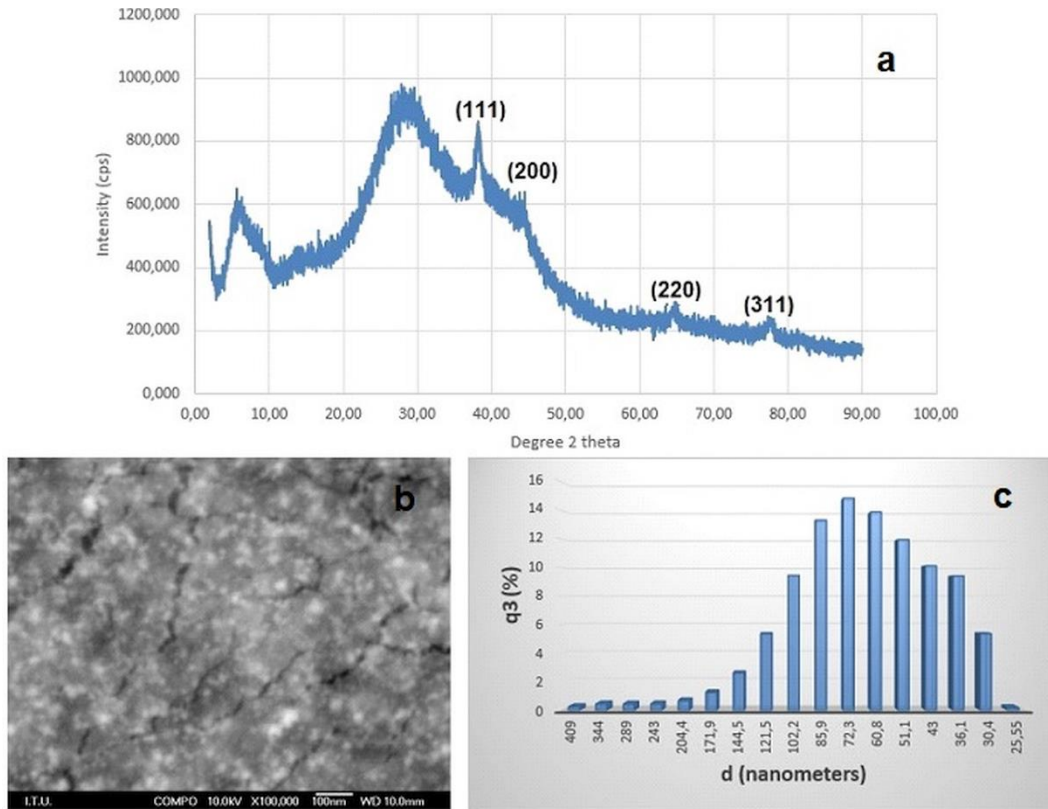
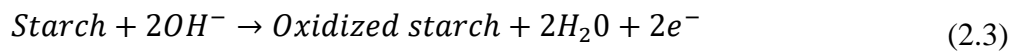


Figure 2.1 : (a) XRD pattern, (b) FE-SEM image and (c) DLS analysis of silver nanoparticles solution synthesized in soluble starch (S-Ag NPs).

By using the production method in our study, the reaction time was reduced with microwave irradiation method. According to the given reactions in the study of Valencia et al., the addition of silver nitrate (pH-3) starts with the oxidation of starch in an acidic solution. Under these conditions, the oxidation of primary hydroxyl groups between carbon 2 and 3 to starch (C2 and C3) can occur, where the primary hydroxyl group is oxidized to the carboxyl group. The OH group generated from the dissociation of NaOH leads to the oxidation of starch and free electrons released after this reaction help to reduce Ag^+ to Ag^0 . Possible reactions are given in equations 2.1-2.5.





2.3.2 Morphology and structural analysis of nanofibers

Figures 2.2(a-d) depict the surface morphology, average diameter, and diameter distribution of S-Ag NPs loaded PVA nanofiber mats with varying S-Ag NPs ratio to PVA solution of 5, 7.5 and 10 wt/wt %, (5S-Ag NPs loaded PVA, 7.5S-Ag NPs loaded PVA, and 10S-Ag NPs loaded PVA nanofiber mats) respectively.

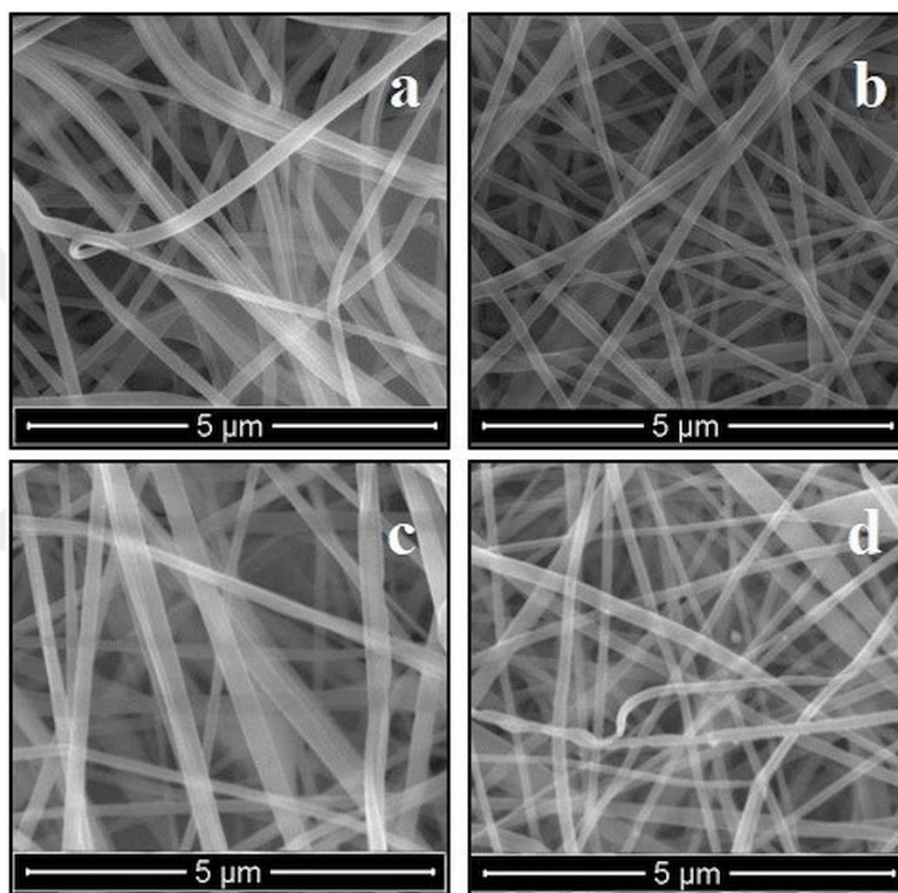


Figure 2.2 : SEM images of neat PVA (a), 5S-Ag NPs loaded PVA (b), 7.5S-Ag NPs loaded PVA (c) and 10S-Ag NPs loaded PVA (d) nanofiber mats.

The average fiber diameters of the neat PVA, 5S-Ag NPs loaded PVA, 7.5S-Ag NPs loaded PVA, and 10S-Ag NPs loaded PVA nanofiber mats were found as 163 ± 42 nm, 141 ± 37 nm, 184 ± 60 nm and 152 ± 45 nm. As seen in the figures, the obtained uniform nanofiber mats exhibited wrinkled and porous surfaces which could take part in the sustained release of Ag nanoparticles. It can be observed that the diameters of the fiber mats have remained relatively unchanged when the S-Ag NPs content in the polymer solutions increased. The incorporation of S-Ag NPs did not influence the average

diameter of PVA nanofibers essentially due to inherent polarity of the PVA solution [43].

XRD analysis was performed to determine the form of silver in the nanofiber structure (Figure 2.3(a)). The formation of silver oxides was observed at the case of electrospinning of PVA and S-Ag NPs together [44,48].

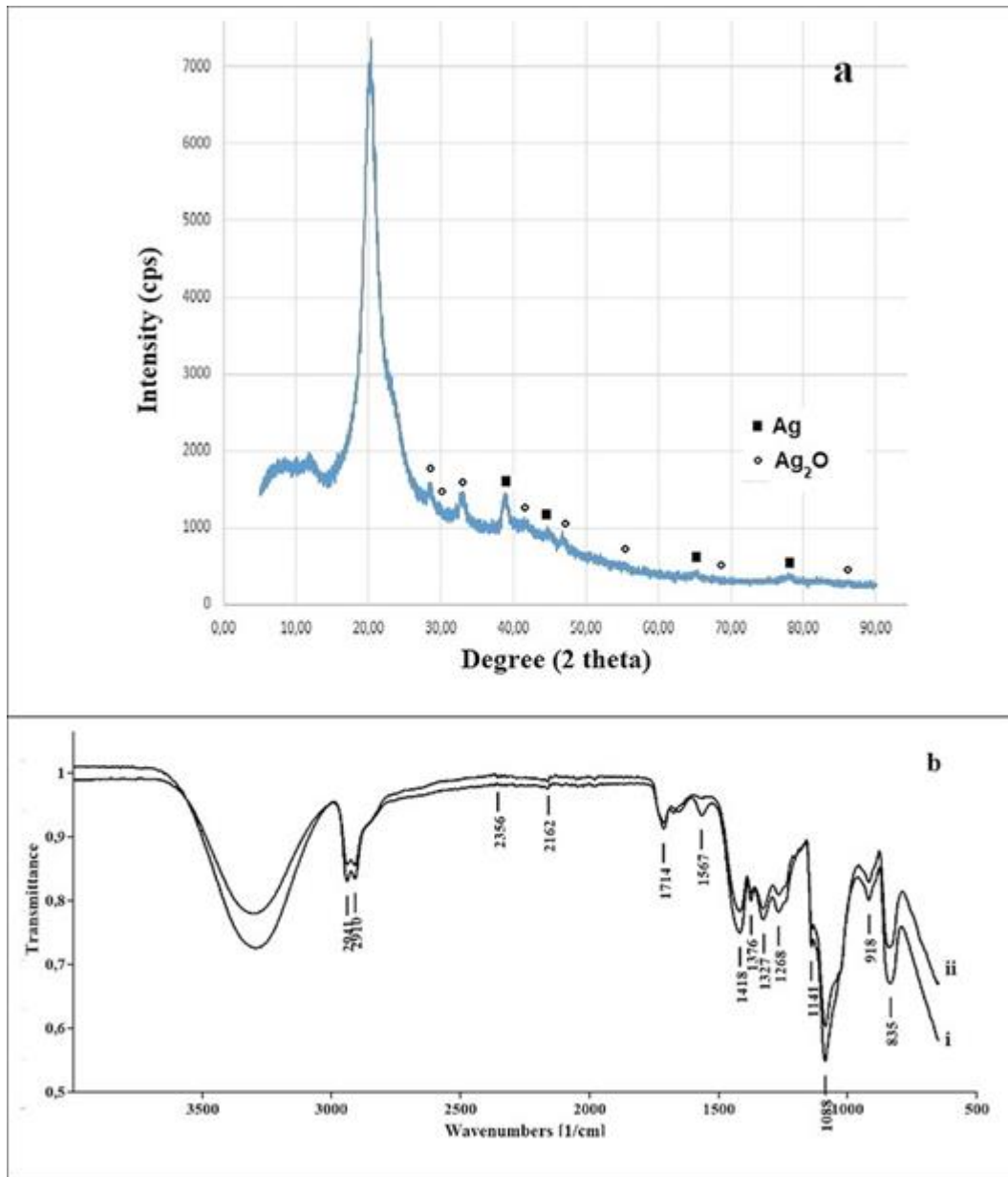


Figure 2.3 : (a) XRD pattern of the 10S-Ag NPs loaded PVA nanofiber mat, (b) FTIR spectra of neat PVA (i) and the 10S-Ag NPs loaded PVA nanofiber mats.

According to the XRD graph, a noteworthy peak at about 20.31° originated from the PVA and is caused by the emergence of string inter and intermolecular bonding [49,92]. The peaks at 39.06° 44.67°, 65.44°, and 78.14° represented the (111), (200),

(220), and (311) planes of silver nanocrystals with cubic symmetry [81]. Additionally, the oxidized silver forms were detected at 28.31°, 28.68, 33.14°, 41.56°, 46.77°, 55.30°, 69.07°, and 86.18° [86].

In addition, FTIR spectroscopy was used to analyze the organic functional groups of S-Ag NPs loaded PVA nanofiber mats in order to obtain further information on the silver nanoparticle containing nanocomposites. Figure 2.3(b) shows FT-IR spectra of neat PVA and 10S-Ag NPs loaded nanofiber mat. As seen from Figure 2.3(b), a large, broad band observed between 3000-3650 cm^{-1} is characteristic stretching vibration of hydroxyl (-OH) group showing presence of both strong internal hydrogen bonds, intra molecular hydrogen bonds and free hydroxyl groups [23,93]. Both CH_2 symmetrical (ν_s) and antisymmetric (ν_{as}) stretching vibration bands are particularly noteworthy in the region between 2800 and 3000 cm^{-1} . The other characteristic peaks of neat PVA were assigned as follows: 2940 cm^{-1} (asymmetric $-\text{CH}_2-$ vibration), 2910 cm^{-1} (symmetric $-\text{CH}_2-$), both 1713 cm^{-1} and 1087 cm^{-1} (C=O groups), 1418 cm^{-1} (C-C stretching vibration in $-\text{CH}_2-$), 1328 cm^{-1} (C-C stretching vibration), 1087 cm^{-1} (C-O stretching and bending modes), 1141 cm^{-1} (symmetric C-C stretching mode in crystalline regions), 856 cm^{-1} (C-C vibrational modes), on hydroxyl (HO-R) and ($\text{CH}_3\text{COO-R}$) functional groups [76,79,87,94,95]. When the FTIR spectra of pure PVA and 10S-Ag NPs loaded PVA nanofibers were compared, no shifts in the bands were observed indicating that there is no chemical combination in the hybrid process. However, the relative transmittance decreased with Ag NPs content as Zhang et al. observed in their study [82].

2.3.3 Selection of the suitable crosslinking treatment

The protection of nanofibrous mat fiber morphology and interfiber pores is important for tissue engineering applications where the high volume to surface area ratio is advantageous [94]. The nanofiber mat with the highest S-Ag NPs content was selected and the characterization studies were carried out to determine the suitable crosslinking process. For this reason, the nanofiber was subjected to two cross-linking operations: heat treatment and glutaraldehyde immersion. SEM images of 10S-Ag NPs loaded PVA nanofiber after both crosslinking treatments were depicted in Figure 2.4. As seen from the Figure 2.4, the nanofibers maintained their morphology after crosslinking treatments. It was found that the network and pore size of nanofiber mats did not

change after both applications. However, the colors of the obtained nanofiber mats crosslinked by glutaraldehyde were changed from white to yellow as observed in the work of Li et al. [87]. The chemical structure of nanofiber mats containing Ag NPs before (Figure 2.5(a)) and after heat treatment (Figure 2.5b) was mainly confirmed basically by structural changes and new absorption bands showing the formation of rearranged fiber structures were detected by using FTIR.

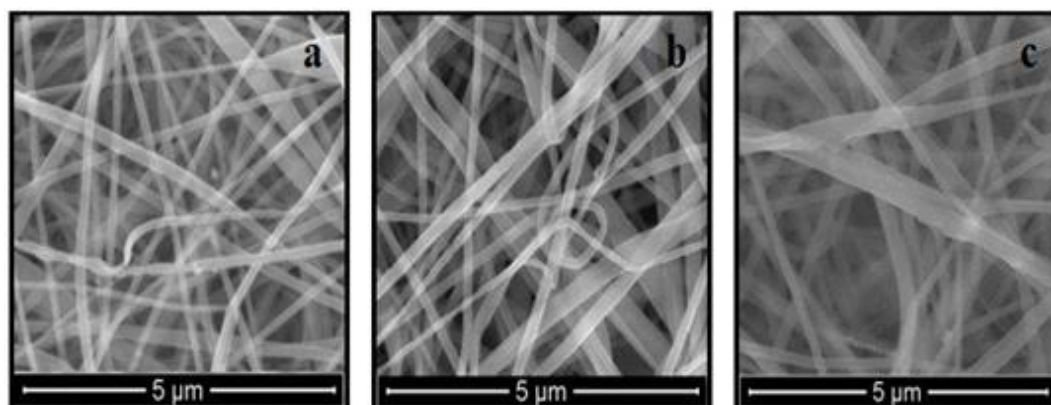


Figure 2.4 : SEM images of the uncrosslinked 10S-Ag NPs loaded PVA nanofiber mat (a), the crosslinked 10S-Ag NPs loaded PVA nanofiber mat by heat treatment (b), and glutaraldehyde immersion (c).

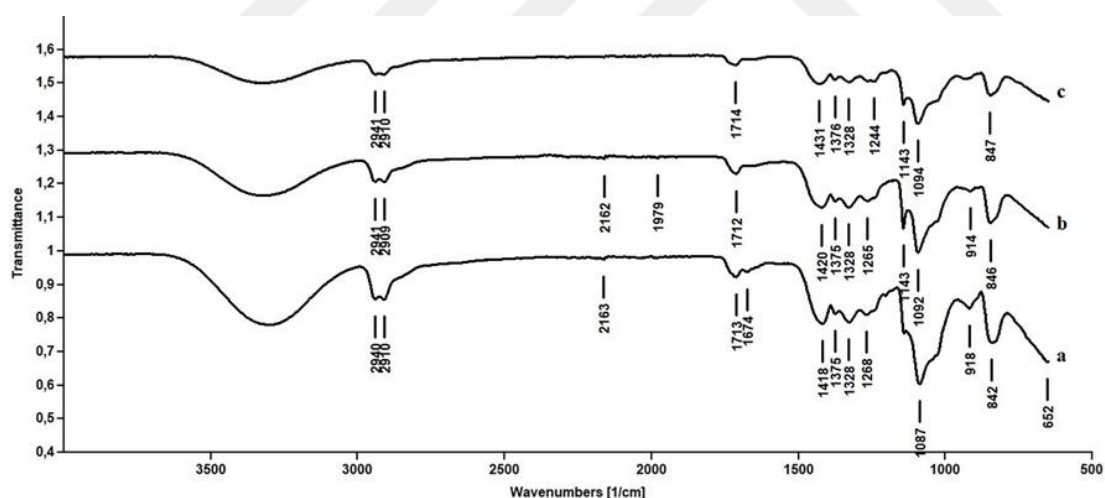


Figure 2.5 : FTIR spectra of neat 10S-Ag/PVA (a), the cross-linked 10S-Ag/PVA by heat treatment (b), and the cross-linked 10S-Ag/PVA by glutaraldehyde immersion (c).

A significant increase in a peak at 1414 cm^{-1} was observed after the heat treatment of S-Ag NPs loaded nanofiber mats. This characteristic peak is well known to be a sensitive marker for determining the degree of crystallinity of PVA. In other words, the crystallization behavior of PVA is increased due to the thermal treatment which plays an important role in preventing the dissolution of nanofibers in solutions [95].

After the heat treatment and glutaraldehyde immersion, the density of the bands of the OH group was found to be relatively lower when compared to the original nanofiber mat [85]. It was conceivable that cross linkages between two hydroxyl groups may occur by losing H₂O at high temperatures at thermal treatment [48]. The nanofiber mat immersed in glutaraldehyde (Figure 2.5(c)) had also the O-C-O vibration of the acetal group observed at 1000-1140 cm⁻¹ [85]. However, the acetal bond at this process was formed between the aldehyde ends of the GA and the hydroxyl groups of the PVA nanofibers both in the intramolecular and intermolecular manner which occurred within the nanofibers and at the interface between the nanofibers [94].

The released amount of Ag⁺ ions from 10 S-Ag NPs loaded PVA nanofiber mat in the simulated body fluid (SBF) was determined by ICP-OES to find out which cross-linking process is effective in Ag⁺ ions release (Figure 2.6). The concentration of released silver ions into SBF was in the range of 0.2-0.6 ppm after 28 days of nanofiber immersion for the 10S-Ag NPs loaded PVA nanocomposite mat cross-linked by heat treatment. On the other hand, the concentration of released silver ions from the 10S-Ag NPs loaded PVA nanofiber mat cross-linked by glutaraldehyde was in the range of 0.9-1.2 ppm after 28 days of nanofiber immersion. When the silver concentration is greater than 0.1 ppb, the constant release of silver cations over a long period of time may prevent growth of bacteria [96,97]. The obtained silver ions release values indicated that both nanofibers possess potency to exhibit antibacterial activity.

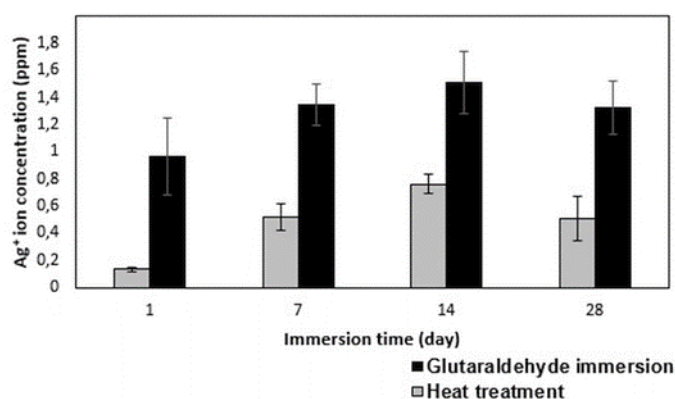


Figure 2.6 : Ag⁺ ion releases of 10S-Ag NPs loaded PVA nanofiber mats cross-linked by heat treatment and by glutaraldehyde immersion in the SBF.

However, the release of silver ions from the nanofiber cross-linked with glutaraldehyde was found to be higher. For this reason, SEM images of samples cross-linked with heat treatment and glutaraldehyde immersion were examined to determine the fiber structure change in SBF immersion for 1, 7, 14, 28 days (Figure 2.7). SEM

images showed more deterioration in fiber structure cross-linked by heat treatment. Glutaraldehyde cross-linked nanofiber mat appeared to protect the fiber structure after interaction with SBF. It might be concluded that glutaraldehyde cross-linked nanofiber mat released more silver ions than the nanofiber mat cross-linked by heat treatment due to preserving its surface area to volume ratio.

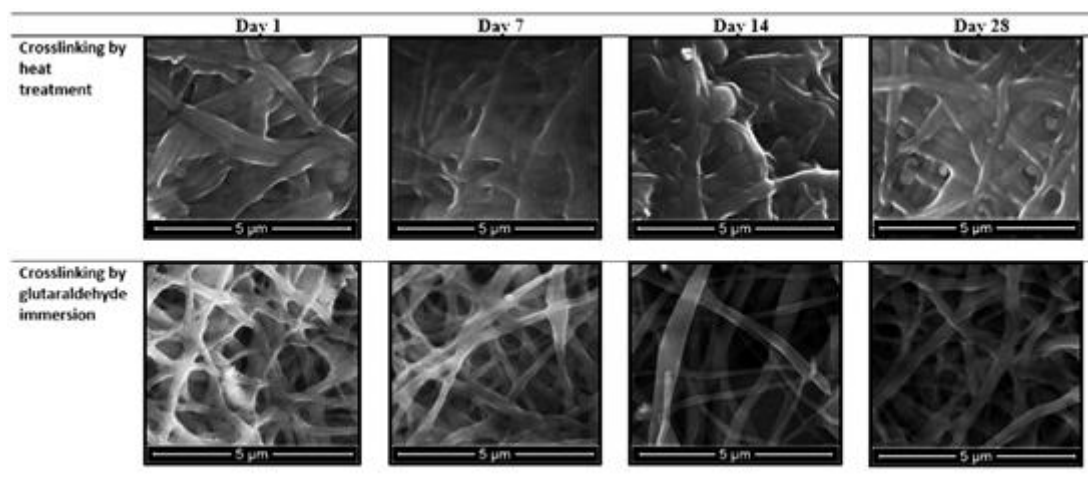


Figure 2.7 : SEM images of the cross-linked 10S-Ag/PVA nanocomposite by heat treatment, and the cross-linked 10S-Ag/PVA nanocomposite by glutaraldehyde immersion in different time intervals in SBF.

2.3.4 Antibacterial activity of nanofibers

The antimicrobial action of silver nanoparticle containing nanofiber mats can be credited to the reality by the production of reactive oxygen species, membrane disruption and the interaction of silver ions with respiratory enzymes [52]. Silver nanoparticles can interact with the sulfur containing proteins from cell membrane and phosphorous containing compounds in cell which attack the respiratory chain with cell division driving to cell death. It has been claimed that silver ions bind to thiol groups within the enzymes and hence deactivate the enzymes. The utilize of Ag NPs has displayed, strong inhibitory and antibacterial effects with exceptional broad spectrum of antimicrobial action because they show activity over a 24 hour period due to their high surface area to volume ratio [49,79]. However, the toxicity of Ag NPs has drawn public attention. Therefore, in order to meet the needs of antibacterial activity and cytotoxicity, a balance must be considered in the design and applications of biomaterials containing Ag NPs. It was reported that the Ag⁺ concentrations below 2.3 ppm and 1.7 ppm had no toxic effect on HaCat keratinocytes and human epidermal keratinocytes, respectively [97]. The silver ions release of the highest silver

nanoparticles content of the nanocomposite fabricated in this study was found to be 1.24 ppm, which was greater than 0.1 ppb and less than 1.7 ppm, indicating that the nanofiber structure was suitable for biological applications. The antibacterial analysis was performed with 5S-Ag NPs loaded PVA, 7.5S-Ag NPs loaded PVA and 10S-Ag NPs loaded PVA nanofiber mats cross-linked with glutaraldehyde, since the glutaraldehyde cross-linked samples were considered to have more antibacterial activity and ion release values were below toxic values. The antibacterial activity of the nanocomposites against *S. aureus* and *E. coli* was determined by measuring the inhibition zone around the nanofiber mats (Table 2.1).

Table 2.1 : The inhibition zone measurements taken after 24 h for 5S-Ag NPs loaded PVA, 7.5S-Ag NPs loaded PVA, and 10S-Ag NPs loaded PVA nanofiber mats against *E.coli* and *S.aureus*.

Sample	<i>E. coli</i>		<i>S. aureus</i>	
	DD (mm) ¹	DIZ (mm) ^{2,3}	DD (mm) ¹	DIZ (mm) ^{2,3}
Neat PVA (Control)	15.0	15.0	15.0	15.0
5S-Ag NPs loaded PVA	14.6±0.5	17.5±0.5	15.0	21.0±0.6
7.5S-Ag NPs loaded PVA	14.8±0.4	17.7±0.5	14.1±0.4	21.0±0.6
10S-Ag NPs loaded PVA	14.4±0.5	17.6±1.4	14.2±0.5	19.6±0.5

¹DD: Disc diameter, ²DIZ: Diameter of inhibition zone,³DIZ values include disc diameter

Pure PVA nanofiber mats didn't show any significant antibacterial activity against tested microorganisms. As seen in the Figure 2.8, all samples had similar blocking zones around them and it was concluded that starch coated silver nanoparticles even at the lowest content were solely responsible for the antibacterial activity.

Antimicrobial activity of silver nanoparticles against *S. aureus* and *E. coli* was also stated in previous studies [52,82,83,98]. In this study, clearer and larger circular zone inhibition was observed against *S. aureus* has been also reported by Lin et al., Zhang et al. and Wang et al. It is believed that the reason of this observation is the difference between the cell wall structures of the Gram-positive (*S. aureus*) and gram-negative (*E. coli*) bacteria [82,83,98].

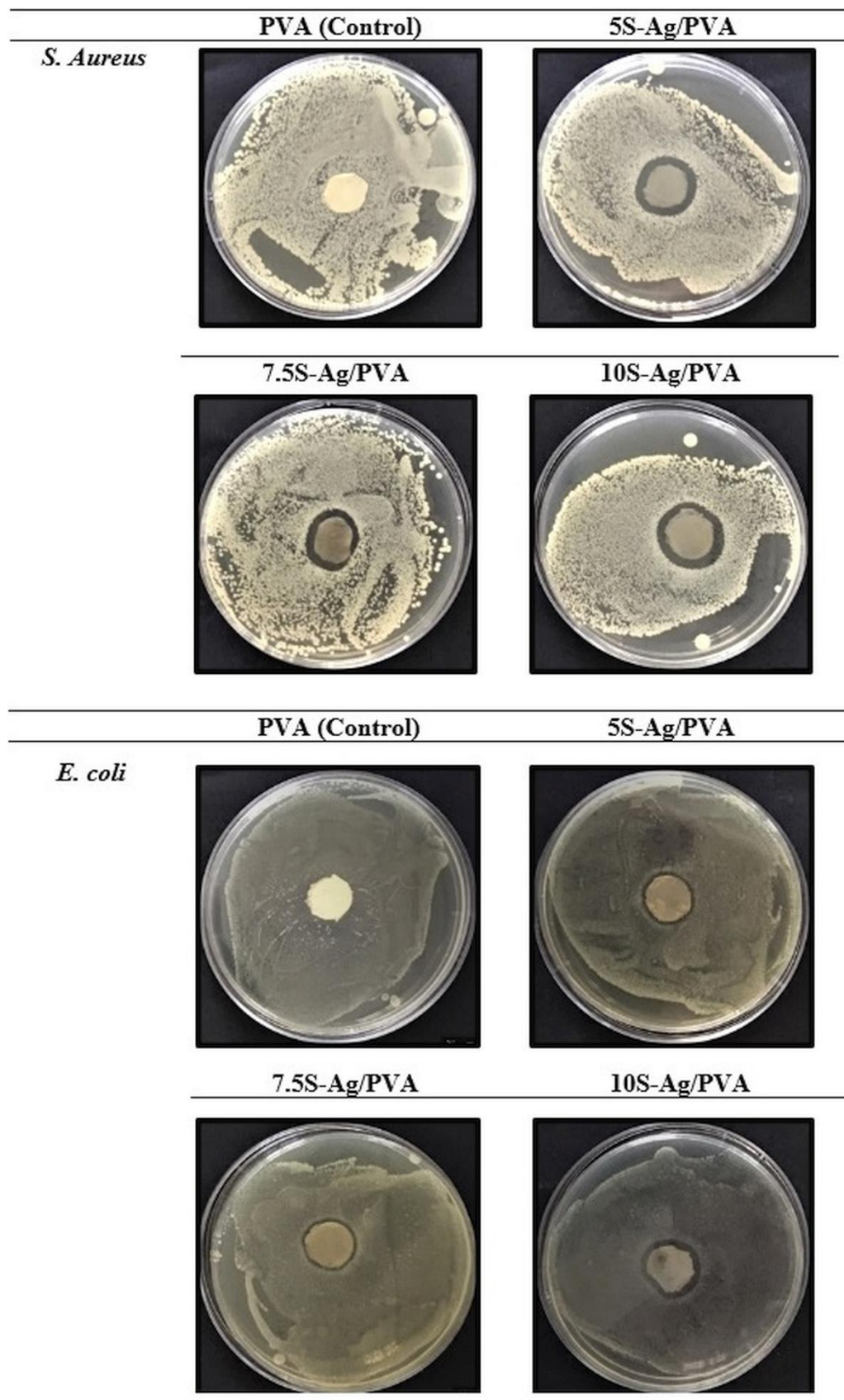


Figure 2.8 : Images of antibacterial activity of 5S-Ag NPs loaded PVA, 7.5S-Ag NPs loaded PVA and 10S-Ag NPs loaded PVA nanofiber mats crosslinked by glutaraldehyde immersion against *S. aureus* and *E. coli*.

2.4 Conclusions

In the present study, silver nanoparticles were synthesized in soluble starch solution with a particle diameter of 19 ± 6 nm by using microwave synthesis method and this solution was used as the antibacterial agent for PVA nanofibers at different weight ratios. It was determined that the nanofibers containing up to 10 (wt/wt) % S-Ag NPs were fabricated in a morphology of porous, interconnected and fiber structure. It was seen that when glutaraldehyde immersion was used as the crosslinking process, the silver ions release was found to be more efficient. The findings indicated that the nanofiber mats containing silver nanoparticles at 5, 7.5, and 10 (wt/wt)% have the potential for wound dressing applications.





3. OPTIMIZATION OF THE ELECTROSPINNING PROCESS VARIABLES FOR GELATIN/ SILVER NANOPARTICLES/BIOACTIVE GLASS NANOCOMPOSITES FOR BONE TISSUE ENGINEERING²

3.1 Introduction

Response Surface Methodology (RSM) is a combination of statistical and mathematical techniques that allow the creation of an approximate model for defining the relationship between a response and a set of predictive variables, based on an empirical data with an appropriate experimental method [99]. It is possible with RSM to query simultaneously the impact of single factors and their common interactions with the possibility of defining quantitatively optimized conditions to be applied to some results or quality characteristics of a particular process [99-101].

In recent years, RSM has received great attention due to its easy application for the optimization of the electrospinning process and the ability of adapting to different polymer/solvent systems [99]. Subsequently, various investigations related with biomedical usages such as drug delivery, tissue scaffolds and protective masks have concentrated on utilizing RSM to display the impact of electrospinning parameters on the fiber diameter [12,33,100-120].

Notwithstanding its simplicity the electrospinning process is confounded by various factors that need to be considered [108]. The factors such as solution parameters (polymer type, polymer concentration, polymer molecular weight, solvent dielectric constant, surface tension, solvent type, solvent volatility, viscosity, conductivity), operating variables (applied voltage, flow rate, needle diameter, electric field strength, tip to collector distance, and electrostatic field shape), and ambient conditions (atmosphere, pressure, temperature, humidity, etc.) play an important role in the spin ability and fiber properties including fiber diameter and morphology [12,100-102,104,105,108,110,111,113,114,116,121]. In this way, it is desirable to have a

² This chapter is based on the article “Akturk, A., Erol Taygun, M. Goller, G., (2020). Optimization of The Electrospinning Process Variables For Gelatin/ Silver Nanoparticles/Bioactive Glass Nanocomposites for Bone Tissue Engineering. *Polymer Composites*, 41(6), 2411-2425”

quantitative connection between these parameters and fiber properties in order to optimize, operate, and control whole electrospinning procedure. That is to say, it is feasible to estimate fiber characteristics by variation in one or more parameters [112].

As a kind of biomacromolecule extracted from animal tissue such as bone, skin, and muscle, gelatin, is generally used in pharmaceutical, cosmetic, medical, and food applications for its natural abundance, inherent biodegradability in physiological environments and cheapness [112,122]. Since it is a denatured type of collagen, its utilization as scaffolding material may avoid immunogenicity and collagen related pathogen transmission concerns [123]. For these reasons, its great properties can offer potential developments in the area of tissue engineering [124]. In recent past, the scaffolds fabricated from gelatin by using electrospinning have been studied intensively because their three dimensional structure mimic extracellular matrix which is the natural media for a wide range of tissues and they are very attractive for tissue engineering applications [122,125]. Especially, they have attracted much consideration for potential applications in bone regeneration [123].

The nanocomposite structure of bone extracellular matrix consists of collagen fibrils and carbonated hydroxyapatite. This structure forms a framework to design synthetic scaffolds [18]. The use of bioceramics in nanofibrous scaffolds for bone tissue applications is remarkable. Bioceramics have superior biocompatibility and noteworthy bioactivity. Among these materials, bioactive glasses (BG) are the most important ceramics used in orthopedic surgery [126].

Various experimental design methods such as Central Composite, Box-Behnken, and D-optimal designs are widely used in RSM [127]. Among all of the experimental design methods, the Box-Behnken design (BBD) is more beneficial since it takes under consideration the interactions between the parameters including less experimentation [112]. For this reason RSM coupled BBD was utilized to find out the optimum electrospinning operating parameters to get suitable nanocomposite for bone tissue engineering applications. Due to its ability to form hydroxyapatite, BG used as the inorganic phase and gelatin used as the organic phase of nanofiber composite structure. Soluble starch coated silver nanoparticles synthesized by using microwave assisted green synthesis were used to overcome the drawback of the non-antibacterial activity of electrospun gelatin/BG nanocomposite structure and a model equation of fiber diameter is obtained by using electrospinning process parameters.

3.2 Materials and Methods

3.2.1 Materials

Gelatin (Gt, type A, from porcine skin, gel strength 300, G2500), silicon dioxide (SiO_2 , purum p.a., powder), were purchased from Sigma Aldrich. Silver nitrate (AgNO_3 , reagent grade), sodium hydroxide (NaOH , reagent grade, $\geq 98\%$ pellets, anhydrous), acetic acid (glacial 100%), soluble starch (soluble GR for analysis), calcium carbonate (CaCO_3 , precipitated GR for analysis), sodium carbonate (Na_2CO_3 , anhydrous puriss), and di-sodium hydrogen phosphate anhydrous (Na_2HPO_4 , anhydrous GR), tryptic soy broth (TSB, catalog no: 105459), tryptic soy agar (TSA, catalog no: 105458) were all obtained from Merck. All chemicals were used without further purification and the solutions were prepared using deionized water.

3.2.2 Preparation of silver nanoparticles

1 M silver nitrate solution was added into 0.5 wt % soluble starch solution to prepare silver nanoparticles. Thereafter, the pH of the solution was set to 8.5 by using NaOH solution. For the synthesis of silver nanoparticles, Bosch microwave oven (model: HMT882H) was used. The desired solution mixture was reacted in that domestic microwave oven operated at 180 W and a frequency of 2450 MHz, for 1h to obtain silver nanoparticle (Ag-NPs) solution [128].

3.2.3 Preparation of bioactive glass particles

The bioactive glass particles were produced using the melt-quenching process. To prepare these particles, the precursor chemicals were first placed in a platinum crucible in appropriate amounts for 45S5 bioactive glass. They were then melted at 1250°C for 2 hours and quenched rapidly into deionized water to form frits. The prepared frits were then grounded and placed in a platinum crucible to repeat the melting and quenching steps to obtain a homogeneous and amorphous structure. Finally, the prepared bioactive frits were grounded below $45\ \mu\text{m}$ to obtain bioactive glass particles (BG).

3.2.4 Preparation of electrospinning solution

Firstly, gelatin was dissolved at 22 %wt in mixtures of the obtained silver nanoparticle solution and acetic acid at the volumetric ratios of 10/90, 20/80, and

30/70 to prepare gelatin nanofiber composites containing silver nanoparticles. The gelatin polymer solution prepared at 22 % wt/v in acetic acid could not be electrospun because of its very high viscosity. The appropriate solvent content was determined by measuring the average fiber diameters of these nanofibers. The optimization studies to determine operating variables were carried out by adding bioactive glass particles to this solvent mixture at 5% wt/v based on the study of Lepry et al. [129]. The mixtures with BG content were stirred for one hour. After that, the gelatin solution was prepared in these mixtures by stirring at room temperature for 2 h in order to obtain homogeneous solutions.

3.2.5 Electrospinning

The prepared solutions were transferred to plastic syringes equipped with a flat stainless steel needle connected to a high voltage supply. The voltage applied to the needle tip was set between 25-31 kV. The flow rate was adjusted as 0.5-1 mL/h with a syringe pump. The nonwoven electrospun fibers were deposited on an aluminum foil wrapped around a grounded collector positioned perpendicular to the tip at 140-180 mm. The electrospinning process was carried out using an electrospinning apparatus (Nanospinner 24 Touch, Inovenso Co) at 50-55% relative humidity at 23 °C.

3.2.6 Antibacterial tests

The antibacterial tests of Ag NPs containing gelatin composite nanofibers against *Escherichia coli* (ATCC 25922) were performed by disc diffusion method. The bacteria were grown in TSB by incubation for 24 hours at 37 °C. Samples of nanofiber membranes were cut into square shaped discs of 10 mm diameter. TSA plates were inoculated with 100 µl of bacterial suspension containing around 1×10^6 colony forming units (CFU) mL⁻¹ using the spread plate method. The samples were sterilized under UV light (each side for 1 hour) and then put on the inoculated TSA, and incubated at 37 °C for 24 h. Zones of inhibition were assessed and the clear areas formed around each sample were determined.

3.2.7 Box-Behnken design experiments

Box Behnken Design (three factor three level) was utilized to specify the relationship between variables of applied voltage (25-31 kV), flow rate (0.5-1 mL/h) and tip to collector distance (TCD) (140-180 mm) on the average diameter of Gt/Ag-NPs/BG

composite nanofibers. The factor and their levels were determined from the preliminary experiments. These values were chosen based on the electrospinnability of the electrospinning polymer solution. It was observed that there was not enough solvent evaporation at the applied voltages lower than 25 kV, tip to collector distances lower than 140 mm and at the flow rates higher than 1 mL/min. Electric arc formations were observed at applied voltages higher than of 31 kV, tip to collector distances higher than 180 mm and at the flow rates lower than 0.5 mL/min. The mean diameter of the fibers obtained from each experiment was measured and these data were documented in Table 3.1 and Figure 3.1.

The BBD response surface model of electrospinning process refers to the diameter of the Gt/Ag-NP/BG nanocomposites as a function of the parameters mentioned above. The polynomial model for the mean nanofiber diameter according to the electrospinning parameters is expressed in the equation (3.1) as follows:

$$Y = C_0 + \sum_{i=1}^3 C_i X_i + \sum_{i=1}^3 C_{ii} X_i^2 + \sum_{i=1}^2 \sum_{j=i+1}^3 C_{ij} X_i X_j \quad (3.1)$$

where Y is the predicted response and C_0 , C_i , C_{ii} , and C_{ij} are the constant coefficients of the model. X_i , X_{ii} , and X_{ij} are the linear, quadratic and interactive factors of the uncoded variables, individually. The regression coefficient (R^2) was utilized to determine the accuracy of the full quadratic equation.

Minitab 17 statistical software (Minitab Inc., State College) was used to perform the regression and graphical analysis of the obtained data. The statistical meaning of each parameter and the possible interactions between them were evaluated by p-values. Terms with a p-value greater than 0.05 are statistically ineffective on the predictive response. For this reason, the equation was simplified by discarding these terms from the equation. The estimation ability of this simplified equation was determined by three validation experiments using different conditions in the design domain. Surface plots were drawn to imagine the relationship between responses and process parameters. At the end, the process conditions for the production of the optimum fiber diameter, which has the similar fiber size for bone tissue engineering applications, was determined.

3.2.8 Characterization of bioactive glass and nanofiber membranes

The morphology of nanofibrous scaffolds and BG particles were examined by scanning electron microscopy (SEM, JSM-5419, Jeol). Prior to the examinations, the surfaces of the scaffolds and BG particles were spray coated with platinum for 120s (SC7620 sprayer, Quorum Technologies Ltd, United Kingdom). For each nanofiber scaffolds, the average fiber diameter and the standard deviation of the average fiber diameter were measured by the aid of image visualization software (Image-J, National Institutes of Health, USA) from about 50 measurements of random fibers. The functional groups of fibrous membranes and BG particles were investigated by Fourier transform infrared spectroscopy (FT-IR). The FT-IR spectra were collected using a spectrometer (Spectrum 100, Perkin Elmer) in the transmittance mode in the medium IR region ($4000\text{-}650\text{ cm}^{-1}$). Characteristic peaks of Ag NPs containing fibrous membranes and the amorphous structure of BG particles were obtained using an X-ray diffraction analyzer (XRD, Panalitic, Xpert Pro) with Cu-K α radiation. The elemental analysis of the nanofiber structure was performed by EDS analyzer connected to the SEM device. Differential thermal analysis (DTA) of the nanofiber structure and BG particles were carried out with the SDT Q 600 thermal analyzer under nitrogen atmosphere from room temperature (RT) up to 800 °C with a heating rate of 10 °C/min.

3.3 Results and Discussion

3.3.1 Preliminary studies

Most failures of bone implants are associated with postoperative complications associated with high morbidity. The microorganism-induced biofilms formed on the implants can reduce the success of the implants applications [130]. To avoid this problem, many researchers have produced antibacterial nanofiber membranes containing Ag NPs for use in bone tissue engineering applications [24,130-134]. In addition, it has been reported that Ag NPs are effective in cell proliferation with their antibacterial effect. In this context, Cheng et al. reported that Ag NPs interact with bone marrow derived stem cells located around the implant and increase cell proliferation [132] and Kwak et al. showed that the contribution of Ag NPs to proliferation of L929 fibroblast cells was also effective [135]. For this reason, it was aimed to fabricate gelatin nanofibers containing Ag NPs and BG particles for bone

tissue engineering applications due to their antibacterial and cell proliferation potential.

Firstly, 22% gelatin solutions were prepared in 10/90, 20/80 and 30/70 Ag NPs solution and acetic acid mixtures as preliminary experiments to find out the most suitable silver-containing gelatin nanofiber membrane. As seen in Figures 3.1(a-c) the mean fiber diameter of the obtained nanocomposites was reduced by Ag NPs addition and measured as 1530 ± 652 nm, 878 ± 255 nm, and 338 ± 89 nm, respectively.

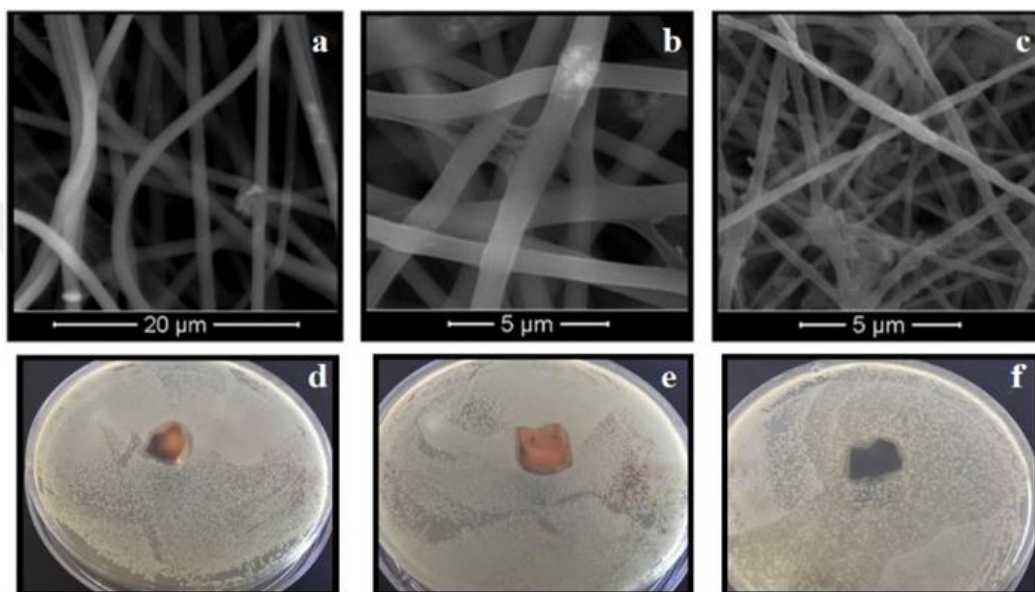


Figure 3.1 : SEM images of Gt/Ag-NPs nanofibers electrospun in mixtures of Ag-NPs solution and acetic acid at volumetric ratios of 10/90 (a), 20/80 (b) and 30/70 (c) and antibacterial tests of Gt/Ag-NPs nanofibers electrospun in mixtures of Ag-NPs solution and acetic acid at volumetric ratios of 10/90 (d), 20/80 (e) and 30/70 (f).

Furthermore, antibacterial tests against *E. coli* were carried out with the gelatin nanofiber membranes electrospun in mixtures Ag NPs solution and acetic acid at volumetric ratios of 10/90, 20/80 and 30/70. Neat gelatin nanofibers could not be produced because it could not electrospun using only acetic acid as the solvent. According to these tests, the inhibition zones surrounding the fiber membranes can be clearly observed Figures 3.1(d-f). After determination of the antibacterial activity of the nanofiber membranes against *E. coli* and considering the size similarity to the bone tissue extracellular matrix, BBD design experiments were performed by using the mixture of Ag NPs solution and acetic acid at the volumetric ratio of 30/70 by adding 5 % (wt/v) BG particles content.

3.3.2 Development of RSM models

In this study, gelatin nanocomposites containing Ag NPs and BG particles were electrospun at each design point (applied voltage, TCD and flow rate) and at three BBD levels resulted in 15 possible combinations. As can be seen from the Table 3.1 and Figure 3.2, it was clear that the fibers in this study were obtained at diameters ranging from 430 ± 89 nm to 543 ± 91 nm.

The experimental results were analyzed statistically using variance of analysis (ANOVA) to determine the probability of significance (p-values) of each terms and the full quadratic response surface model can be seen from Table 3.2. The significance of each term was decided according to the p-values. The terms with p-value less than 0.05 at the interval of 95% confidence indicate that the terms of the model are statistically significant and have significant effects on the dependent variable [12,106,110,112,136]. The fact that the R^2 and adjusted R^2 values were close to each other indicated the compatibility of the model equation with the experimental results [137]. The R^2 and adjusted- R^2 were found as 0.9641 and 0.8995, respectively.

Model reduction is a common technique for modelling within the case of various insignificant terms. The removal of insignificant terms will increase the effectiveness of the model [106]. The obtained ANOVA results of the response at different levels were given in Table 3.3 and the equation of linear and quadratic terms for the three electrospinning parameters in uncoded variables was found in equation (3.2).

$$Y = 578 + 157.7X_1 - 33.5X_2 - 26.72X_3 - 3X_1^2 + 0.0844X_3^2 \quad (3.2)$$

where X_1 , X_2 , X_3 and Y are applied voltage (kV), flow rate (mL/h), TCD (mm), fiber diameter (nm) respectively.

The ANOVA results show that the two quadratic terms (X_1^2 and X_3^2) and the linear term X_1 exhibit significant effects on the mean fiber diameter at $p < 0.05$. Furthermore, the p-value of the model was found to be 0.004, which implied that the model was significant. This means that the probability of occurrence of a small p-value due to noise is low [12].

The fit of the model was assessed using the regression coefficients. The high value of $R^2 = 0.9641$ and R^2 adjusted = 0.8995 showed the high reliability of the model when the mean fiber diameter was estimated.

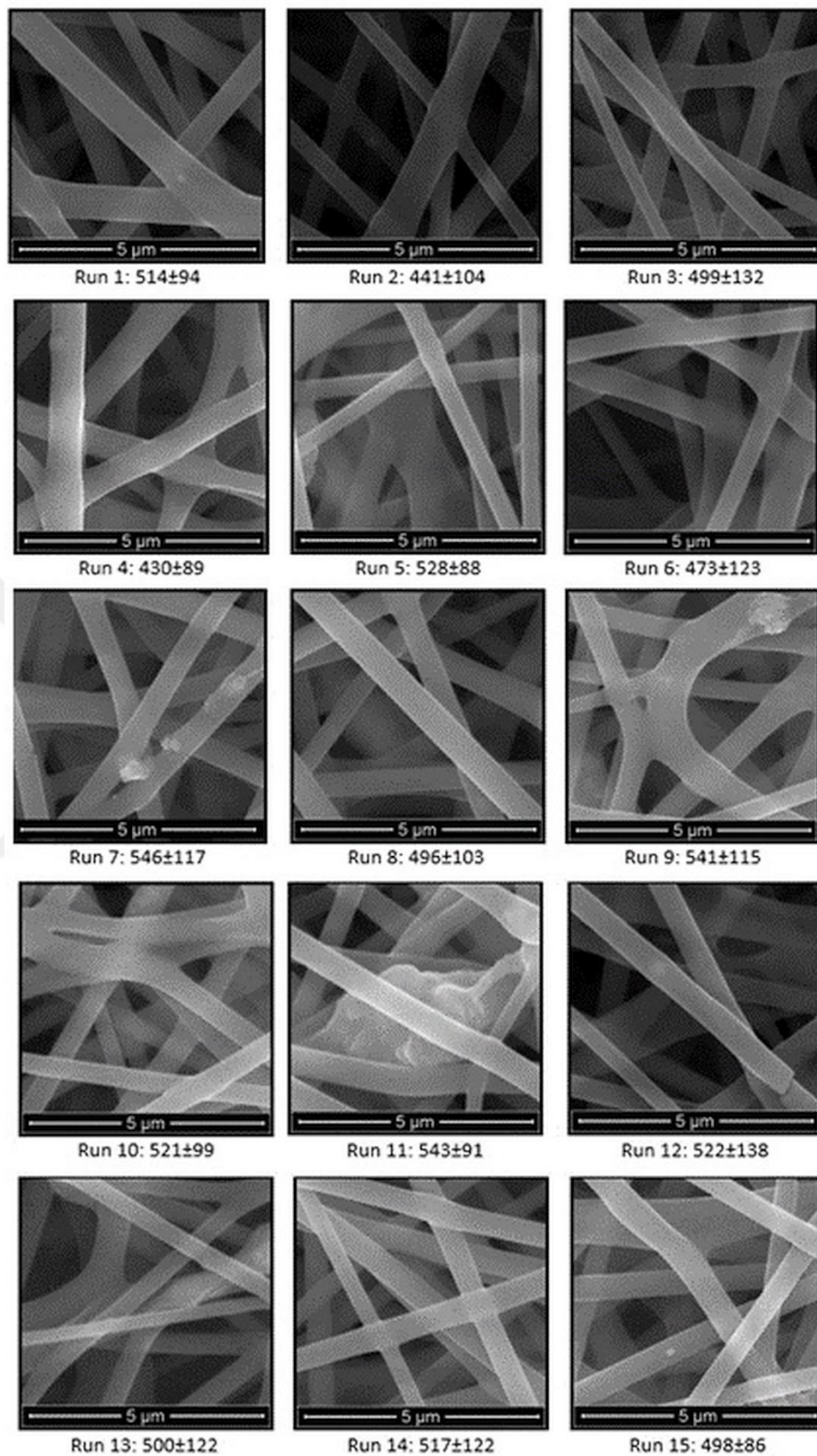


Figure 3.2 : SEM images of Gt/Ag-NPs/BG nanocomposites in various electrospinning conditions based on Box-Behnken-design.

Table 3.1 : The BBD design experiments and results.

Run	Voltage, X ₁ (kV)	Flowrate, X ₂ (mL/h)	TCD X ₃ (mm)	MFD ¹ (nm)	CFD ² (nm)
1	25	0.50	160	514	513
2	31	0.50	160	441	452
3	25	1.00	160	499	497
4	31	1.00	160	430	435
5	25	0.75	140	528	533
6	31	0.75	140	473	471
7	25	0.75	180	546	544
8	31	0.75	180	496	482
9	28	0.50	140	541	538
10	28	1.00	140	521	521
11	28	0.50	180	543	549
12	28	1.00	180	522	532
13	28	0.75	160	500	501
14	28	0.75	160	517	501
15	28	0.75	160	498	501

¹MFD: Measured Fiber Diameter, ²CFD: Calculated Fiber Diameter by the model equation

Table 3.2 : ANOVA results for the experimental response at different levels.

Source	DF	Seq SS	Adj MS	F	P
Regression	9	16055.9	1783.98	14.92	0.004
Linear	3	8429.3	2809.75	23.50	0.002
X ₁	1	7626.1	7626.13	63.79	0.000
X ₂	1	561.1	561.13	4.69	0.083
X ₃	1	242.0	242.00	2.02	0.214
Square	3	7616.1	2538.70	21.24	0.003
X ₁ ²	1	3229.3	2792.31	23.36	0.005
X ₂ ²	1	304.7	156.00	1.30	0.305
X ₃ ²	1	4082.1	4082.08	34.15	0.002
Interaction	3	10.5	3.50	0.03	0.992
X ₁ X ₂	1	4.0	4.00	0.03	0.862
X ₁ X ₃	1	6.3	6.25	0.05	0.828
X ₂ X ₃	1	0.3	0.25	0.00	0.965
Residual error	5	597.7	119.55		
Lack-of-fit	3	379.7	126.58	1.16	0.494
Pure error	2	218.0	109.00		
Total	14	16653.6			
				Model evaluation	
				R ²	0.9641
				R ² adjusted	0.8995
				R ² predicted	0.6057

Table 3.3 : ANOVA results after elimination of insignificant terms for the experimental response at different levels.

Source	DF	Seq SS	Adj MS	F	P
Regression	5	15889.4	3177.87	37.42	0.000
Linear	3	8429.3	2809.75	33.09	0.000
X ₁	1	7626.1	7626.13	89.81	0.000
X ₂	1	561.1	561.13	6.61	0.030
X ₃	1	242.0	242.00	2.85	0.126
Square	2	7460.1	3730.05	43.93	0.000
X ₁ ²	1	3229.3	2707.71	31.89	0.000
X ₃ ²	1	4230.8	4230.80	49.82	0.000
Residual error	9	764.3	84.92		
Lack-of-fit	7	546.3	78.04	0.72	0.691
Pure error	2	218.0	109.00	Model evaluation	
Total	14	16653.6		R ²	0.9542
				R ² adjusted	0.9286
				R ² predicted	0.8768

The quadratic term (X₂²) and interaction terms (X₁X₂, X₁X₃ and X₂X₃) were found to be insignificant and eliminated to find out a modified regression model. ANOVA of the modified regression model showed that R² value was 0.9542, indicating that the model could account for 95.42 % of the data variation and only 4.48 % of the total values were not explained by the model [138]. The values of the R² adjusted (0.9286), R² predicted (0.8768) confirm that the model is very meaningful, indicating a good agreement between experimental and predicted fiber diameters.

When the regression coefficient values before and after the modification of the model were examined, it was clear that the regression coefficient value for the new model was lower than the regression coefficient of the model containing all of the interaction terms. The R² value increases not only by the suitability of the responses but also with the increase of the number of terms. Hence, after elimination of the insignificant terms smaller R² values were anticipated for the new model, due to the less terms [112].

The R² value should not be less than 0.75 for a model to be sufficient. However, this does not mean that a great value of R² is always good for the regression model, and such an inference can only be made based on the R² adjusted value, which has a similarly high value. Thus, the model is sufficient for predicting the interval between experimental variables. In addition, R² adjusted and R² predicted should be within 20% to reach good agreement [138]. This requirement is met with a R² predicted (0.8768) in this study. The model offers 87.68% variability in estimated fiber diameter change beyond the range of experimental electrospinning operation conditions. Moreover, the model showed a good agreement with data because the lack of fit has F (0.72) and P

(0.691) values which are higher than 0.05 showing that the probability of the error was not significant. Besides, the model has the p-value of 0.000 proving the validity of the model. For this reason, the existing quadratic model can be used in the range of the design space [107].

3.3.3 Verification of experimental and model data

Figure 3.3(a) shows the relation between the measured values and model determined values of the mean fiber diameters by linear regression coefficient ($R^2=0.969$). The normal probability plot of residuals was given in Figure 3.3(b). The relation showing that the experimental values have good grade of fit with the model determined data implying the compatibility of the model equation with the experimental data [12,102,106,136].

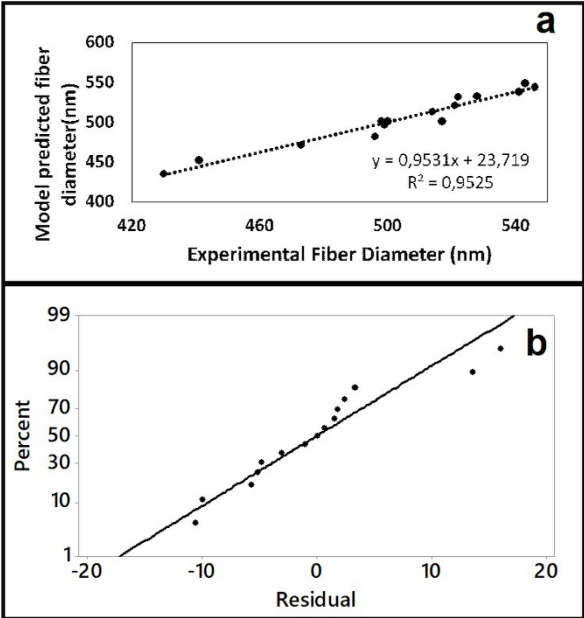


Figure 3.3 : Plot of model predicted fiber diameter against experimental fiber diameter (a) and normal probability plot (b).

Besides, the data points are on a straight line in the normal probability plot. This plot shows that the errors have a normal distribution [12]. Furthermore, the correspondence between both the experimental results and the results obtained by the model equation were determined by the verification experiments (Table 3.4). Thus, it was concluded that the model was created correctly.

Table 3.4 : Results of validation experiments.

Run	Voltage (kV)	Flowrate (mL/h)	TCD (mm)	M.D ^a (mm)	C.D ^b (mm)
1	31	1.00	180	470±112	474
2	25	0.50	140	513±150	541
3	28	1.00	160	493±113	493

^a M.D: Measured Diameter. ^b Calculated Diameter

3.3.4 Effect of electrospinning parameters on the nanofiber diameter

Three of electrospinning operation parameters, including applied voltage, flow rate, and TCD were used at three levels to determine their effects on the mean diameter of the electrospun Gt/Ag-NPs/BG composite nanofibers. The effect of the electrospinning parameters were determined by the p-values of the factors in the model. According to the p-values, the linear effect and quadratic effect of the applied voltage had significant effects on the nanofiber diameter. It was seen that the linear term had a positive value and the quadratic term had a negative value. A decrease in diameter was determined by the voltage increase. This suggests that the quadratic effect is more dominant than the linear effect for the applied voltage. Only the linear effect was found to be effective for the flow rate. However; it was appeared that the effect of the TCD was not significantly effective linearly but it was quadratically effective. Linear by linear effects (X_1X_2 , X_1X_3 , X_2X_3) appear to be ineffective on the nanofiber diameter.

The change of the parameters between +1 and -1 levels was examined by leaving the other variables constant to figure out the effect of each parameter on the mean fiber diameter, Thus, the effect of the electrospinning parameters could be arranged as one parameter at a time graphs. A curvature or a steep slope in a parameter indicated that this parameter is sensitive to the response. A relatively straight line proves the insensitivity against the change in the parameter [106].

The effect of applied voltage varying at 25-31 kV on the formation of electrospun fibers can be seen from Figures 3.4 (a-c). As seen in this figure, the fiber diameters tend to decrease for each case with the increase at the applied voltage. The applied voltage has two opposite impacts on the fiber diameter. To begin with, increasing the applied voltage increases the electrostatic force, moreover, it creates fibers with smaller diameter. Besides, at the same time, the needle draws more solutions out, hence increasing the diameter. The diameter decreases with the dominance of the first

impact. On the other hand, due to the dominance of the second impact, the diameter increases [112]. It was concluded that the first impact was effective because it was seen that the fiber diameter decreases as the voltage increases in the voltage ranges of the design space.

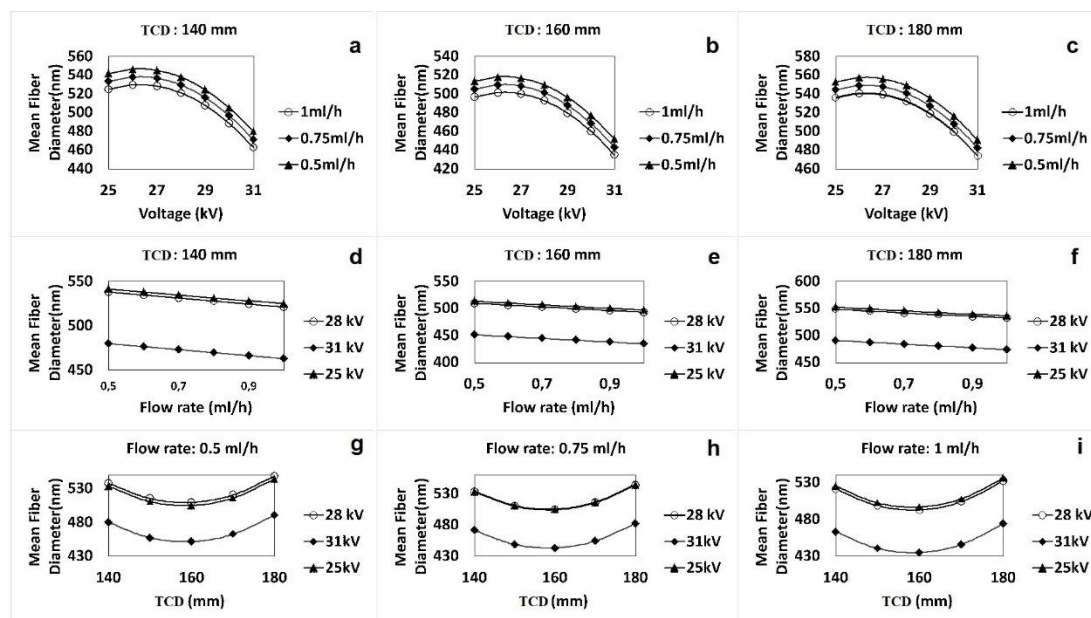


Figure 3.4 : The effect of applied voltage (a-c), flow rate (d-f) and TCD (g-i) on the diameter of electrospun Gt/Ag-NPs/BG composite nanofibers for different experimental conditions.

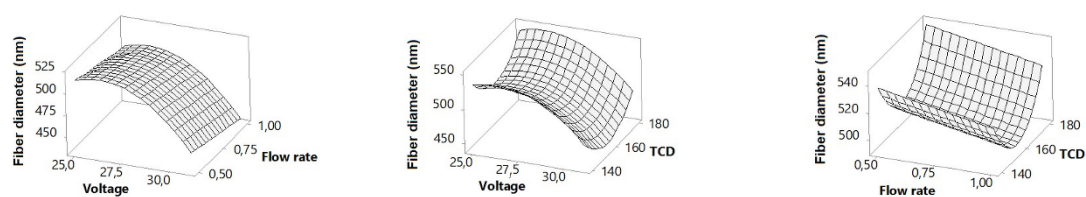
The nanofiber diameter was expected to increase as the feed rate increases [17]. However, it was determined from the p-value results, the coefficients of the model equation and the one parameter at a time graphs that the fiber diameter size decreased linearly with the increase of feed rate as given in Figures 3.4 (d-f). This may be related to the presence of silver nanoparticles and bioactive glass, which increases the conductivity of the solution [76,86,139-141]. In this case, it is possible that the feed rate cannot overcome the fiber diameter reduction effect of silver nanoparticles and bioactive glass [17].

TCD has a direct impact on the jet flight time and electric field strength. A decrease in this value abbreviates solvent evaporation time and flight time, and increases the electric field strength, which comes about in more bead formation. The impact of decreasing TCD is nearly the same as the increase of voltage [142]. As seen in Figures 3.4 (g-i), the fiber diameter was increased at TCD values higher than 160 mm. The formation of larger nanofibers at lower TCD values than 160 mm could be attributed to the inadequacy of the solvent evaporation due to the low TCD before it reached to

the collector. With the increase of TCD, the smaller nanofibers were formed due to efficient solvent drying. Also, the reason for the formation of larger nanofibers at high TCD values was the intensity decrease of the electrical force on the spinning solution [118].

3.3.5 Surface plots

Figure 3.5 shows the 3-D surface plots of the response (mean fiber diameter) for the parameters (two-parameter time). The plots appear the relation between the two parameters at the central level of the third parameter. 3D surfaces have been progressed by combining equal response points [112]. The surface plot of predicted mean fiber diameter versus applied voltage and flow rate showed that with increasing the voltage and the flowrate the mean fiber diameters were decreased. The main parameter of the decrease in fiber diameter might be the increasing the stability of the jet solution resulted in the formation of thinner fibers. The surface plot for applied voltage and TCD showed that with the increase in TCD and applied voltage, the mean fiber diameter first increased and at higher TCD, that is greater than 160 mm, the mean fiber diameter increased. The surface plot for flow rate and TCD showed that the middle TCD and the highest flow rate had a decreasing effect on the fiber diameter. Based on these observations the parameters to fabricate fibers with the minimum and maximum values were determined.



Hold values: Voltage 26 kV, Flow rate 0.75 mL/h, TCD: 160 mm

Figure 3.5 : Surface plots of the response variable (fiber diameter(nm)) for various electrospinning paramaters (two factor at a time). (applied voltage-flowrate, applied voltage-TCD, flowrate-TCD).

3.3.6 Optimization of Gt/Ag NPs/BG nanofiber membrane fabrication

The nano-scale bone tissue structure has collagen fibers, which are surrounded and infiltrated with minerals [2]. It has been proved that it is important to imitate the nanostructured collagen structure (50-500 nm) from bone components in bone tissue

scaffolding [25]. By solving the equation, the optimum applied voltage, TCD and flow values were found for minimum and the maximum fiber diameters. The nanofiber membranes with minimum mean fiber diameter of 434.5 nm could be fabricated by using the optimum values for applied voltage of 31 kV, flow rate of 1 mL/h, and the TCD 158 mm. The optimum values to fabricate the maximum diameter (557 nm) were found for applied voltage, flow rate and TCD as 26 kV, 0.5 mL/h, 180 mm, respectively. As a result, it can be said that due to the size similarities with collagen fibers the parameters to fabricate maximum fiber diameter was proper parameters for bone tissue engineering applications [143].

3.3.7 Characterization of 45S5 bioglass particles

The morphology and the content of the BG particles were determined by SEM analysis and EDS analysis. SEM image of 45S5 BG particles can be seen from Figure 3.6(a). As shown in the figure, the BG particles have irregular morphology and contain a large number of heterogeneous particles whereas most of the 45S5 BG particles had a size range between 4.7 and 53.3 μm (mean $24.7 \pm 11.3 \mu\text{m}$). EDS analysis was performed on the BG particles and the results were presented in Figure 3.6(b). The EDS analysis results showed the traces of the sodium (Na), Silicon (Si), Phosphorus (P), Calcium (Ca) elements in the produced glass, It can be also clearly said that the composition of the elements in the structure of the produced glass is similar to the almost 45S5® bioactive glass composition.

The experimental FTIR spectrum of the bioglass (Figure 3.6(c)) consisting of silicate (45 wt% SiO_2) network and phosphate network (6 wt% P_2O_5) has the Si-O bending mode located in 703 cm^{-1} . The band between 765 and 960 cm^{-1} is associated with Si-O having one non-bridging oxygen. The Si-O-Si stretching vibration mode is found at 1005 cm^{-1} . The complex absorptions between 1350 cm^{-1} to 1550 cm^{-1} originate from the carbonate groups. The broad band in the range 1590 - 1715 cm^{-1} refers to molecular water [144]. The glass transition and crystallization temperatures of bioactive glass particles were also determined by DTA. Based on the DTA thermogram of the BG particles given in Figure 3.6(d), the glass transition temperature of the BG particles was $624.90 \text{ }^\circ\text{C}$, while the crystallization temperature was $719.44 \text{ }^\circ\text{C}$, indicating the glass's crystallization ability [145]. XRD pattern of the 45S5 BG particles given in Figure 3.6(e) showed no sharp diffraction peaks were observed, indicating that the BG

particles had a typical amorphous structure of the silicate glass appearing at about 30° theta as a wide peak meaning that the synthesized glass particles have high purity [146,147].

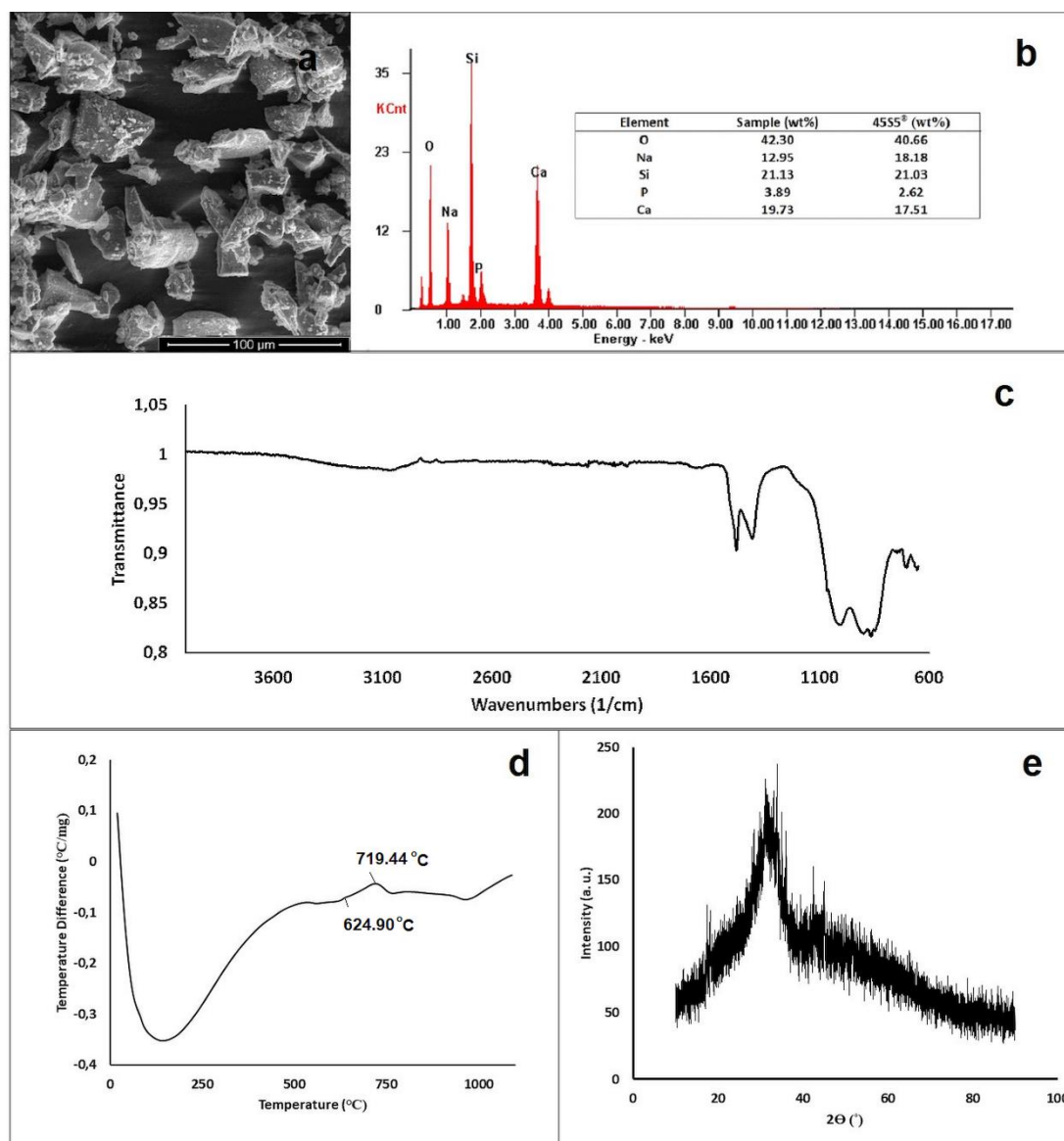


Figure 3.6 : Characterization studies of BG particles including SEM analysis (a), EDS analysis (b), FTIR measurements (c), DTA analysis (d), and XRD analysis (e).

3.3.8 Characterization of optimized Gt/Ag-NPs/BG nanofiber membrane

The nanofiber membrane was fabricated by using optimum conditions found with the model by Box Behnken Design and the characterization studies of this structure were performed. When the SEM image of this nanofiber structure (Figure 3.7(a)) was examined, it was determined that the average fiber diameter was 472 ± 94 nm. When the nanofiber diameter calculated by the model (557 nm) compared with the fiber

diameter of the fabricated nanofiber membrane at the optimum variables, it was seen that the diameter of the optimized nanocomposite calculated by the model appeared to be in the measurement range of the nanofiber membrane fabricated at the optimum variables. This result proves the correctness of the model.

In addition, the crystalline structure of the electrospun gelatin nanofiber doped with Ag NPs and BG was determined using the XRD analysis shown in Figure 3.7(b). In the XRD pattern of the electrospun membrane, the diffraction peak at around $2\Theta=20^\circ$ with an expanded band is shown due to the amorphous structure of the gelatin. The X-ray diffraction of the Gt/Ag-NPs/BG sample shows three of the Bragg reflection peaks at 38.8° , 44.9° and 65.1° separately from the gelatin peak, corresponding to the (111), (200), (220) planes of the face centered cubic structured metallic silver [128,148]. Using the Scherrer equation, the mean Ag NPs crystallite size in the nanofiber structure was estimated with the full widths at the half-maximum of the characteristic peaks (111), (200) and (220) [148].

As a result, the average silver size in the nanofiber membrane was calculated approximately 19.3 ± 1.3 nm, which showed that the size of the Ag NPs in the nanofiber membrane was the similar to the Ag NPs average size of the 19 ± 6 nm obtained in our previous study [128]. FTIR measurements were performed to identify the functional groups of Gt, Gt/Ag-NPs and Gt/Ag-NPs/BG nanofiber membranes (Figure 3.7(c)). As can be seen from the figure, the bands of the raw gelatin nanofiber membrane were detected at 1635 , 1538 , 1450 , 1334 , 1242 , 1202 and 1082 cm^{-1} which correspond to the amide I, amide II, C-N stretching vibrations of the amines, wagging vibrations of proline side chains, amide III, vibrations of C-N and N-H group linked with amide plane of amide III or the vibrations of the glycine CH_2 groups and vibrations related with primary amine, respectively. In addition to that a broad band is appeared between 3100 - 3700 cm^{-1} due to N-H stretching band of amide bond [149,150].

As compared with Gt/Ag-NPs nanofiber membrane the FTIR spectrum of neat Gt nanofiber membrane is identical with the spectrum of Gt/Ag-NPs nanofiber membrane (Figure 3.7(c)). When the FTIR spectrum of the Gt/Ag-NPs/ BG nanofiber membrane was examined, it was observed that the density of the Gt characteristic bands decreased with BG addition. It was found that Ag NPs and BG was successfully participated in the nanocomposite structure in the characterization studies to determine the effect of

Ag addition and BG addition. FTIR spectra showed that the Ag NPs addition was not effective on the functional groups in the gelatin nanofiber structure, but BG content had the effect of reducing the density of the functional groups. It can be argued that the characteristic bands of the BG are not visible is because of the overlapping Gt bands [151,152].

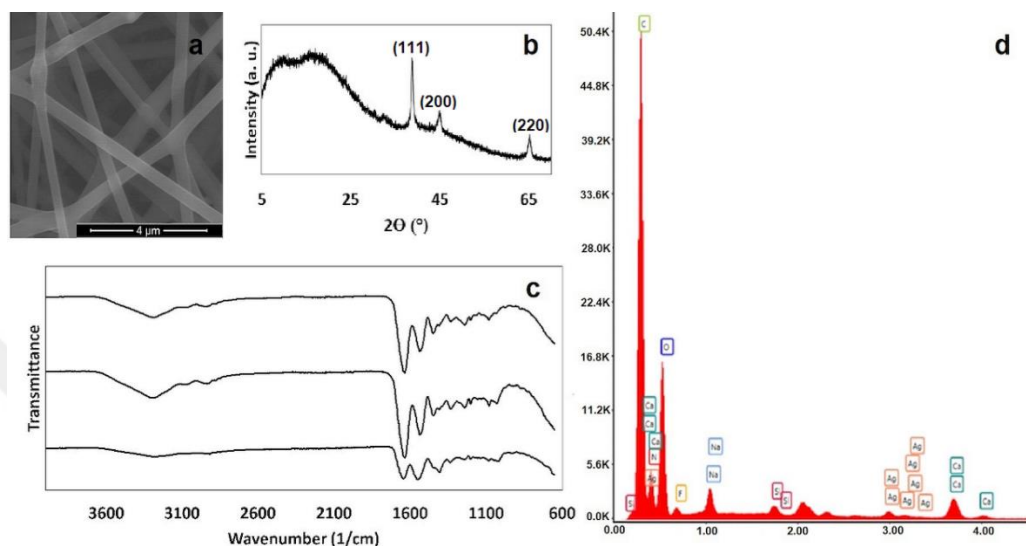


Figure 3.7 : (a) SEM image of the optimized Gt/Ag-NPs/ BG nanofiber membrane; (b) XRD analysis of the optimized Gt/Ag-NPs/ BG nanofiber membrane; (c) FTIR spectra of Gt nanofiber membrane (*i*), Gt/Ag-NPs nanofiber membrane (*ii*) and Gt/Ag-NPs/BG nanofiber membrane (*iii*); (d) EDS analysis of the optimized Gt/Ag-NPs/ BG nanofiber membrane.

The EDS analysis given in Figure 3.7(d) was performed to find out the chemical composition of the structure. As a result of this analysis, the presence of Ag, as well as Si, Ca, Na elements were determined. In addition, the amount of silver in the structure was determined as 0.68 wt%. When the studies on the production of scaffolds by various methods using Ag nanoparticles in their structures, which were designed for use in bone tissue cells, were investigated, it was observed that cytotoxicity was related to silver concentration [134]. For example, while Marsich et al. [153] and Bakare et al. [154] found a 0.05% silver ratio for their bone tissue structure composites, Hasan et al. [155], Alt et al. [156] and Gao et al. [157] stated that 1% and 2.5% Ag content suitable for bone tissue applications. Based on these data, the nanocomposite structure obtained in this study has the potential to be used in bone tissue applications.

Furthermore, thermogravimetric analysis (TGA) and differential thermogravimetric analysis (DTG) methods given in Figure 3.8(a,b) were used to determine the content of bioactive glass particles and the thermal behavior of the Gt, Gt/Ag-NPs and Gt/Ag-

NPs/BG nanofiber membranes. The obtained temperatures showing the maximum degradation of these nanofiber membranes were given in Table 3.5. When the char yields of Gt/Ag-NPs and Gt/Ag-NPs/BG nanocomposites were compared, the difference between these two values found as 18.62, giving the percentage of bioactive glass particles in the structure. Based on the literature studies, Lepry et al. reported that the minimum bioactive glass content required for hydroxyapatite conversion was 12.5% [129]. In addition, El-Kady et al. showed that bioactivity can be obtained with 20% bioactive glass content at the scaffold they fabricated [158]. In the light of these results, it can be concluded that the scaffold obtained in this study has the potential to have bioactive behavior. When DTG curves were examined, it was determined that nanocomposites were degraded in two stages. The first maximum decomposition temperatures (T_{d1}) indicated the removal of the absorbed water, bound water as well as NH_3 and CO_2 . In the second stage (T_{d2}), breakdown of protein chains, deterioration of peptide bonds and carbonization occur [159,160]. As a result of examination of the second maximum decomposition temperatures, it was seen that the decomposition temperature of gelatin did not change with the addition of Ag NPs but the degradation occurred at lower temperature with the addition of the BG particles. The change in the decomposition temperature of the Gt/Ag-NPs/BG with the BG particles addition showed that the bioactive glass content interacted with gelatin to promote the degradation of gelatin [161]. It can be concluded that the production of the composite was successfully achieved with the formation of the molecular interaction between BG particles and gelatin.

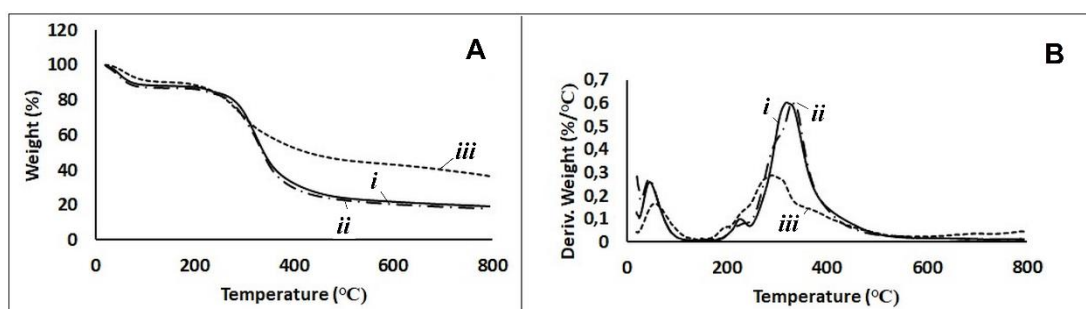


Figure 3.8 : (a) TGA of Gt nanofiber membrane (i), Gt/Ag-NPs nanofiber membrane (ii) and Gt/Ag-NPs/BG nanofiber membrane (iii), (b) DTG of Gt nanofiber membrane (i), Gt/Ag-NPs nanofiber membrane (ii) and Gt/Ag-NPs/BG nanofiber membrane (iii).

Table 3.5 : Degradation temperatures of Gt, Gt/Ag-NPs and Gt/Ag-NPs/BG nanofiber membranes.

Sample	T _{d1} (°C)			Weight loss (%)	T _{d2} (°C)			Weight loss (%)	Char yield(%)
	T _{onset}	T _{max}	T _{end}		T _{onset}	T _{max}	T _{end}		
Gt	RT	44.7	114.1	11.65	176.2	225.3	533.7	64.7	19.24
Gt/Ag-NPs	RT	43.7	115.0	13.02	181.7	320.7	518.9	62.8	17.89
Gt/Ag-NPs/BG	RT	58.6	141.0	9.76	141.0	290.1	551.3	47.7	36.51

The bone scaffold suitable for bone regeneration must have sufficient mechanical properties to meet bone tissue requirements [162]. To improve the tensile properties of the Gt/Ag-NPs/BG nanofiber membrane, crosslinking treatment was applied on the nanofiber membrane by using glutaraldehyde vapor (50 % wt) at room temperature for 2 h. Figure 3.9 depicts the tensile tests carried out on the optimized neat Gt/Ag-NPs/BG nanofiber membrane and crosslinked Gt/Ag-NPs/BG nanofiber membrane. The elastic modulus of the nanofiber mats were calculated from the slope of the linear portion of the stress-strain curve. The tensile strength and elastic modulus of the neat Gt/Ag-NPs/BG nanofiber membrane were found as 2.46 MPa and 126.94 MPa, respectively. After the crosslinking treatment the tensile strength and elastic modulus of this membrane were found as 4.08 MPa and 154.12 MPa, respectively. A significant increase was observed after the crosslinking treatment.

The electrospun scaffold obtained in this study has a potential to be used for bone regeneration of low and/or non-load bearing areas (trabecular bone), since the load-bearing natural bone (cortical bone) has very high tensile properties [163]. The cortical bone structure is composed of inorganic crystalline minerals containing very few osteocytes and blood vessels [7]. It has tensile strength of 107-140 MPa and elastic modulus of 10-20 GPa [164]. The trabecular bone located in the center of cortical bone structures is composed of a porous trabecular network and bone marrow filling and it has an elastic modulus of 0.01-0.9 GPa [7,164]. Furthermore, Shkarina et al. mentioned about tensile properties of various human bones in their study. Accordingly, they reported that tensile strength of fresh frozen trabecular bone, tibia for the male group and fresh frozen cancellous bone were 1-13 MPa, 0.2-6.7 MPa and 1.8-63.6 MPa, respectively, and they suggested that the nanofiber membrane they fabricated could be used for the bone structures match with the tensile strength of this nanofiber

membrane [165]. In this context, the nanofiber obtained in this study is thought to have the potential to be used in bone tissues have a tensile strength of 4.08 MPa and elastic modulus of 154.12 MPa. It has the potential to be used in cartilage and bone repair applications where mechanical strength is not required [7]. In applications that require high mechanical strength, it is recommended to produce multiple layers with mechanically resistant biopolymers or use mechanically competent 3D printed meshes [166,167].

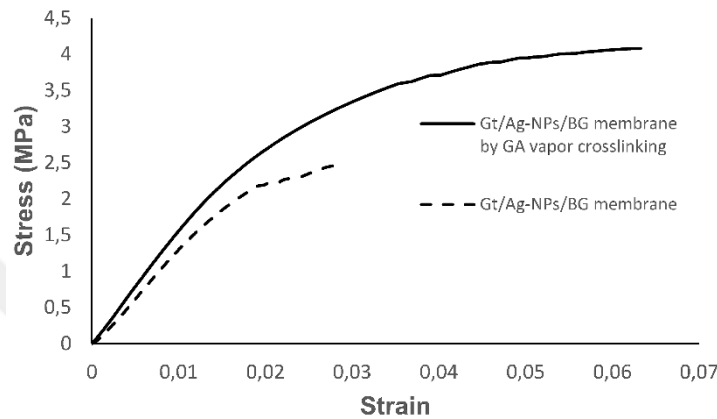


Figure 3.9 : Stress-strain curves of the optimized nanofiber membranes.

3.4 Conclusion

In the current study, response surface methodology was employed as an optimization method for finding the process parameters that yielded the nanocomposite fibers with maximum diameter. In this context, a three-level, three-variable Box-Behnken design was adopted to express fiber diameter as a function of applied voltage, tip-to-collector distance (TCD), and flow rate. The construction of a model that describes the effects of process parameters allows us to represent the effect of parameters in a simple and systematic manner and to predict the experimental results with different parameter combinations. Hence, this work will serve as a beneficial guideline to select the most convenient parameter settings to fabricate the Gt/Ag-NPs/BG nanocomposite membranes with targeted mean fiber diameter. Characterization studies showed that the nanocomposite scaffold was successfully fabricated with the light of the optimum process parameters which may find uses as scaffold in bone tissue engineering applications. Moreover, the detailed biocompatibility tests will be performed on the fabricated nanofiber for future studies.

4. SYNTHESIS AND ANTIFUNGAL ACTIVITY OF SOLUBLE STARCH AND SODIUM ALGINATE CAPPED COPPER NANOPARTICLES³

4.1 Introduction

Metallic nanoparticles (MNPs) have outstanding chemical, physical, thermal and optical properties due to their large amount of high-energy surface atoms relative to bulk solid and they have been used in various applications such as engineering photovoltaic technology, electronic, information storage, catalytic, chemical, environmental technology, biosensors, medicine and biomedical fields [168,169]. While most of these applications prefer noble metals such as gold (Au) and silver (Ag), the high cost of these metals is a major limitation in their large-scale production. Preparation of copper nanoparticles (Cu NPs) has become a thrust area in material investigations, as they are thought to be a possible exchange of Au NPs and Ag NPs in various potential applications such as catalysts, diagnostic, conductive inks and therapeutic applications [169,170].

Copper is a fundamental component encountered in plant and animal tissues. The human body has a copper metabolism active in proteins and other biomolecules that have key catalytic and basic roles. According to certain limits, there are mechanisms in the human body that provide protection against copper toxicity at cellular, tissue and organ levels. Cu NPs have been reported to have antibacterial effects comparable to Ag NPs in single *E. coli*, *B. subtilis* strains *Staphylococcus* species and similar antifungal properties [171,172]. Upon the achievement of stable Cu NPs as suitable biomaterials part, they can be anticipated in biotechnology and medicine [173].

Cu NPs have been synthesized by various recognized techniques such as thermal decomposition, microwave heating, radiation methods, micro-emulsion techniques, reverse micelles, electrode discharge, photochemical reduction, gamma radiolysis, laser irradiation, electrochemical techniques, sonochemical reduction, polyol process,

³ This chapter is based on the article “Akturk, A., Karbancıoğlu Güler, F., Erol Taygun, M., Goller, G., Küçükbayrak, S. (2020). Synthesis and antifungal activity of soluble starch and sodium alginate capped copper nanoparticles. *Materials Research Express*, 6, 12”

and chemical reduction [168,174-177]. Within these techniques, the chemical reduction strategy is the most conventional and practical way to synthesize Cu nanoparticles due to its predominant properties such as simple processing, high yield, high quality products, basic and finite equipment and straightforward control method [168,176]. The major drawback with their preparation and protection is their immediate oxidation to CuO or Cu₂O when exposed to the air [168,178]. In order to avoid oxidation, these processes are usually carried out in non-aqueous medium, reaction solutions were carefully deoxygenated and all processes were performed under rigorous protection of an inert environment or in presence of reducing, capping or protecting agents (polymers, surfactants)[168,177,178]. In this regard, dispersants and modifiers are used as surfactants in the synthesis of copper nanoparticles. However the processes performed with surfactants require organic media and metallic precursors, which decompose at elevated temperatures [169]. For this reason, cetyltrimethylammonium bromide (CTAB), polyethylene glycol 8000 (PEG8000), sodium dodecyl sulfate (SDS), and polysorbate 20 (Tween 20) were reported as the soluble surfactants in the copper nanoparticle synthesis [169,179]. Furthermore, the use of natural and synthetic polymer surfactants and ligands as stabilizers in aqueous media also prevents agglomeration by producing well-dispersed metal nanoparticles with high stability [180]. It is also possible to synthesize copper nanoparticles in aqueous medium by leaf extracts and fruit extracts due to metabolites (flavonoids, proteins, terpenoids, tannins and polyphenols) in their structures [168,181].

The interaction of nanoparticles with proteins and enzymes within mammalian cells inhibits the antioxidant defense mechanism. Eventually apoptosis (programmed cell death) or necrosis happens. Toxicity of nanoparticles is regulated by using capping agents [182]. Uncapped nanoparticles are very sensitive to environmental factors (e.g., pH, temperature, electrolytes and solvent) and aggregate easily [183]. To increase the in vivo stability, circulation lifetime and cellular uptake of nanoparticles, particles may be incorporated into or on the surface of liposomes or capped with non-toxic biocompatible macromolecules like polysaccharides or proteins [182]. The studies carried with nanoparticles have pointed that the nontoxic or toxic nature of nanoparticles depend on the capping agent and dosage [183]. For example, while chitosan loaded copper nanoparticles and Ag-Dendrimer nanocomposites show toxicity, Ag-polysaccharide nanocomposites and copper-starch conjugates have non-

toxic nature [182,183]. Due to having biocompatibility, stability and biodegradability, renewable polymers such as polysaccharides, cellulose, starch, and chitosan can be used in various formulations depending on their superior properties [171,184].

Furthermore, the resistance of microorganisms increases as a result of misuse of antibiotics. So therapeutic solutions of fungal infections need to be presented. Among all fungal infections, *Candida* species are both common and highly effective microorganisms on human health [185]. In the case of immune system efficiency occurs, these pathogenic microorganisms cause a disease known as candidiasis [186,187]. Similarly, *Candida* species attack and colonize in medical devices such as peripheral and central vascular catheters utilized in the treatment of patients under chemotherapy, hemodialysis and parenteral nutrition [186]. Cu is a broad-spectrum biocide that successfully prevents the growth of bacteria, fungi and algae [188]. Aqueous ions based on copper ions, complex copper species or copper-containing polymers have been proposed and used as effective antifungal agents [189]. In addition, Cu NPs, previously used as antifungal agents, have been found to be effective against various fungi species such as *Saccharomyces cerevisiae*, *Stachybotrys chartarum*, *Candida albicans*, *Rhizoctonia solani*, and *Candida tropicalis* [172,189-193].

There have been limited studies on the production of Cu NPs with biopolymers. In the literature, Cu NPs synthesis has been carried out especially by chemical reduction using hydrazine. When these studies were evaluated, it was observed that the low copper precursors concentrations changing from 1mM to 60 mM were used and copper reduction was carried out for long time periods (between 6h to 324h) or at elevated temperatures (between 80-120 °C) [171,173,176,180,184,194-201]. For this reason, in this study, it was aimed to produce Cu NPs in a shorter time by using a high copper salt solution. Therefore, microwave assisted reduction method was used to reduce the long reaction times. Soluble starch and sodium alginate were selected as biopolymers due to their availability of their hydroxyl groups to stabilize Cu NPs, biodegradability, biocompatibility, cheapness and renewability [176,184]. There have been studies based on the production of Cu NPs by microwave method using starch and sodium alginate [64,183,202,203], but in this study, Cu NPs synthesis was performed in the soluble starch and sodium alginate solutions by combining microwave radiation and chemical reduction by hydrazine at highly concentrated copper salt solution (0.32 M)

for the first time. It was also aimed to broaden the knowledge of antifungal properties of Cu NPs capped with polysaccharides (soluble starch and sodium alginate) against *Candida krusei* and *Candida albicans*.

4.2 Materials and Methods

4.2.1 Materials

CuSO₄·5H₂O (CAS-No: 7758-99-8), hydrazine hydrate (64-65%, reagent grade, CAS-No: 7803-57-8) and sodium alginate (C₆H₉NaO₇, alginic acid sodium salt from brown algae, CAS-No: 9005-38-3, W201502) were obtained from Sigma Aldrich. Soluble starch ((C₆H₁₀O₅)_n, CAS-No: 9005-84-9) ammonia solution (25%, Catalogue number: 105432), pepton (CAS-No: 91079-38-8), D(+) glucose monohydrate (CAS-No: 14431-43-7), agar-agar (CAS-No: 9002-18-0) were purchased from Merck. Other than these materials, deionized water was used in order to prepare solutions.

4.2.2 Synthesis of Cu NPs

The synthesis of Cu NPs was carried out on the basis of the work of Tantubay et al. [193]. Firstly, 0.5% (wt/v) soluble starch solution was prepared by stirring until the solution became clear. The sodium alginate solution was also obtained after stirring for 3 hours with deionized water at the same concentration. The pH value of these solutions were adjusted to 9 by addition of ammonia solution and 0.32 M CuSO₄·5H₂O solution was added into these solutions. Subsequently, 5 mL of hydrazine hydrate was added to the resulting mixtures and the obtained brown mixtures were then exposed to microwave irradiation for 2 minutes at 600 W in a domestic microwave oven. The obtained wine-red colored Cu nanoparticle solutions were centrifuged at 22000 rpm for 40 minutes. The Cu NPs separated from the solution were dispersed in deionized water and then centrifuged. This process was repeated two times, after which the washed Cu NPs were dried overnight in a vacuum oven at 40 °C at a pressure of 20 mbar.

4.2.3 Characterization of Cu NPs

Dynamic light scattering (DLS) analyzer (Nanoflex particle size analyzer) and scanning electron microscope (SEM, Jeol JSM-5410) were used to measure the nanoparticle size and determine the nanoparticles morphology. DLS measurements

were performed by dispersing the nanoparticles into deionized water. The average particle size was analyzed with the aid of an image visualization software (Image-J, National Institute of Health, USA) from about 100 random measurements of the nanoparticles. The success of the nanoparticle synthesis process was evaluated by X-ray diffraction (XRD, Bruker™ D8 Advance) with Cu-K α radiation. XRD patterns were acquired over a 2 θ range from 5° to 80° with a step size of 0.01°. Fourier transform infrared spectroscopy (FTIR, Spectrum 100, Perkin Elmer) with 4 cm⁻¹ resolution in transmittance mode in the mid-IR region (4000-650 cm⁻¹) was used to determine interactions between Cu NPs and polysaccharides (soluble starch and sodium alginate). KBr pellet method was used to perform FTIR measurements of Cu NPs. Cu NPs/KBr pellets were prepared at weight ratio of 1 wt%.

4.2.4 Antifungal activity of Cu NPs

The antifungal activities of Cu NPs against *Candida albicans* (ATCC 10231) and *Candida krusei* (KUEN 1001) were analyzed by broth microdilution method according to Tantubay et al [193]. Microorganisms were obtained by cultivating in the Sabouraud dextrose broth (SDB) medium and then concentrations were adjusted at about 10⁶ colony forming units (CFU) mL⁻¹. Aliquots of suspensions containing microorganisms in culture medium (150 μ L) were added to aqueous dispersions of 150 μ L of Cu NPs at concentrations changing from 4 mg mL⁻¹ to 7.8 μ g mL⁻¹ in 96 well plates, respectively. The inhibition of growth was determined by measuring the absorbance with a microplate reader (BioTek Synergy HT) at 540 nm for each concentration after an incubation at 37 ° C for 16 hours. Microbial growth inhibition was calculated using the following formula given in equation (4.1) :

$$Inhibition (\%) = 100 - \left(\frac{A_2}{A_1} \times 100 \right) \quad (4.1)$$

where A₁ and A₂ refer to the absorbance of fungal cells in the control and the absorbance of fungal cells in the test medium, respectively. As positive controls, aliquots of suspensions containing microorganisms in culture medium (150 μ L) were added to 150 μ L of SDB medium. Aqueous dispersions of 150 μ L of Cu NPs at concentrations changing from 4 mg mL⁻¹ to 7.8 μ g mL⁻¹ were mixed with 150 μ L of SDB medium to prepare negative controls.

Broths from the wells (included NPs and fungi) after the measurement of optical density were cultured onto Sabouraud dextrose nutrient agar (SDA) plates and incubated for 24 hours at 37 °C to determine minimum fungicidal concentration (MFC). MFC was the lowest fungicidal concentration of the tested NPs under defined condition.

4.3 Results and Discussion

At the very early stage of Cu NPs synthesis it was noticed that the color of the solutions changed to pink, deep red after microwave irradiation which was the first sign of Cu NPs formation [62]. When an aqueous Cu^{2+} solution reacted with hydrazine, the starting blue color of the CuSO_4 solution turned to pale yellow, yellowish black, light purple-brown, light brown and finally dark brown, and the color of these solutions changed to pink and dark red when irradiated by microwave irradiation [199]. SEM, XRD, FTIR, thermal analysis and antifungal tests of the obtained Cu NPs were performed to prove that the synthesized particles were Cu NPs and the properties of these nanoparticles were also determined.

4.3.1 Phase analysis

XRD analysis was performed to investigate the phase purity and crystallinity of both CuS NPs and CuA NPs. In the XRD pattern of CuA NPs given in Figure 4.1(a) sharp peaks were determined at 43.55° , 50.70° , and 74.41° , and in the XRD pattern of CuS NPs given in Figure 4.1(b) sharp peaks were determined at 44.27° , 51.39° , and 75.06° .

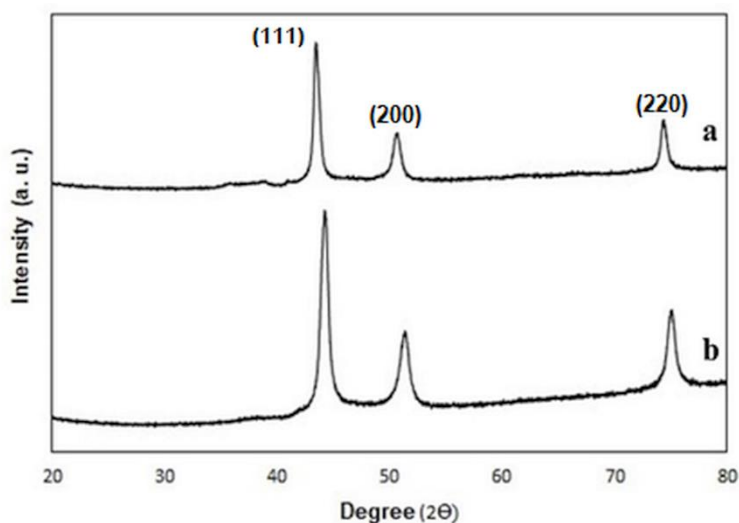


Figure 4.1 : XRD analysis of CuA NPs (a) and CuS NPs (b).

These peaks show that the synthesized structures are metallic copper with cubic (FCC) structure with Miller indices corresponding to (111), (200) and (220) crystal planes [176,177,181,199,201]. Also, other phases such as Cu₂O and CuO were not observed [177]. It shows that pure Cu NPs were obtained under microwave conditions.

4.3.2 Morphology of Cu NPs

SEM investigations reveal the pseudospherical morphology of CuA and CuS NPs (Figure 4.2 (a,d)) [64,169]. The mean particle size distributions of the Cu NPs were measured randomly using the Image-J software, and the obtained data were represented by the histograms given in Figure 4.2 (b,e). CuA NPs and CuS NPs have mean particle size diameters of 57 ± 10 nm with a size distribution changing from 32 nm to 85 and 67 ± 28 nm with a size distribution changing from 32 nm to 292 nm, respectively. Based on SEM images, it is seen that the size distribution of CuA NPs is more homogeneous than the size distribution of CuS NPs. In this case, it can be considered that the biopolymer type plays an important role as a polymeric capping agent and possibly as a size controller [169].

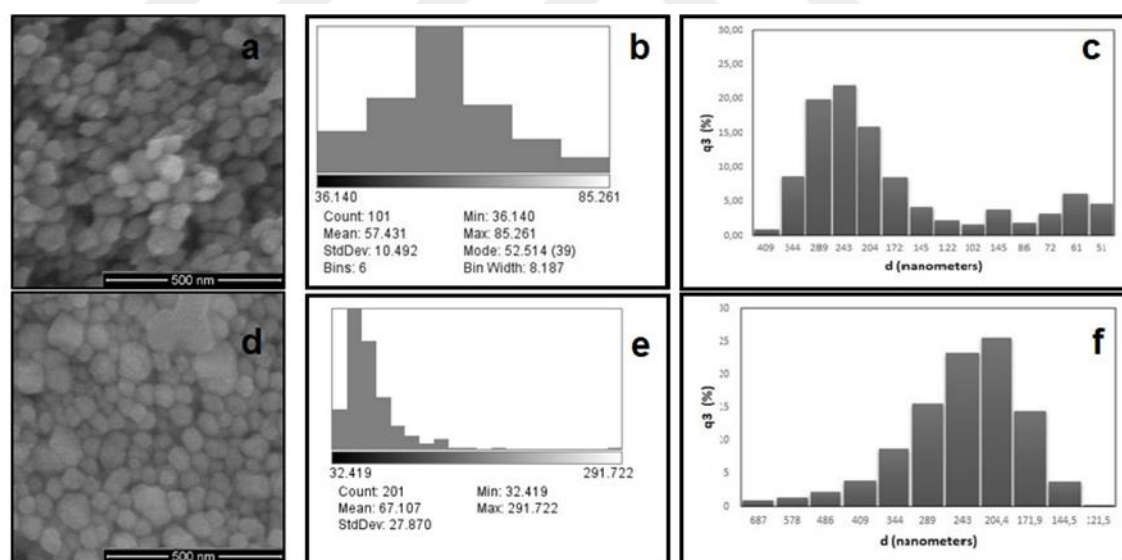


Figure 4.2 : SEM images of CuA NPs (a) and CuS NPs (d); Particle size distribution histograms of CuA NPs (b) and CuS NPs (e); DLS analysis of CuA NPs (c) and CuS NPs (f).

Starch, in aqueous solutions, has the right-hand helix structure, which may facilitate the complexation of a large number of hydroxyl groups with the molecular matrix of the metal ions. It consists of a linear component, amylose and amylopectin, a branched component. Branching results from 1,6 acetal bonds in amylopectin that are not present

in amylose. As a result of the bond angles in the alpha acetal bond, it is assumed that the amylose forms a spiral structure that helps stabilize [204]. In addition, starch acts as a dispersing agent for separating metal ions from one another and provides size control of the nanoparticles [205]. The amylose in starch has a wide size range changing from 3 μm to 200 μm [199]. Therefore, it is thought that the size distribution of CuS NPs obtained in this study depends on the size range of amylose content of starch. It was concluded that carboxylate and hydroxyl groups of sodium alginate selectively trap Cu NPs by providing inter and intramolecular interstices [202].

In addition, DLS analyzes of these nanoparticles were carried out and results with a large size distribution were obtained. This was because DLS showed the hydrodynamic diameter, while SEM showed the actual nanoparticle diameter [190]. As the hydrodynamic volume of NPs is measured in the DLS analysis, the polymer chain area surrounding the NPs is included [80,128]. When the DLS results of CuA NPs (Figure 4.2(c)) were examined, it was observed that there were two peaks in the size distribution. In the particle size distribution of CuA NPs, 82.9 % of the total volume had an average particle size of 263.8 nm and 17.1 % of the total volume had an average particle size of 67.5 nm. The occurrence of this distribution with particle size was based on the fact that the particles were capped with alginate. The distribution of CuS NPs had a mean particle size of 253.3 nm for the entire volume to form a single peak (Figure 4.2(f)). This result indicates that the starch capped on the particles. Furthermore, it was also supported by other studies in the literature that copper nanoparticles tend to accumulate and aggregate when dispersed in deionized water [206-208].

It has been reported in the literature that nanoparticles can more easily pass through cell membranes than bulk materials. Smaller nanoparticles have high toxic effects due to their high surface area to volume ratio [209]. Therefore, Auffan et al. stated that nanoparticles under 20-30 nm have thermodynamic instability and this critical dimensions should be considered for nanoparticles used in nanotoxicological studies [210]. Chen et al. reported that, nanoparticle-sized copper nanoparticles (23.5 nm) had acute toxicity comparing with micron-sized copper nanoparticles (17 μm) in mice in vivo [211]. Prabhu et al. investigated the effect of copper nanoparticles on dorsal root ganglion (DRG) in rats. In their study, they exposed these neurons to copper nanoparticles at increasing concentrations (10-100 μM) and sizes (40, 60 and 80 nm)

for 24 hours, and found that the smallest copper nanoparticles had toxic behaviour [206]. Alizadeh et al. investigated the in vitro wound healing promotion of copper nanoparticles at specific sizes (20 nm, 40 nm, 80 nm) and different concentrations. They found that copper nanoparticles (40 nm/10 mM) have proliferation effect in endothelial, keratinocyte and fibroblast cells, and also copper nanoparticles (80 nm/1 mM) support collagen expression [209]. When the dimensions of Cu NPs obtained in this study are examined, it is thought that these nanoparticles have a potential to be used in biotechnological applications at appropriate concentrations.

4.3.3 Thermal analysis

The differential thermogravimetric analysis (DTG) and differential thermal analysis (DTA) curves of sodium alginate, soluble starch, CuA NPs and CuS NPs given in Figure 4.3(a-d) were obtained under N₂ atmosphere. Based on these curves, the onset and ending temperatures of the weight losses occurring in the structures, the weight loss percentages in these temperature ranges and the temperatures with the maximum weight losses were summarized in Table 4.1. Initial weight losses occurring from room temperature (RT) to 100-130 °C range refer to the removal of the adsorbed water from the structure. The subsequent weight losses of the biopolymers ended at about 600 °C. At these intervals, the polymers are degraded and the mass losses at temperatures higher than 600 °C can be neglected. As the N₂ medium was studied, the Cu NPs remained intact without any oxidation [181]. The weight loss of CuS NPs between 130.7-408.6 °C was 6.87 % and the weight loss of CuA NPs between 124.3-467.9°C was 7.37%. These weight losses can be attributed to the biodegradation of the polymers which have the role as the biocapping materials.

The largest exothermic transition peak recorded in the DTA curve of the soluble starch starts at 215 °C and continues up to 300 °C with a maximum decomposition temperature at the DTG curve. This range can be interpreted as the temperature at which the amylose molecules are thermally decomposed [199]. When the DTA curve of CuS NPs was examined, an exothermic peak with a maximum value of 250 °C with the starting temperature of 211 °C was observed similar to the soluble starch. These results show that soluble starch and Cu NPs interact with each other. The sodium alginate biopolymer has also shown an exothermic peak starting at 184°C and reaching a maximum value of 240 °C. In the case of CuA NPs, two exothermic peaks were

observed at higher temperatures than 240 °C. As a result, it can be decided that the structure breaks down between 240-535 °C. This range is similar to the decomposition temperature range of sodium alginate [199].

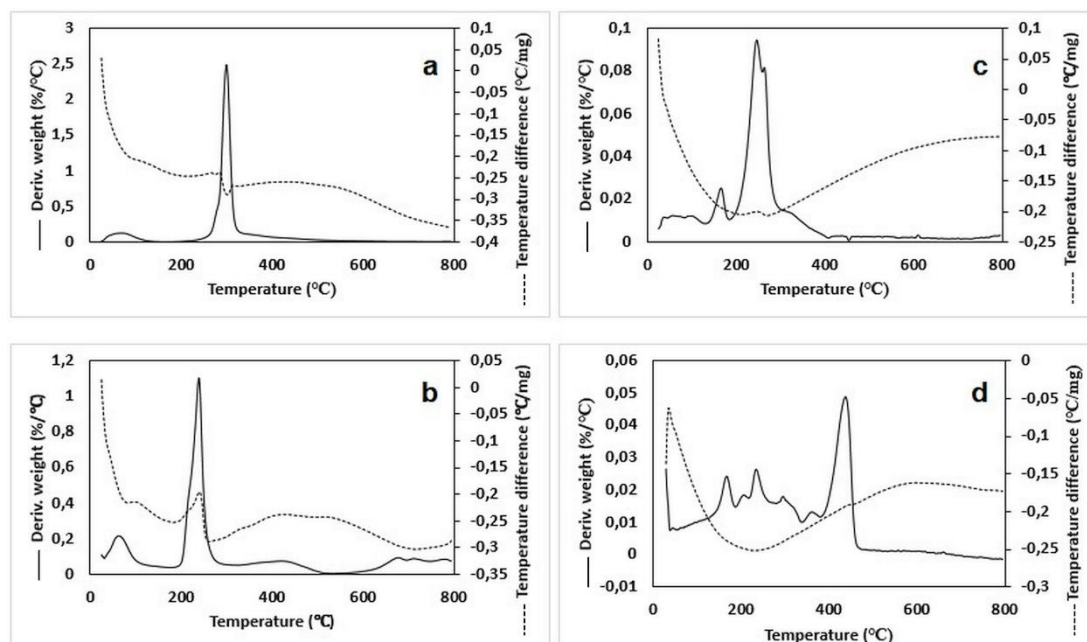


Figure 4.3 : DTG and DTA curves of soluble starch (a), sodium alginate (b), CuS NPs (c) and (d) CuA NPs under N₂ atmosphere.

Table 4.1 : Thermal analysis of soluble starch, CuS NPs, sodium alginate (NaAlg) and CuA NPs under N₂ atmosphere.

Sample	T _{d1} (°C)			Weight loss (%)	T _{d2} (°C)			Weight loss (%)
	T _{onset}	T _{max}	T _{end}		T _{onset}	T _{max}	T _{end}	
Starch	RT	69.2	133.3	8.2	215.2	299.5	613.3	74.1
CuS NPs	RT	56.4	130.7	1.2	130.7	165.5	408.6	6.9
						246.1		
						255.6		
NaAlg	RT	62.7	103.7	11.7	103.7	239.8	535.9	47.7
						419.6		
CuA NPs	RT	44.7	71.5	0.4	124.3	167.8	467.9	7.4
						204.9		
						234.5		
						293.8		
						361.4		
						438.3		

Thermogravimetric analysis (TGA) was carried out to investigate the thermal changes of CuS NPs and CuA NPs under air environment given in Figure 4.4. According to these graphs, the initial weight changes from room temperature to 135-150 °C range is due to the release of moisture in the structure [188]. The next thermal events starting

from the 140-150 °C range were caused by sodium alginate and soluble starch degradation. When the thermal analysis curves of CuS NPs and CuA NPs were examined, weight increases were observed after 379.5 °C and 366.9 °C, respectively due to the copper oxidation. Thermal changes occurring up to these values were given in Table 4.2.

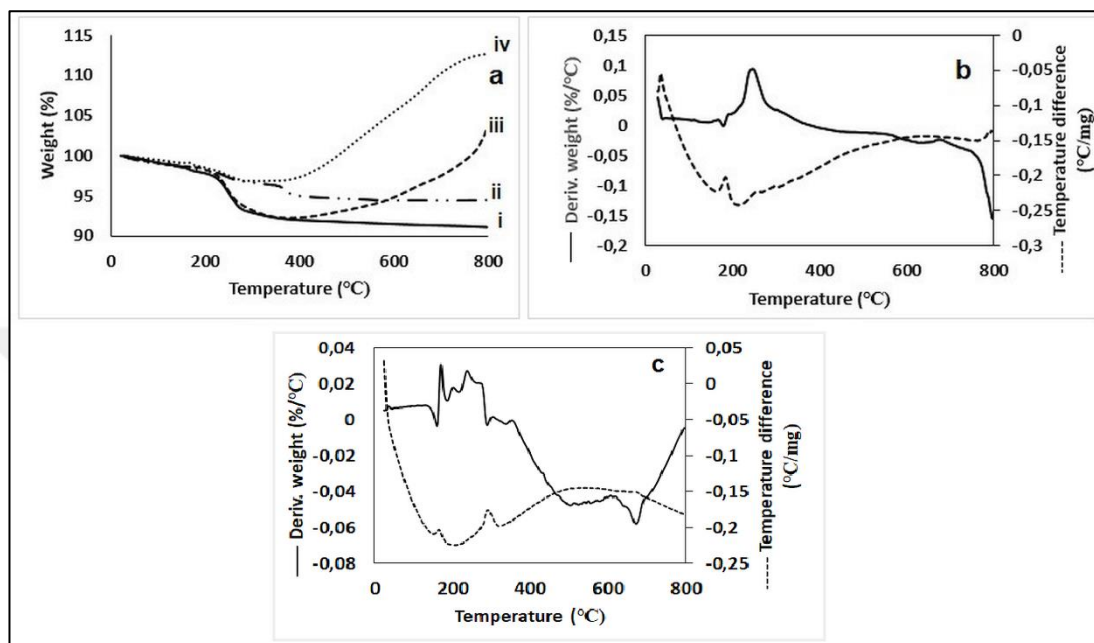


Figure 4.4 : (a) TGA of CuS NPs (i) and CuA NPs (ii) under N₂ atmosphere, TGA of CuS NPs (iii) and CuA NPs under air atmosphere; (b) DTG and DTA analysis of CuS NPs under air atmospheres; (c) DTG and DTA analysis of CuA NPs under air atmosphere.

Table 4.2 : Thermal analysis of soluble starch, CuS NPs, sodium alginate and CuA NPs under air atmosphere.

Sample	Td1 (°C)			Weight loss (%)	Td2 (°C)			Weight loss (%)
	Tonset	Tmax	Tend		Tonset	Tmax	Tend	
CuS NPs	RT	115.0	135.4	1.2	141.1	165.1	379.5	7.2
					190.1			
					243.8			
					303.1			
CuA NPs	RT	35.4	159.5	0.9	159.5	170.6	367.9	2.2
					201.2			
					242.6			
					302.1			
					351.2			
					362.3			

Weight losses between 140-150 °C range to 380-420 °C range of both Cu NPs are very fast and these losses can be interpreted to be related to biopolymer degradation because

they are similar to weight losses temperatures under nitrogen atmosphere [202]. The weight gain of CuS NPs to 800 °C is found as 10.95 %. And also, this value for CuA NPs was determined as 15.74 %. The DTG curve presented in Figure 4.4(b) shows that the approximate weight changes for CuS NPs occur at 165 °C, 190 °C, 246 °C and 303 °C, while the associated differential thermal analysis (DTA) curve shows a multi-step exotherm. These changes in sodium alginate are also seen in the DTG and DTA curves of CuA NPs at 165.39 °C, 205 °C, 243 °C, 290.92 °C, 338 °C and 362 °C. The resulting peaks may be associated with the combined effect of the decomposition of starch and sodium alginate, oxidation of Cu and the burning of any carbonaceous residue (starch and sodium alginate) [193]. Tantubay et al. have determined the exothermic peaks for Cu nanoparticles synthesized by carboxymethyl chitosan (CMC) at 158 °C, 205 °C, 243 °C and 304 °C. They proposed that the exothermic peak at 158 °C is related to the degradation of CMC and deconvenient thermal effects associated with the oxidation of Cu to Cu₂O [193]. In this study, the decomposition temperature of the biopolymers in the structure of CuS NPs and CuA NPs and the oxidation temperature of copper were determined as 165.1 °C and 170.6 °C, respectively. Tantubay et al. [193] compared the observed peaks at 205, 243 and 304 °C with three oxidation steps of Cu including surface oxidation of Cu₂O to CuO, oxidation of the cores of Cu NPs to Cu₂O and oxidation of Cu₂O cores to CuO. Considering these data; it can be interpreted that copper oxidation at CuS NPs takes place at temperatures of 190.1 °C, 243.8 °C and 303.1 °C. In addition to this, the copper oxidation temperatures of CuA NPs were found to be 201.2 °C, 242.6 °C, 302.1 °C, 351.2 °C and 362.3 °C.

4.3.4 FTIR analysis

FTIR spectra of soluble starch, sodium alginate, CuS NPs and CuA NPs were recorded to investigate the interaction of functional groups involved in the reduction of CuSO₄.5H₂O and subsequent stabilization of Cu NPs. Figures 4.5(a,b) show the FTIR spectra of the soluble starch and sodium alginate biopolymers. The main peaks of the soluble starch were observed at 3000-3600, 2926, 2163, 1979, 1681, 1584, 1487, 1409, 1364, 1325, 1294, 1236, 1148, 1104, 1077, 1013, 925, 832, 763, 691 and 660 cm⁻¹. The large absorption band between 3000-3600 cm⁻¹ and the small peaks at 2163 cm⁻¹, 1325 cm⁻¹, 1294 cm⁻¹ and 1980 cm⁻¹ are attributed to the vibration mode of O-H bonds and the combination of O-H stretching vibrations that represent the degree of hydrogen bonding in soluble starch, respectively [173,175,181,183,199,212,213]. Peaks at

2926 cm^{-1} , 1681 cm^{-1} , 1584 cm^{-1} , 1487 cm^{-1} , 1409 cm^{-1} , 1236 cm^{-1} refer to asymmetric C-H stretching of CH_2 , C-H bending vibration, asymmetric stretch of carboxylate, plane bending at CO-H symmetric carboxylate and acetyl group stretching [168,173,175,199]. The peaks at 1149 and 1013 cm^{-1} are associated with C-O stretching vibration of ether and alcohol groups [173,183]. The peaks at 925, 832, 763, 691 and 660 cm^{-1} correspond to the pyranose ring [173]. Figure 4.5(c) depicts the FTIR spectrum of starch capped Cu NPs showing characteristic frequencies at 2915, 1647, 1566, 1519, 1411, 1102, and 692 cm^{-1} [175]. Small peaks similar to starch-like peaks mean that both hydroxyl and carboxyl groups were involved in the synthesis and stabilization of Cu NPs.

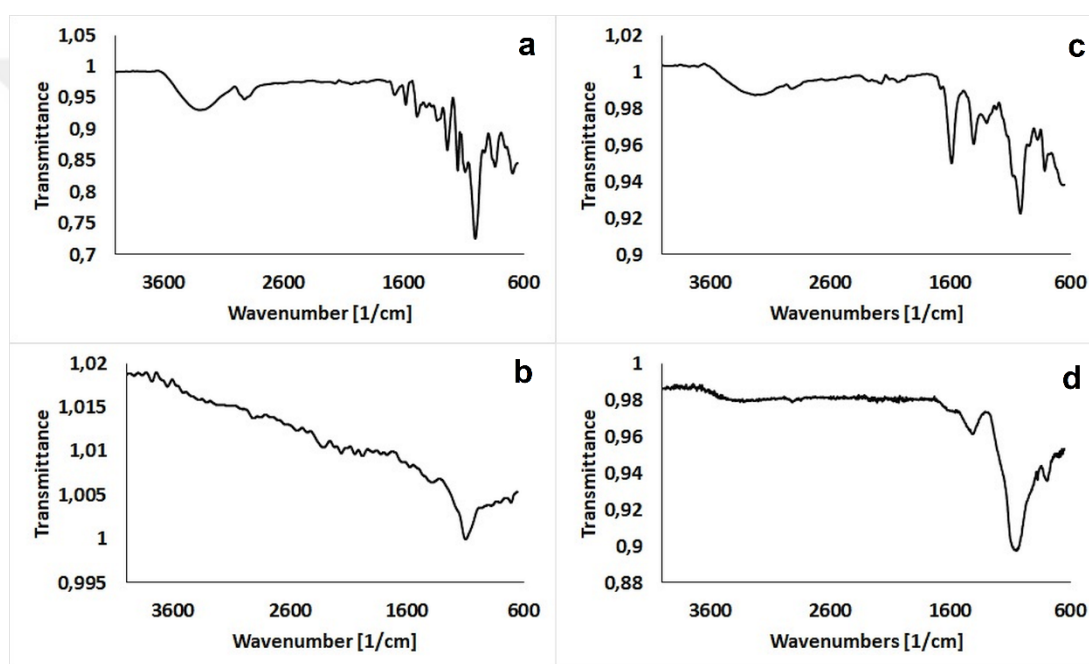


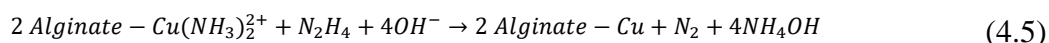
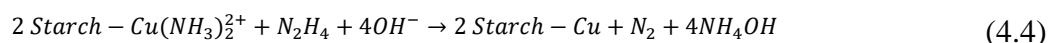
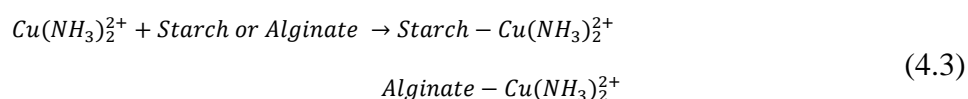
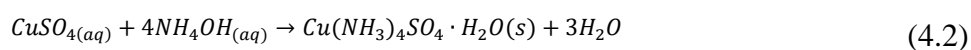
Figure 4.5 : FTIR spectra of soluble starch (a), CuS NPs (b); sodium alginate (c) and CuA NPs (d).

The major peaks in the FTIR spectrum of the sodium alginate were observed at 3298, 2162, 1980, 1682, 1588, 1407, 1300, 1218, 1011, 949, 878, 816 and 664 cm^{-1} . The absorption band at 3298 cm^{-1} and the small peaks at 2162 cm^{-1} and 1980 cm^{-1} are attributed to the vibration mode of O-H bonds and the combination of O-H stretching vibrations, respectively [173,175,181,183,199,213]. The peaks at 1682 cm^{-1} , 1588 cm^{-1} , 1407 cm^{-1} , 1218 cm^{-1} correspond to C-H bending vibration, carboxylate asymmetric stretching (COO^-), symmetric carboxylate and acetyl group stretching [168,175,199]. The peak at 1013 cm^{-1} is associated with C-O stretching vibration of ether groups [183]. The peaks at 949, 878, 816 and 664 cm^{-1} correspond to the out-of plane

deformation of the glycosidic bond on the pyranose rings coupled with other deformation vibrations (C–H of the β -mannuronic acid residues and C–H of the α -glucuronic acid residues) [173,202]. Figure 4.5(d) shows the FTIR spectrum of CuA NPs indicating characteristic frequencies at 1418, 1051, 875, and 801 cm^{-1} . Small peaks similar to the sodium alginate mean that hydroxyl groups were involved in the synthesis and capping of Cu NPs.

Interactions in carboxyl and hydroxyl groups were observed in the FTIR spectrum which mean that these structures were effective in the synthesis of Cu nanoparticles. The reason for this was the formation of a chemical bond between the oxygen atoms of these groups and the Cu^{2+} and Cu atoms. The positively charged Cu^{2+} surfaces form ion-pairs with O-H groups. Thus, the reduction of the Cu^{2+} to Cu^0 occurs in the amylose chain in soluble starch and the soluble starch serves a role as a capping agent that controls the morphology of the nanomaterials instead of being stabilizer [199]. The local bridging interaction process between Cu^0 and the oxygen of the $-\text{C}=\text{O}$ group has influence upon the vibrations of the O-C-O⁻ group, the C-OH deformation, -O-C-O⁻ symmetrical stretching and C-C stretching of mannuronic and glucuronic acid depending on the strength and spatial range of the $-\text{C}-\text{O}-\text{Cu}$ interaction due to the high electron density of copper [202].

Based on the findings from XRD, FTIR and literature studies, chemical reduction reactions of $\text{CuSO}_4 \cdot 5\text{H}_2\text{O}$ salt using hydrazine, soluble starch or sodium alginate and ammonia solution can be anticipated as the following equations (4.2-4.5) [193,198,199,201]:



In the light of these information, hydrazine instantly reduces copper ions. Thus, the possibility of occurrence of impurities such as oxide phase Cu_2O and $\text{Cu}(\text{OH})_2$ are eliminated. In addition, during the reduction process the sustained release of N_2

provides an inert atmosphere, so that no external inert gas source is required during synthesis [193,198]. Because of the high concentration of Cu^{2+} solution, this procedure has good reproducibility which can be used for large-scale synthesis of Cu NPs [193].

4.3.5 Stability of Cu nanoparticles

Cu nanoparticles were kept in open air conditions for 6 weeks in order to determine their stability at the ambient conditions, and the changes in their structures were determined by the XRD analysis given in Figure 4.6. Extra peaks at 36.63° and 61.68° were detected for CuS NPs which correspond to the (111) and (220) crystal planes of crystalline Cu_2O . In CuA NPs, similar to CuS NPs the (110), (111), (220) crystal planes of copper oxide were found at 29.91° , 36.65° and 61.72° [214-216]. However, when these two XRD graphs were compared, it was seen that the Cu_2O peaks of CuA NPs were more pronounced, indicating that CuA NPs were more sensitive to oxidation.

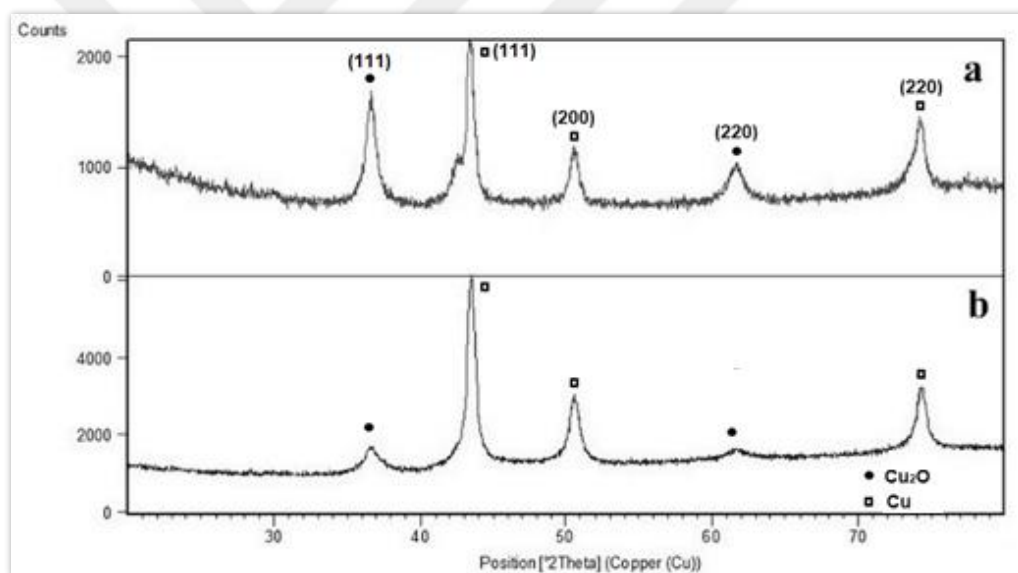


Figure 4.6 : XRD of CuA NPs (a) and CuS NPs (b) kept under open air environment for 6 weeks.

It was also important to note that no Cu_2O was observed in the XRD pattern of the copper nanoparticles obtained after the synthesis (Figure 4.6). Similar results were also obtained by Murtaza et al. They determined the presence of copper oxide (Cu_2O) in the copper nanoparticles synthesized with polyvinylpyrrolidone (PVP) by using XRD patterns to verify the oxidation stability. According to the XRD pattern they obtained, they found that copper nanoparticles synthesized without PVP have Cu_2O in the structure even one hour after the synthesis. This showed that uncapped copper

nanoparticles were very sensitive to oxidation. The XRD pattern of the PVP capped copper nanoparticles after one week showed that PVP prevented oxidation [217].

4.3.6 Antifungal activity of CuA NPs and CuS NPs

Cu NPs have a great activity for the removal of bacterial and fungal contaminants, which may be useful for surface disinfection, inside paints, biomedical and pharmaceutical purposes. Primary action modes associated with the antibacterial effect of Cu NPs are unclear [218]. Most likely the dynamic structure of the fungal cell wall allows the passage of NPs. Subsequently, Cu NPs (as reported for AgNPs) probably result in disruption of the plasma membrane integrity and inhibition of the fungal budding process [190].

CuS NPs and CuA NPs were further tested for antifungal activities against *C. albicans* (ATCC 10231) and *C. krusei* (KUEN 1001), which are the major causative agents of fungal diseases in humans [185]. According to our literature survey, there was no report on the antifungal activity of Cu NPs against to *C. krusei*. The results were presented in Figure 4.7. Both of the Cu NPs tested against these fungi showed inhibitory activity after 16 hours and the inhibitory activity was increased with the increase in the concentration of Cu NPs.

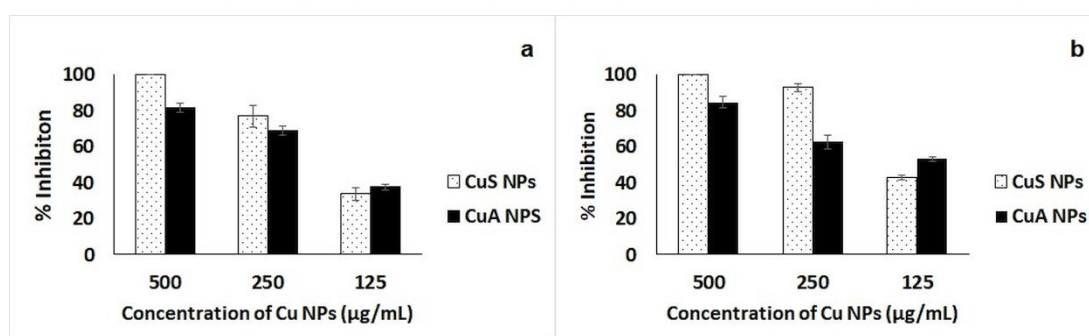


Figure 4.7 : Percentage inhibition of *C.albicans* (a) and *C.krusei* (b) by Cu NPs.

After the microdilution test, samples taken from the post-test medium were spread on SDA and they incubated for 24 hours at 37 °C to determine whether there was any growth of the microorganisms (Figure 4.8). The minimum fungicidal concentrations (MFC) were determined to compare the efficiency of the synthesized Cu NPs. Similarly to the microdilution test, MFC values for *C. krusei* were determined as 1 mg CuA NPs/mL and 0.5 mg CuS NPs /mL. The MFC values for *C. albicans* were found to be as 1 mg/mL for CuA NPs and 0.5 mg/mL for CuS NPs. Based on the MFC values,

it was concluded that CuS NPs had more effectivity against both microorganisms than CuA NPs.

The antifungal properties of Cu NPs against *C. albicans* have been reported in various studies and the minimum inhibiton concentration (MIC) values and MFC values differ from each other. For example; Rasool et al. was found the MFC of the Cu NPs synthesized by plant extract (*Gelidium* sp.) as 5 mg/mL [219] . Beltrán-Partida et al. synthesized ascorbic acid capped copper nanoparticles and they found their MFC value as 500 µg/mL [220]. Kruk et al. determined the MIC of Cu NPs synthesized by sodium dodecyl sulfate (SDS) as 3.75 µg/mL and Bogdanović et al. found that the MFC value of copper/polyaniline nanocomposite was 1 µg/mL [221,222]. Although there are few studies based on the efficacy of Cu nanoparticles against *C. albicans*, it seems that the stabilizing agent and particle size of Cu NPs are the important factors on the antifungal activity against *C. albicans* [219].

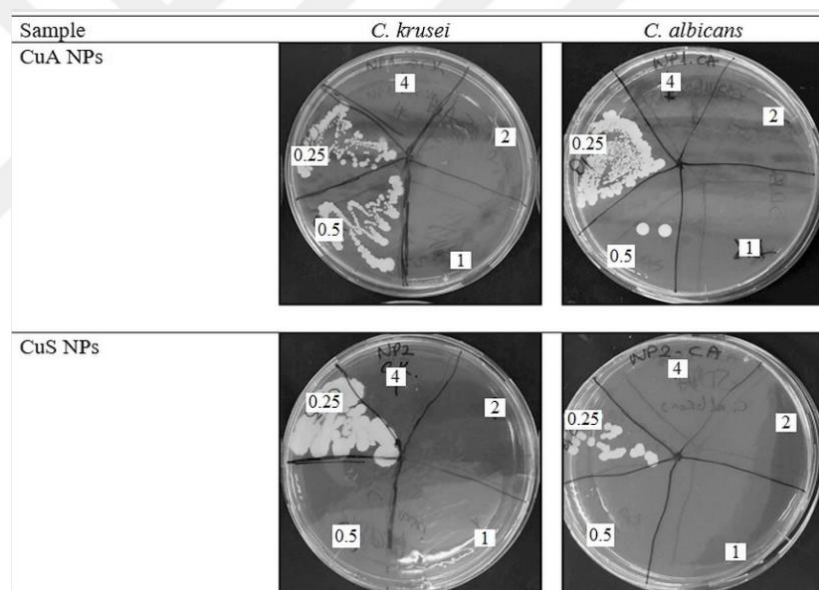


Figure 4.8 : Growth of *C. krusei* and *C. albicans* on Agar medium loaded with CuA NPs and CuS NPs microdilution test samples at different concentrations (4, 2, 1, 0.5, 0.25 mg/mL).

4.4 Conclusions

In this study, the effects of polymeric capping agents (soluble starch and sodium alginate) on Cu NPs synthesized by microwave assisted chemical reduction method were compared. Nanoparticle size distributions of these particles were determined using SEM and DLS analyzes. In the DLS analysis of CuA NPs, the size distribution showed two peaks. In contrast, CuS NPs had a more uniform distribution. Thermal

analysis results showed that Cu NPs were capped with soluble starch and sodium alginate. In FTIR analysis, the determination of soluble starch and sodium alginate peaks in the FTIR spectra of the nanoparticles pointed the capping of the polymers on the nanoparticles which confirmed the results of the thermal analysis. The behavior of the nanoparticles at the ambient conditions determined by XRD indicated the relatively high intensity of the Cu_2O peaks at CuA NPs and the stability of the CuS NPs. The antifungal tests against *C. krusei* and *C. albicans* showed that CuS NPs had more inhibitory activity than CuA NPs. Since no published information regarding the antifungal activity of Cu NPs against *C. krusei* has been found in the literature, this study was the first report introducing the antifungal activity of biopolymer capped Cu NPs against this fungus. Furthermore, this study demonstrated the potential of starch capped Cu NPs in various antifungal applications including biotechnological and food packaging applications.

5. OPTIMIZATION OF THE FABRICATION OF POLYCAPROLACTONE NANOFIBER MATS DOPED WITH BIOACTIVE GLASS AND COPPER NANOPARTICLES FOR TISSUE ENGINEERING APPLICATIONS⁴

5.1 Introduction

Electrospinning method has introduced in different novel applications of polymeric fibers (in the range of micro or nanosized diameters) over distinctive areas [106]. In the production of nanofibers prepared by electrospinning method, there are several process requests which are the solution-properties (viscosity, concentration, polymer type, polymer molecular weight, surface tension, conductivity, solvent type, solvent dielectric constant, solvent volatility), environmental factors (temperature, humidity, atmosphere, pressure, etc) and the processing conditions (applied voltage, electric field strength, electrostatic field shape, flow rate, distance between the tip of syringe and collector, needle diameter) to fine tune the shape-size harmony of the electrospun fibers that ultimately determine their bio-physicochemical properties [12,100-102,104-106,108,110,111,113,115,116,121]. In this way, it is desirable to have quantitative connection between these parameters and fiber properties in order to operate, optimize, and control whole process. That is to say, it is feasible to estimate fiber properties by variation in one or more parameters [112].

It would be very time consuming to examine each factor independently on the morphology of fibers and the optimization of the parameters with the desired diameter with low working costs [102,121]. For this reason, statistical experimental design techniques can be utilized to assess the impacts of factors and the optimization of experimental parameters [121]. Unlike conventional approaches to formulate optimization, when a variable evaluated at one time, statistical optimization uses fewer but more meaningful experiments and provides an optimum formulation in a correct manner by an efficient approach [108,115]. With this basis, response surface

⁴ This chapter is based on the article “Akturk, A., Erol Taygun, M., Goller, G., Küçükbayrak, S. (2020). Optimization of the Fabrication of Polycaprolactone Nanofiber Mats Doped with Bioactive Glass and Copper Nanoparticles for Tissue Engineering Applications (*Submitted*).

methodology (RSM) is frequently seen as a reasonable aid to plan experiments. It is a well-suited choice in creating numerical models, measuring the impact factors and the search for ideal combinations of factors [106]. In this context, a polynomial model is utilized to examine the main and interactive impacts of various factors on response and to get an optimal response. RSM has been effectively utilized for diverse processes like injection, molding, fiber spinning and electrospinning for optimization and expectation of response factors [108] .

Electrospinning has drawn attention in tissue engineering applications because of electrospun fiber mat having a web like nature, high porosity, very small pore size and large specific surface area by providing a nanoscale biomimetic structure of natural extracellular matrix (ECM) [223,224]. Many polymers such as polycaprolactone (PCL), polyurethane (PU), polylactic acid (PLA), poly(glycolic acid) (PLGA), poly-DL-lactide (PDLLA), gelatin, cellulose acetate, chitosan, polyethersulphone have been commonly electrospun to manufacture nanofibrous scaffolds for particular end uses[12,18,101,105,108,110,113,114,126,129,143,145,147,161,224-228]. Especially, due to their in vitro hydroxycarbonate apatite formation ability inorganic particles like bioactive glass (45S5 bioglass, 58S bioglass, borate glass, strontium borosilicate glass, strontium-substituted bioactive glass), hydroxyapatite, tricalcium phosphate were used as fillers to form nanocomposites for bone tissue engineering applications [19,104,114,123,129,145,147,225,227-234]. Also, copper takes a key part in improving bone formation and healing and it functions as a cofactor in metabolic processes including bone, articular tissues and immune system processes. Noteworthy visible cell copper distributions have been found in human endothelial cells, when they have undergone angiogenesis showing this ion as a significant angiogenic agent [235].

In this study, 45S5 bioglass due to its ability to form hydroxyapatite and copper nanoparticles because of their angiogenic property were used as the fillers of PCL polymer matrix for the fabrication of the nanocomposite scaffold. RSM coupled Box-Behnken response design (BBD) and cytotoxicity studies with L929 fibroblast cells were performed to find out the polymer solution properties by changing polymer concentration, bioglass and copper nanoparticle percentage in the polymer matrix to be able to obtain a suitable nanocomposite for bone tissue engineering applications.

5.2 Materials and Methods

Polycaprolactone (PCL, average Mn 80000), silicon dioxide (SiO₂), and Copper(II) sulfate pentahydrate, were obtained from Sigma Aldrich. N,N-dimethylformamide (DMF), dichloromethan (DCM), soluble starch di-sodium hydrogen phosphate anhydrous (Na₂HPO₄), calcium carbonate (CaCO₃) and sodium carbonate (Na₂CO₃), and ammonia solution were all purchased from Merck. Murine fibroblast cells (L-929) (ATCC), Dulbecco's Modified Eagle Medium (DMEM) with 5% fetal bovine serum and penicilline-streptomycine (FBS, Gibco Life Sciences Cat#10270-106), and WST-1 assay (Roche Cat#11644807001) were used to measure cell proliferation in nanofiber mats.

5.2.1 Preparation of copper nanoparticles

0.32 M copper sulfate pentahydrate solution was added into 0.5 wt % starch solution to prepare copper nanoparticles. Thereafter, the pH of the solution was set to 9 by using ammonia solution. Hydrazine monohydrate was added to this solution. This solution was reacted in a domestic microwave oven (Bosch, HMT882H model) that operated at 600 W and a frequency of 2450 MHz, for 2 min to obtain copper nanoparticle solution. The obtained nanoparticle solution was centrifuged at 22000 rpm for 40 min and the supernatant was discarded, the precipitate was washed by using deionized water and a further centrifugation was performed. The obtained precipitate was dried under vacuum at 40 °C [236].

5.2.2 Preparation of bioactive glass particles

Bioactive glass particles were produced utilizing melt-quenching method. In order to produce bioactive glass, the precursor chemicals were first placed in a platinum crucible at appropriate amounts for 45S5 bioactive glass. After that, they were melted at 1250 °C for 2h and quickly quenched into deionized water to form frits. The prepared frits were then grounded and placed in the platinum crucible to repeat the melting and quenching steps to get a homogeneous and an amorphous structure. At last, the prepared bioactive frits were ground under 45 µm to obtain bioactive glass particles (BG).

5.2.3 Preparation of PCL/Cu NP/BG solutions and electrospinning process

First Cu NPs was added to DMF/DCM solution (20/80(v/v)) and the solution was stirred for an hour. After that, BG was added to this mixture and stirred for an hour. At last PCL was dissolved in this mixture and stirred at room temperature for 2 h in order to obtain homogeneous solution. The polymer blends were prepared according to the ratios based on Box Behnken Design experiments.

The as-prepared solutions were transferred to a plastic syringe equipped with a flat stainless steel needle, which was connected to a high-voltage supply. Voltage applied to the needle tip was 20 kV. The flow rate was set as 1.25 ml/h by a syringe pump. Nonwoven electrospun fibers were deposited onto an aluminum foil wrapped around the grounded collector placed at a distance of 17 cm perpendicular to the needle tip. Electrospinning procedure was performed at 26°C with a relative humidity of 60%.

5.2.4 Design of electrospinning experiments by Box Behnken Design (BBD)

Three factor three level BBD was performed to determine the relationship between three independent variables of PCL concentration in DCM/DMF solution (X_1) (10-15 % wt/v), Cu NPs ratio to PCL (X_2) (2.5-7.5 % wt/wt) and BG ratio to PCL (X_3) (10-20 % wt/wt) on the average diameter of PCL/BG/Cu NPs composite nanofibers. The variables were encoded in three different intervals (-1, 0, +1) and the average fiber diameter was chosen as the response. The analysis of variance (ANOVA) of experimental data were examined using Minitab 17.0 statistical software. F and p-values were examined to determine the importance of each term in the model. P-values < 0.05 mean that the parameter has a significant effect on the nanofiber diameter. The performed experiments and their results can be seen from Table 5.1.

The BBD response surface model of electrospinning experiments refers to the diameter of the PCL/Cu NPs/BG composite nanofibers as a function of the above variables. The polynomial model for the nanofibers' diameter according to the electrospinning variables was expressed in the equation 5.1 as follows:

$$Y = C_0 + \sum_{i=1}^3 C_i x_i^2 + \sum_{i=1}^3 C_{ii} x_i^2 + \sum_{i=1}^3 \sum_{j=1}^3 C_{ij} x_i x_j \quad (5.1)$$

where Y is the predicted response and C_0 , C_i , C_{ii} , and C_{ij} are the constant coefficients of the model. X_i , X_{ii} , and X_{ij} are the linear, quadratic and interactive factors of the uncoded variables, individually. The determination coefficient (R^2) was used to evaluate the accuracy of the full quadratic equation.

Table 5.1 : The BBD design experiments and results.

Experiment Number	PCL concentration (wt/v %)		Cu NPs ratio (wt/wt)%		BG ratio (wt/wt)%		MFD ¹ (nm)	CFD ² (nm)
	Actual values	Coded values	Actual values	Coded values	Actual values	Coded values		
1	10	-1	2.5	-1	15	0	480	509
2	15	1	2.5	-1	15	0	779	881
3	10	-1	7.5	1	15	0	565	496
4	15	1	7.5	1	15	0	1406	1410
5	10	-1	5	0	10	-1	617	669
6	15	1	5	0	10	-1	1371	1312
7	10	-1	5	0	20	1	653	667
8	15	1	5	0	20	1	1330	1310
9	12.5	0	2.5	-1	10	-1	840	861
10	12.5	0	7.5	1	10	-1	1134	1120
11	12.5	0	2.5	-1	20	1	972	859
12	12.5	0	7.5	1	20	1	999	1118
13	12.5	0	5	0	15	0	820	824
14	12.5	0	5	0	15	0	848	824
15	12.5	0	5	0	15	0	870	824

¹MFD: Measured fiber diameter, ²CFD: Calculated fiber diameter by the model

5.2.5 Morphological characterization of nanofiber mats

Morphology of the nanofibrous scaffolds were determined by scanning electron microscope (SEM, Jeol JSM-5410). Before the observation, surfaces of scaffolds were sputter coated (SC7620 sputter coater, Quorum Technologies Ltd, United Kingdom) with platinum for 120 s. For each experiment, the average fiber diameter and its standard deviation were analyzed with the help of an image visualization software (Image-J, National Institute of Health, USA) from about 50 measurements of the random fibers.

5.2.6 Cell behavior of fibroblast cells on nanofibrous mats

A water soluble tetrazolium (WST-1) assay was used to measure cell response of L-929 fibroblasts grown in well plates with nanofiber mats. This protocol is based on the reduction of the WST-1 by viable cells to generate a colored formazan dye by glycolic production of NADPH. The formazan dye was quantified by measuring the absorbance at 440 nm. For the WST-1 assay, samples were cut as discs with diameter of 15 mm

and these discs were split in two equal parts. Afterwards, the samples were sterilized under UV irradiation for 40 min (each side for 20 min).

L-929 fibroblast cells were maintained in DMEM at 37 °C in a humidified atmosphere with 5% CO₂ incubator (ESCO, Singapore). The cell culture medium was removed from the flask containing the L-929 cells and the cell surface was washed with 5 mL phosphate buffered saline (PBS) to subculture the cells for the WST-1 assay. Then, trypsin was added to the flask to release the cells from the flask surface and a new culture medium was added to resuspend the cells.

The sterilized samples were placed into individual wells of a 96-well plate and incubated in 200 µL of cell culture medium for an hour. Then 1×10^4 L-929 murine fibroblast were added and incubated for 24 h, 48 h and 72 h. After the incubation periods ended, nanofiber samples were taken and transferred to another 96-well plate. 200 µL of WST solution diluted with cell culture medium at volumetric ratio of 1/10 in each well, it was allowed to react with viable cells for 2 h. Absorption of formazan dye was then read by a microplate reader (BioTek Elisa ELx800). For this assay, the absorption directly correlates to the viable cell number. Culture medium with WST-1 reagent and no cells with nanofiber mats served as blanks so the color of the medium did not affect the absorbance readings.

5.2.7 Stability of nanofiber mats in simulated body fluid

Nanofiber mats were immersed in freshly prepared simulated body fluid (SBF) at a ratio of 20 mg/mL and incubated at various time points (1, 7, 14 and 28 days) at a controlled temperature of 37 °C. At each time point, the samples were removed from the SBF, rinsed three times slowly with deionized water to remove saline, and dried at 37 °C until constant weights, and then SEM images were taken. The copper ions concentrations released from the nanofiber mats to the SBF solution were measured by inductively coupled plasma-mass spectrometer (ICP-OES, Perkin Elmer, Optima 2100 DV model). The mineralization ability of the nanofiber mat in the SBF was determined by X-ray diffraction (XRD, Bruker™ D8 Advance) with Cu-K α radiation. XRD patterns were acquired over a 2θ range from 10° to 80° with a step size of 0.01°.

5.3 Results and Discussion

5.3.1 Statistical results

15 experiments based on response surface methodology coupled with Box Behnken Design were determined for regression analysis of three parameters at three levels. (Table 5.1). The Box Behnken design requires less experimentation with three factors at three levels with maximum efficiency within the experimental design methods, [31]. Analysis of variance (ANOVA) was used to evaluate the variables' effects and their interactions, as given in Table 5.2.

Table 5.2 : ANOVA results for the experimental response at different levels.

Source	DF	Seq SS	Adj MS	F	P
Regression	9	1157277	128586	20.77	0.002
Linear	3	959649	319883	51.67	0.000
X ₁	1	826255	826255	133.47	0.000
X ₂	1	133386	133386	21.55	0.006
X ₃	1	8	8	0.00	0.973
Square	3	104882	34961	5.65	0.046
X ₁ ²	1	945	945	0.15	0.712
X ₂ ²	1	1869	1869	0.30	0.606
X ₃ ²	1	97800	97800	15.80	0.011
Interaction	3	92746	30915	4.99	0.058
X ₁ X ₂	1	73441	73441	11.86	0.018
X ₁ X ₃	1	1482	1482	0.24	0.645
X ₂ X ₃	1	17822	17822	2.88	0.151
Residual error	5	30952	6190		
Lack-of-fit	3	29696	9899	15.76	0.060
Pure error	2	1256	628		
Total	14	1188229			
				Model evaluation	
				R ²	0.9740
				R ² adjusted	0.9271
				R ² predicted	0.5978

After the elimination of insignificant terms ($p > 0.05$) from the quadratic terms and interaction terms, the obtained ANOVA results of the response at different levels were given in Table 5.3 and the equation of linear and quadratic terms in uncoded units for the three solution properties to approximate the PCL nanofiber fiber diameter was found as follows (equation 5.2):

$$Y = 1802 + 20.2x_1 - 219.3x_2 - 198.1x_3 + 6.60x_3^2 + 21.68x_1x_2 \quad (5.2)$$

The R² value of the new model appears to be low. R² always increases with the number of terms in the model. It is known that the decrease in R² occurs when there are few terms in the model [112]. However, R² adjusted and R² predicted were improved,

having values of 95.63% and 93.21%, respectively. The high values of these correlation coefficients prove the goodness-of-fit measure of the model [31]. After removal of the insignificant terms from the model, it appears there is a reasonable agreement (within 0.2 of each other) between the R^2 adjusted value and the R^2 predicted value [237,238].

Table 5.3 : ANOVA results after elimination of insignificant terms for the experimental response at different levels.

Source	DF	Seq SS	Adj MS	F	P
Regression	5	1134642	226928	39.41	0.000
Linear	3	959649	319883	55.55	0.000
X ₁	1	826255	826255	143.49	0.000
X ₂	1	133386	133386	23.16	0.001
X ₃	1	8	8	0.00	0.971
Square	1	101552	101552	17.64	0.002
X ₃ ²	1	101552	101552	17.64	0.002
2-way interaction		73441	73441	12.75	0.006
X ₁ X ₂	1	73441	73441	12.75	0.006
Residual error	9	51823	5758		
Lack-of-fit	7	51805	7401	792.93	0.001
Pure error	2	19	9		
Total	14	1186466			
				Model evaluation	
				R ²	0.9563
				R ² adjusted	0.9321
				R ² predicted	0.8185

5.3.2 Validation of experimental and predicted model data

Predicted versus actual values plot and normal probability of residuals plot were evaluated to determine the goodness of the proposed model. Figure 5.1(a) shows the actual and predicted values of the fiber diameters by a diagonal line with a fairly uniform random distribution of all the points having a linear correlation coefficient of $R^2=0.9553$ [238].

The slight deviation seen between the experimental and model values means that the actual values of fiber diameter are in close agreement with predicted values of fiber diameter [112,238]. It is possible with a normal probability graph, to determine whether there is a normal probability distribution of residuals following a straight line or not [238]. Figure 5.1(b) reveals that fiber diameters are in a narrow range on a straight normal probability line suggesting a normal distribution of residuals and that there are small minor points deviating from the normal line [13,238]. Thus, the satisfactory normal distribution in the deviation of the model estimation from the

actual data confirms the validity of the quadratic regression model and proves the independence and normality of the residuals [238].

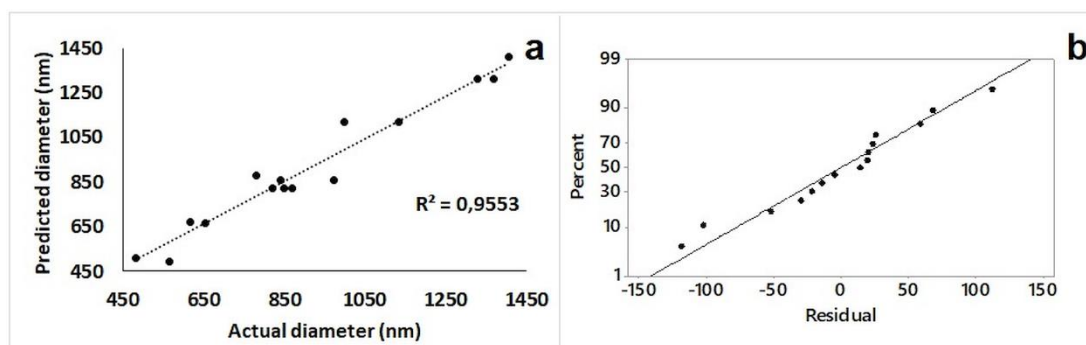


Figure 5.1 : (a) Plot of model predicted fiber diameter against experimental fiber diameter, and (b) normal probability plot.

In addition, the estimation capability of the model was tested with a validation test by setting the PCL concentration, the Cu NPs ratio and BG ratio as 15 %wt/v, 2.5 %wt/wt, and 10 %wt/wt and the fiber diameter was measured as 1032 ± 338 nm. By using these parameters, the fiber diameter was calculated with model equation as 1047 nm, which is consistent with the model.

5.3.3 Effect of parameters on the response

A sensitive control over the diameter of the nanofibers is highly effective on the final properties of nanofiber mats for administration in biomedical areas, because nanofibers with lower diameters have higher surface area for cell attachment and proliferation and for drug loading [17].

ANOVA tables and perturbation plots were examined to determine affecting factors on the fiber diameter. The sharpness of curvature in the perturbation graphs indicates that the response to the factor is highly sensitive, while the semi-flat curves indicate that the response to the factor is less sensitive. The effect of all independent variables on the average diameter of the nanofibers was obtained using coded levels at the intermediate levels of the independent variables [238].

Based on the ANOVA results (Table 5.2) and perturbation plots (Figure 5.2), PCL concentration appears to have a linear effect and it has the most significant effect on the fiber diameter. With increasing the PCL concentration in electrospinning solution the fiber diameter rises sharply, which based on the balance between surface tension and viscosity (Figure 5.2(a)) [112].

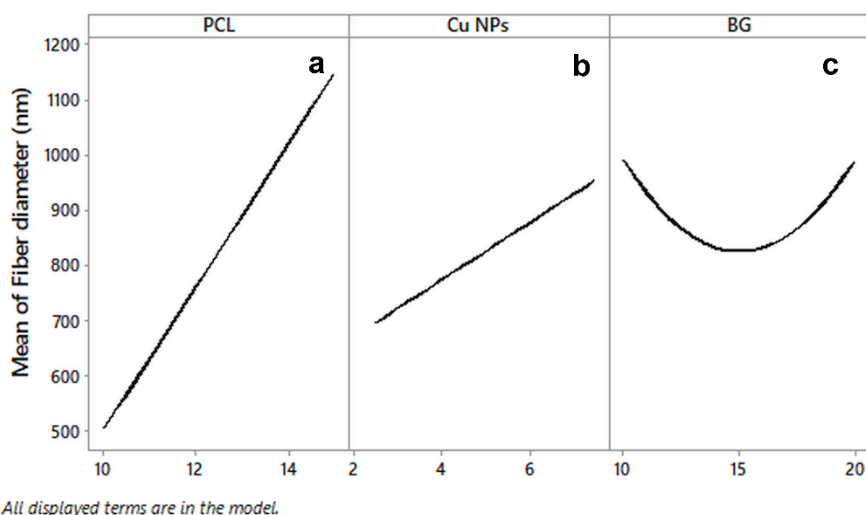


Figure 5.2 : Perturbation plot for fabrication of PCL/BG/ Cu NPs nanofibers as a function of PCL concentration (a), Cu NPs ratio (b), and BG ratio (c).

Higher concentrations in polymer solutions result in higher viscosity which cause to more pronounced chain entanglement. As a result, larger viscous elastic forces that resist axial stretching inhibit the set of bending instability during whipping. The reduced jet path leads to produce fibers with larger diameter [13,31,33,239]. In addition; larger viscous elastic force exceeds surface tension and leads to formation of less bead and droplet-free structure [13]. As shown in Figure 5.2(b), increasing the Cu NPs ratio has a positive effect to produce nanofiber mats with larger diameter. BG contribution has a quadratic effect on the nanofiber diameter as seen in the perturbation plot of the BG ratio (Figure 5.2(c)). BG incorporation increases the conductivity of the polymer solutions and leads to a reduction in fiber diameters' size [139,140]. When the perturbation plot of BG ratio was examined, this effect was seen up to 15% BG ratio. At the BG ratio higher than 15%, the effect of viscosity increase becomes dominant and leads to an increase in fiber diameter.

It was also found that PCL had an interaction with Cu NPs shown in the perturbation and interaction plots. Nanofiber diameters increased with incorporation of Cu NPs especially at higher PCL concentrations. However, the fiber diameter sizes found to be relatively similar at the minimum polymer concentration (10% wt/v) across all Cu NPs ratios. The mutual interaction between PCL and BG was found to be insignificant as seen from the interaction plots (Figure 5.3). The quadratic effect seen in the BG/PCL mutual interaction plot is the main square effect of BG on the nanofiber diameter.

The same situation was observed when the graphs of mutual interactions between Cu NPs and BG were examined.

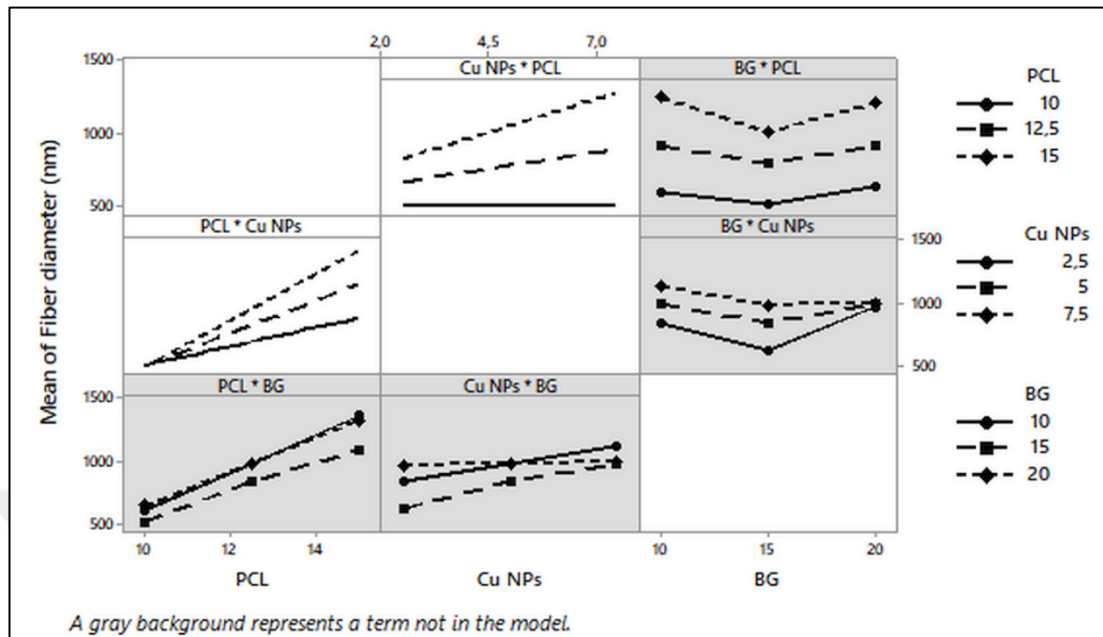


Figure 5.3 : Interaction plots between the formulation variables of PCL concentration, Cu NPs ratio, BG ratio.

5.3.4 Response surface analysis

The whole relations between the response variable and the independent variables within an operating range can be better evaluated with the contour and response surface plots obtained by the model predicted empirical equation [13]. The two-dimensional (2D) contour plots and three dimensional (3D) surface plots can be developed by combining equal response points [112]. Thus, with the resultant response surface, a useful visualization can be performed to define the desired response and operating parameters [13]. These plots describe the mutual interactions of independent variables, while the other variables are held constant [13,238].

Contour and surface plots which were based on the binary relationships were developed to determine optimum conditions for obtaining the minimum fiber diameter (Figure 5.4 (a-c)). The contour plots show constant responses between 500 nm and 1400 nm and the darkest areas indicate the highest fiber diameter. Hereby, the variables were kept constant at PCL concentration = 12.5% wt / vol, Cu NPs ratio = 5% wt / wt, BG ratio: 12.5% wt /wt for all contours and surface areas.

The surface plot and contour plot given in Figure 5.4(a) show the interactive effect of PCL concentration and Cu NPs ratio on the nanofiber diameter. The plots indicate that

a continuous increase in both PCL concentration and Cu NPs ratio advocate the increase in fiber diameter value. It can be seen that increase of Cu NPs was more effective at high concentrations for a fixed BG ratio of 15% wt/wt. Nanofiber diameter values at 15% PCL concentration varied between 880 nm and 1410 nm with Cu NPs increase, while nanofiber diameter values at 10% PCL concentration showed constant values at around 500 nm.

When the contour and surface diagrams of PCL concentration and BG interaction plotted for fixed 5% Cu NPs, a circular shape indicating insignificant interaction can be seen (Figure 5.4(b)) [240]. Quadratic and linear effects of BG and PCL can be observed in these interaction plots. The interaction of Cu NPs and BG for a constant concentration of 12.5 PCL % wt/v is also ineffective, as evidenced in the contour and surface plots for Cu NPs and BG. In this case, quadratic and linear effects of BG and Cu NPs can be observed in the interaction plot.

The diameter of the structural natural ECM proteins has a fiber size range of about 50-500 nm [6]. For this reason, the optimal values to obtain nanofiber diameter similar with ECM was selected. The fibers at diameters less than 600 nm can be estimated by using contour and surface plots as follows: 10% PCL concentration, 15% BG ratio, and all of the Cu NPs ratios. When the model equation was solved, it was determined that the minimum nanofiber size was 496 nm and this size was obtained with 10% PCL concentration, 7.5% Cu NPs ratio and 15% BG ratio.

5.3.5 Cytocompatibility study

Cytotoxicity studies were carried out by fabricating nanofiber membranes with the formulation levels obtained from the optimization study (10% PCL concentration, 15% BG glass ratio and Cu NPs ratio ranging from 2.5 to 7.5%). WST-1 tests were performed with neat PCL nanofiber mat (PCL), PCL nanofiber mat with 15% BG ratio (PCL-BG), PCL nanofiber with 15% BG ratio and 2.5% Cu NPs ratio (PCL-BG-2.5 Cu), PCL nanofiber with 15% BG ratio and 5% Cu NPs ratio (PCL-BG-5 Cu), and PCL nanofiber with 15% BG ratio and 7.5% Cu NPs ratio (PCL-BG-7.5 Cu). As a result of this test, it was determined that BG glass incorporation had an effect on cell proliferation and cytotoxicity was detected in all membranes with Cu NPs added.

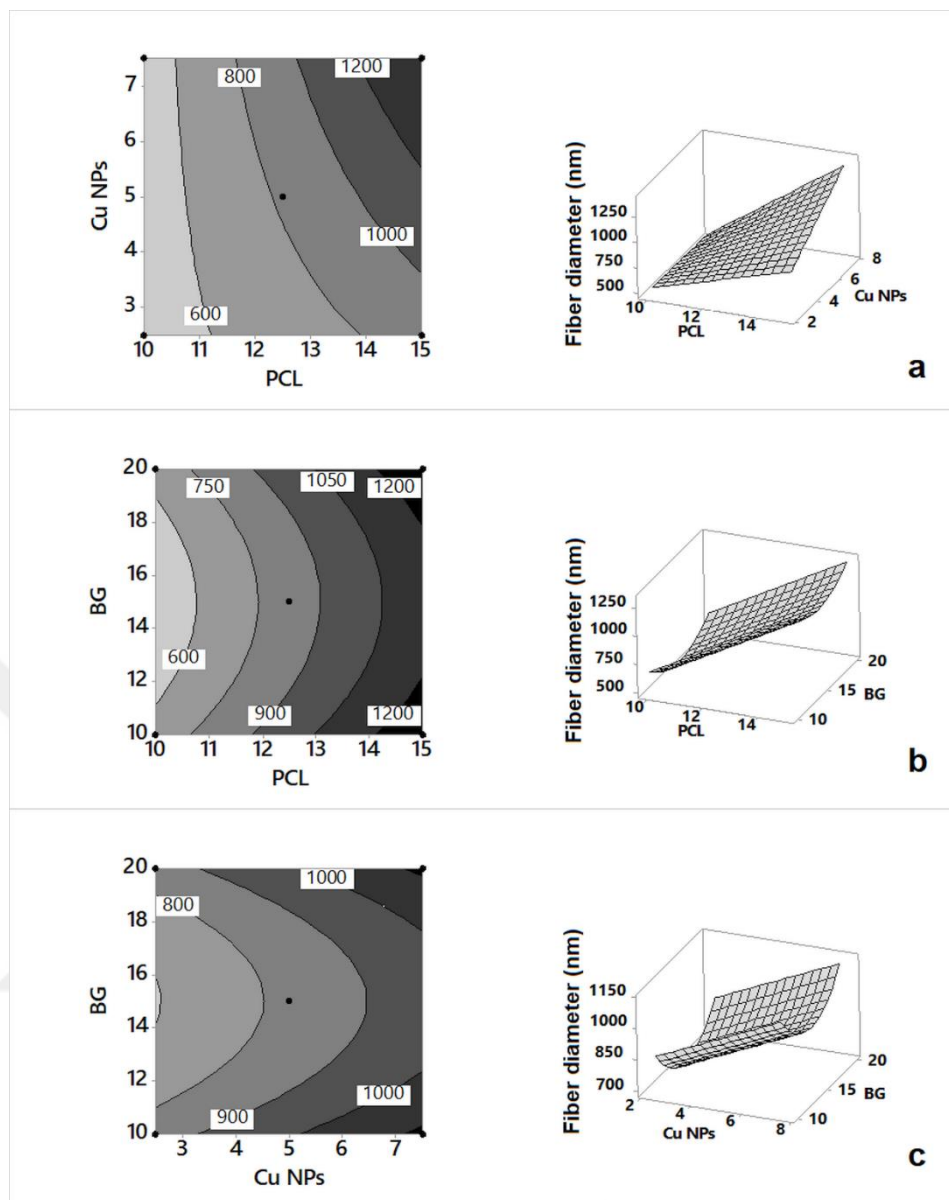


Figure 5.4 : Contour and surface plots of the response variable (fiber diameter, nm) for different experimental factors(two factor at a time): a) PCL concentration and Cu NPs ratio, b) Cu NPs ratio and BG ratio.

Therefore, the study was continued at the Cu NPs levels other than mathematical modeling. PCL nanofiber with 15% BG ratio and 0.25% Cu NPs ratio (PCL-BG-0.25 Cu), PCL nanofiber with 15% BG ratio and 0.5% Cu NPs ratio (PCL-BG-0.5 Cu), PCL nanofiber with 15% BG ratio and 0.75% Cu NPs ratio (PCL-BG-0.75 Cu) showed also toxic effect on the L929 fibroblast cells.

Further experiments were performed with PCL-BG-0.025 Cu, PCL-BG-0.05 Cu, PCL-BG-0.075 Cu membranes with copper ratios of 0.025%, 0.05% and 0.075% Cu NPs. Among these membranes, only the PCL-BG-0.025 Cu membrane was found to to have no cytotoxic properties (Figure 5.5).

Since nanofiber production was carried out at the Cu NPs levels outside from the optimization study, SEM images of PCL, PCL-BG, PCL-BG-0.025 Cu, PCL-BG-0.05 Cu, PCL-BG-0.075 membranes were taken to visualize their morphological structure (Figure 5.6). The fiber sizes of the PCL, PCL-BG, PCL-BG-0.025 Cu, PCL-BG-0.05 Cu, PCL-BG-0.075 membranes were measured as 481 ± 142 nm, 389 ± 72 nm, 474 ± 152 nm, 414 ± 88 nm, and 503 ± 278 nm, respectively. As can be seen from these results, PCL nanofiber diameter decreased with BG incorporation, and nanofiber diameters increased with the incorporation of Cu NPs.

SEM images of the membranes incubated for 72 h were taken to support the results in the WST-1 assay (Figure 5.6). In particular, fibroblast cells were detected on the PCL, PCL-BG and PCL-BG-0.025 Cu nanofiber mats. Furthermore, no cells were detected on the PCL-BG-0.05 Cu and PCL-BG-0.075 Cu nanofiber mat.

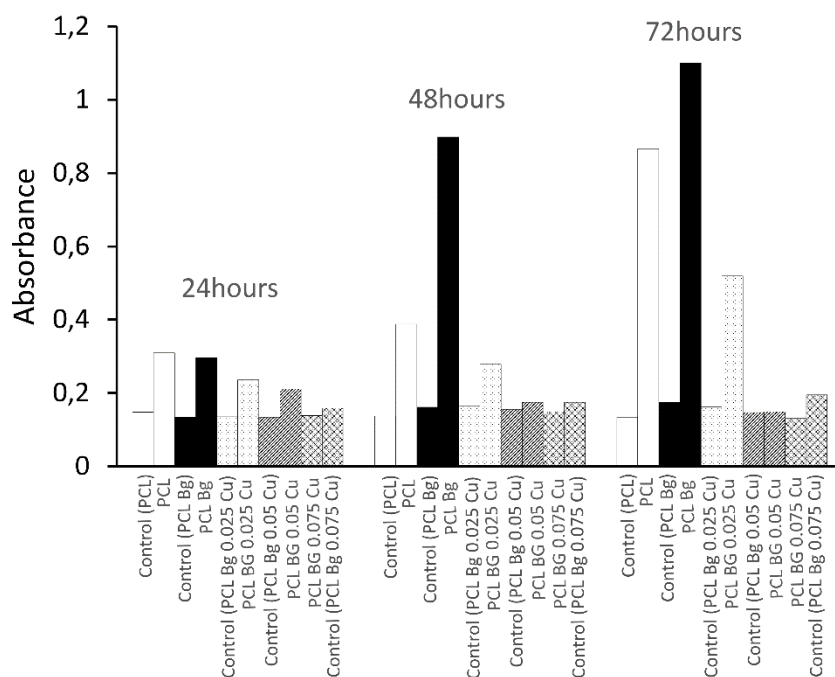


Figure 5.5 : The WST-1 assay absorbance graph of the PCL nanofiber mats containing BG and Cu NPs after 24, 48 and 72 hours.

5.3.6 In vitro mineralization study and Cu ions release assessment

It is known that copper element is necessary for skeletal metabolism and deficiency of copper element causes bone abnormalities. In addition, it is determined that osteoporotic patients have significant Cu element deficiency than healthy people. It is also observed that there is also copper deficiency in patients having Menke's syndrome and occipital horn syndromes. Cu stimulates vascular endothelial growth factor

(VEGF) expression and accelerates wound healing. It is also effective on the hypoxia-inducible factor (HIF)-1 α expression and VEGF in human bone marrow stromal cells [241].

However, the biological activity of the Cu element in cells is dose dependent [242]. In various studies, the osteogenic and angiogenic activity of Cu ion were investigated with different experimental conditions and different values have been obtained [241-246]. For this reason, in this study, Cu ions release amounts were obtained with the same experimental conditions as Lu et al. [241] and it was tried to determine whether the PCL-BG-0.025 Cu nanofiber membrane obtained had osteogenic potential by comparing with the values they obtained (35-40 $\mu\text{mol/L}$). Figure 5.7(a) depicts the release of Cu ion from the PCL-BG-0.025 Cu nanofiber membrane in simulated body fluid (SBF) and the maximum Cu ions release was found as 2.5 ppm (39 $\mu\text{mol/L}$), which shows the Cu ions delivery capacity and osteogenic potential of the obtained nanofiber mat.

The common point of bioactive materials is their apatite like layer formation ability when they interact with physiological fluids mimicking human plasma [246]. The in-vitro bioactivity of the PCL-BG-0.025 Cu nanofiber membrane was assessed by analyzing the SEM images of the nanofiber membranes which were immersed in SBF for 1, 7, 14 and 28 days (Figure 5.8). The XRD analysis of the sample kept in SBF for 28 days was performed to determine the precipitates' structure seen in the SEM images (Figure 5.7(b)). The diffraction peaks appeared at $2\Theta = 25.86$, $2\Theta = 31.94$ and $2\Theta = 43.66$ indicate the lattice planes that define hydroxyapatite [242,245]. According to the SEM images, the formation of hydroxyapatite appears to occur within 7 days. However, the decrease of the Cu ions release value after 12 hours suggests that Cu might coprecipitate in hydroxyapatite [245]. Based on this result, it can be interpreted that hydroxyapatite formation begins after 12 hours. Furthermore, it was observed that the fiber structure was preserved within 28 days.

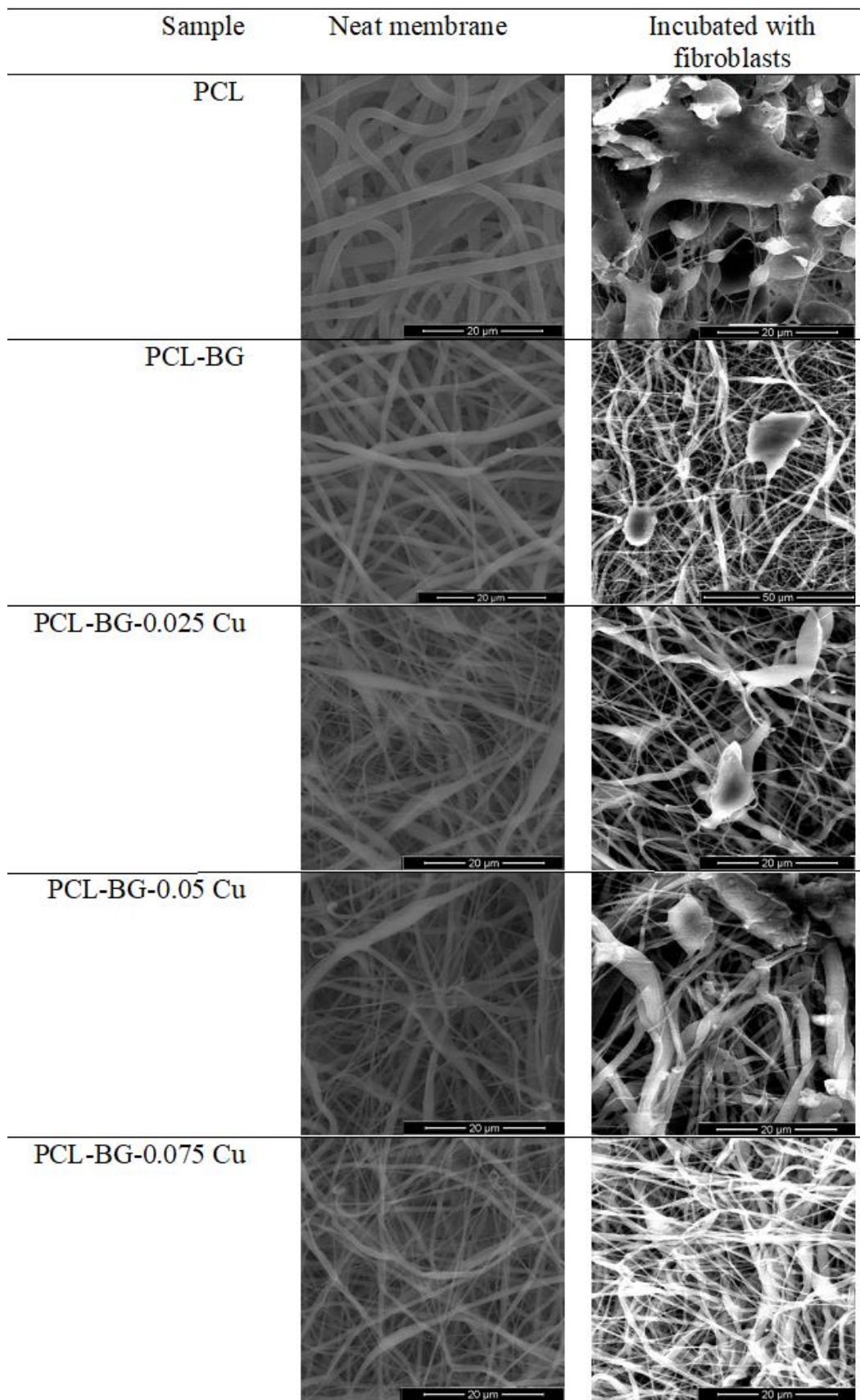


Figure 5.6 : The SEM images of the PCL nanofiber mats containing BG and Cu NPs after WST-1 for 72 hours.

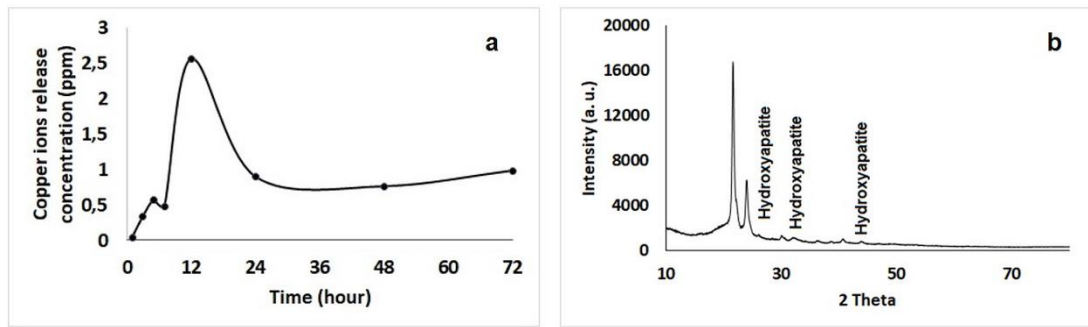


Figure 5.7 : (a) Copper ions release of the PCL-BG-0.025Cu nanofiber mat in SBF for different time intervals and (b) XRD graph of the PCL-BG-0.025Cu nanofiber mat immersed in SBF for 28 days.

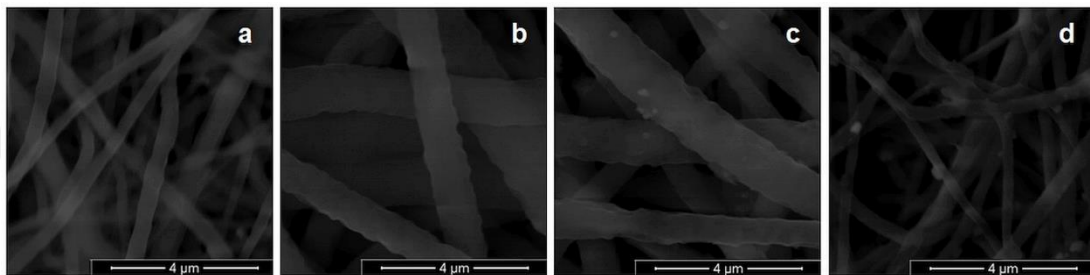


Figure 5.8 : SEM images of the PCL/BG/0.025 Cu NPs nanofiber mat immersed in SBF for 1 day (a), 7 days (b), 14 days (c), and 28 days.

5.4 Conclusions

In this study, polycaprolactone nanofiber scaffolds doped with bioactive glass (BG) and copper nanoparticles (Cu NPs) were fabricated by electrospinning technique. Three electrospinning process factors, including PCL concentration, BG ratio, and Cu NPs ratio were evaluated at three levels in the fabrication of electrospun nanofibers via Box-Behnken design. As a result of these evaluations, it was observed that fiber diameter increased linearly with PCL concentration increase. BG contribution had a quadratic effect on the fiber diameter and Cu NPs incorporation increased the fiber diameter. The surface and contour plots were estimated to find the formulation parameters to obtain nanofibers with minimum fiber sizes. It was determined that nano fibers at about 500 nm can be fabricated with 10% PCL concentration, 15% BG ratio and all of the Cu NPs ratios. After the results of cytotoxicity studies with L929 fibroblast cells, BG contribution was found to have a positive effect on fibroblast cell proliferation. The PCL-BG-0.025 Cu nanofiber was found to be non-toxic for the fibroblast cells. The SBF studies indicated the osteogenic potential of the obtained nanofiber mat. Overall results showed that this nanofiber formulation was suitable for both bone tissue engineering and wound dressing applications.



6. CONCLUSIONS

Tissue engineering is a new and developing area which aims tissue or organ regeneration. The activities related with the cells are in nano dimensions. Therefore, nanocomposites are important to create templates (scaffolds) for cells to live in, but a problem that can be faced by implantation of this template is microbial attachment. As antibacterial agent, the metal nanoparticles are very efficient to prevent microbial attachment. Therefore, nowadays, metal–polymer nanocomposites are the subject of increased interest due to their potential to combine the features of polymers with inorganic materials. In this regard, in the first article given in this study, silver nanoparticles were synthesized with 19 ± 6 nm diameter using soluble starch as reducing and capping agent by microwave synthesis method. The obtained silver nanoparticles (S-Ag NPs) solution was used as the antibacterial agent for PVA nanofibers in different weight ratios. It was determined that nanofibers containing up to 10% (w/w) S-Ag NP can be produced in porous, interconnected and fibrous structure morphology. Two different methods (heat treatment and glutaraldehyde immersion) were used as the cross-linking processes to enhance the stability of the PVA/S-Ag NPs nanofiber mats in physiological environments. Silver ions release was found to be more efficient when using glutaraldehyde immersion as the crosslinking method. Antibacterial tests against *E. coli* and *S. aureus* were performed with PVA/S-Ag NPs nanofiber mats crosslinked with glutaraldehyde, and it was found that these nanofiber mats were more antibacterial effectivity against *S. aureus* than *E. coli*. Ag ions release values were compared with the literature. The results showed that nanofiber mats containing 5%, 7.5% and 10% (w/w) silver nanoparticles have the potential for wound dressing applications. The silver nanoparticles obtained in this study can be used as additives with different polymer structures other than PVA. For further studies, the synthetic PVA membrane structures obtained in this study can be modified by adding biologically active natural polymer additives such as chitosan, hyaluronic acid, gelatin, alginate, etc.

Specifically, the combination of a natural polymer (biopolymer) and metal nanoparticles is highly appealing because of the individual antibacterial activity of the

metal nanoparticle components, and the possibility to generate a biodegradable and biocompatible composite. The bioactivity of composites can be achieved by using bioactive inorganics such as hydroxyapatite and bioactive glasses. Within this respective, the second article in this study aimed to combine metal-polymer-bioactive glass to fabricate a new nanocomposite material. Experimental studies were aimed to be carried out by a combination of electrospinning technique and response surface methodology based on Box-Behnken design technique to fabricate nano-scaled composite materials from gelatin, bioactive glass, and silver nanoparticles. For this purpose, Ag nanoparticles fabricated in the first article in this study were used and bioactive glass (45S5®) particles were produced by melt derived process. Then, solutions containing mixtures of gelatin, Ag nanoparticles and bioactive glass particles were prepared to obtain electrospun nanofibers at the relevant conditions (applied voltage, tip-to-collector distance and flow rate). Hence, the optimal conditions to produce metal nanoparticles and nanocomposite scaffolds were investigated. Characterization studies showed that the nanocomposite scaffold optimized in this article had a potential to be used in cartilage and bone repair applications where mechanical strength is not required. In applications requiring high mechanical strength, it is recommended to produce multiple layers with mechanically resistant biopolymers or to use mechanically competent 3D printed networks.

In comparison with Ag nanoparticles, Cu nanoparticles have been less studied because of its ease of oxidation, although they show a significant promise as antibactericidal agent. Cu and Cu compounds are effective against lots of microorganisms such as *Vibrio cholerae*, *Shigella*, *Escherichia coli*, *Salmonella*, fungi, viruses, etc. In the third article in this study, the effects of polymeric capping agents (soluble starch and sodium alginate) on the Cu NPs synthesized by microwave assisted chemical reduction method were compared. SEM results showed that sodium alginate capped Cu NPs (CuA NPs) and soluble starch capped Cu NPs (CuS NPs) had particle size of 57 ± 10 nm and 67 ± 28 , respectively. DLS analysis, thermogravimetric analysis and FTIR measurements were performed to prove the capping of the Cu NPs with these biopolymers. XRD analysis carried out after the synthesis of the nanoparticles showed that the synthesized Cu NPs had metallic copper structure with no impurity. In addition to that, the behavior of the Cu nanoparticles at the ambient conditions was also determined by XRD indicating the relatively high intensity of the Cu_2O peaks at CuA NPs and the stability of the CuS

NPs against oxidation. The antifungal tests against *C. krusei* and *C. albicans* showed that CuS NPs had more inhibitory activity than CuA NPs. As a result, CuS NPs were thought to have a potential in various antifungal applications, including biotechnological and food packaging applications. As further studies, cytotoxic properties of these copper nanoparticles could be determined.

In the fourth article in this study, poly(ϵ -caprolactone) nanocomposite mats doped with 45S5® bioactive glass particles and copper nanoparticles were fabricated by using the electrospinning technique and response surface methodology based on Box-Behnken design technique. The copper nanoparticles capped with soluble starch (CuS NPs) obtained in the third article were used in this study. The solution parameters (PCL concentration, bioactive glass content, Cu nanoparticles content) were optimized to determine targeted fiber diameter. In addition, the most suitable CuS NPs content was determined by the biocompatibility tests. It was determined that nano fibers at 500 nm which were non-toxic to fibroblast cells could be fabricated with 10% PCL concentration, 15 wt/wt% bioactive glass ratio to PCL and 0.025 wt/wt% Cu NPs ratio to PCL. The nanofiber composite obtained in this study was thought to have a potential for wound dressing applications due to its non-toxicity to fibroblast cells and bone tissue engineering applications because of its ability to form hydroxyapatite in the simulated body fluid. It is recommended to carry out mechanical tests, angiogenic studies or animal tests of this scaffold for future studies.



REFERENCES

- [1] **Armentano, I., Dottori, M., Fortunati, E., Mattioli, S., and Kenny, J.** (2010). Biodegradable polymer matrix nanocomposites for tissue engineering: a review, *Polymer Degradation and Stability*, 95(11), 2126-2146.
- [2] **Bhattacharai, D., Aguilar, L., Park, C., and Kim, C.** (2018). A review on properties of natural and synthetic based electrospun fibrous materials for bone tissue engineering, *Membranes*, 8(3), 62.
- [3] **Jun, I., Han, H.-S., Edwards, J. R., and Jeon, H.** (2018). Electrospun fibrous scaffolds for tissue engineering: Viewpoints on architecture and fabrication, *International Journal of Molecular Sciences*, 19(3), 745.
- [4] **Jenkins, T. L., and Little, D.** (2019). Synthetic scaffolds for musculoskeletal tissue engineering: cellular responses to fiber parameters, *NPJ Regenerative Medicine*, 4(1), 1-14.
- [5] **Nemati, S., Kim, S. J., Shin, Y. M., and Shin, H.** (2019). Current progress in application of polymeric nanofibers to tissue engineering, *Nano Convergence*, 6(1), 1-16.
- [6] **Khorshidi, S., Solouk, A., Mirzadeh, H., Mazinani, S., Lagaron, J. M., Sharifi, S., and Ramakrishna, S.** (2016). A review of key challenges of electrospun scaffolds for tissue-engineering applications, *Journal of Tissue Engineering and Regenerative Medicine*, 10(9), 715-738.
- [7] **Chocholata, P., Kulda, V., and Babuska, V.** (2019). Fabrication of Scaffolds for Bone-Tissue Regeneration, *Materials*, 12(4), 568.
- [8] **Tan, G. Z., and Zhou, Y.** (2019). Electrospinning of biomimetic fibrous scaffolds for tissue engineering: a review, *International Journal of Polymeric Materials and Polymeric Biomaterials*, 1-14.
- [9] **McCullen, S. D., Ramaswamy, S., Clarke, L. I., and Gorga, R. E.** (2009). Nanofibrous composites for tissue engineering applications, *Wiley Interdisciplinary Reviews: Nanomedicine and Nanobiotechnology*, 1(4), 369-390.
- [10] **Ma, P. X.** (2008). Biomimetic materials for tissue engineering, *Advanced Drug Delivery Reviews*, 60(2), 184-198.
- [11] **Dhandayuthapani, B., Yoshida, Y., Maekawa, T., and Kumar, D. S.** (2011). Polymeric scaffolds in tissue engineering application: a review, *International Journal of Polymer Science*, 2011, 1-19.
- [12] **Anaraki, N. A., Rad, L. R., Irani, M., and Haririan, I.** (2014). Fabrication of PLA/PEG/MWCNT electrospun nanofibrous scaffolds for anticancer drug delivery, *Journal of Applied Polymer Science*, 3(132), 41286.

- [13] **Anindyajati, A., Boughton, P., and Ruys, A.** (2018). Modelling and optimization of Polycaprolactone ultrafine-fibres electrospinning process using response surface methodology, *Materials*, *11*(3), 441.
- [14] **Bhardwaj, N., and Kundu, S. C.** (2010). Electrospinning: a fascinating fiber fabrication technique, *Biotechnology Advances*, *28*(3), 325-347.
- [15] **Gao, X., Han, S., Zhang, R., Liu, G., and Wu, J.** (2019). Progress in electrospun composite nanofibers: composition, performance and applications for tissue engineering, *Journal of Materials Chemistry B*, *7*(45), 7075-7089.
- [16] **Rodríguez-Tobías, H., Morales, G., and Grande, D.** (2019). Comprehensive review on electrospinning techniques as versatile approaches toward antimicrobial biopolymeric composite fibers, *Materials Science and Engineering: C*, *101*, 306-322.
- [17] **Heidari, M., Bahrami, H., and Ranjbar-Mohammadi, M.** (2017). Fabrication, optimization and characterization of electrospun poly (caprolactone)/gelatin/graphene nanofibrous mats, *Materials Science and Engineering: C*, *78*, 218-229.
- [18] **Allo, B. A., Lin, S., Mequanint, K., and Rizkalla, A. S.** (2013). Role of bioactive 3D hybrid fibrous scaffolds on mechanical behavior and spatiotemporal osteoblast gene expression, *ACS Applied Materials & Interfaces*, *5*(15), 7574-7583.
- [19] **Balasubramanian, P., Roether, J. A., Schubert, D. W., Beier, J. P., and Boccaccini, A. R.** (2015). Bi-layered porous constructs of PCL-coated 45S5 bioactive glass and electrospun collagen-PCL fibers, *Journal of Porous Materials*, *22*(5), 1215-1226.
- [20] **Gerhardt, L.-C., and Boccaccini, A. R.** (2010). Bioactive glass and glass-ceramic scaffolds for bone tissue engineering, *Materials*, *3*(7), 3867-3910.
- [21] **Boccaccini, A. R., and Maquet, V.** (2003). Bioresorbable and bioactive polymer/Bioglass® composites with tailored pore structure for tissue engineering applications, *Composites Science and Technology*, *63*(16), 2417-2429.
- [22] **Sheikh, F. A., Kanjwal, M. A., Saran, S., Chung, W.-J., and Kim, H.** (2011). Polyurethane nanofibers containing copper nanoparticles as future materials, *Applied Surface Science*, *257*(7), 3020-3026.
- [23] **Abdelgawad, A. M., Hudson, S. M., and Rojas, O. J.** (2014). Antimicrobial wound dressing nanofiber mats from multicomponent (chitosan/silver-NPs/polyvinyl alcohol) systems, *Carbohydrate Polymers*, *100*, 166-178.
- [24] **Sheikh, F. A., Woo Ju, H., Mi Moon, B., Jung Park, H., Kim, J. H., Joo Lee, O., and Hum Park, C.** (2014). Facile and highly efficient approach for the fabrication of multifunctional silk nanofibers containing hydroxyapatite and silver nanoparticles, *Journal of Biomedical Materials Research Part A*, *102*(10), 3459-3469.

- [25] **Caramella, C., Conti, B., Modena, T., Ferrari, F., Bonferoni, M. C., Genta, I., Rossi, S., Torre, M. L., Sandri, G., and Sorrenti, M.** (2016). Controlled delivery systems for tissue repair and regeneration, *Journal of Drug Delivery Science and Technology*, 32, 206-228.
- [26] **Berton, F., Porrelli, D., Di Lenarda, R., and Turco, G.** (2020). A Critical Review on the Production of Electrospun Nanofibres for Guided Bone Regeneration in Oral Surgery, *Nanomaterials*, 10(1), 16.
- [27] **Kishan, A. P., and Cosgriff-Hernandez, E. M.** (2017). Recent advancements in electrospinning design for tissue engineering applications: a review, *Journal of Biomedical Materials Research Part A*, 105(10), 2892-2905.
- [28] **Huang, Z.-M., Zhang, Y.-Z., Kotaki, M., and Ramakrishna, S.** (2003). A review on polymer nanofibers by electrospinning and their applications in nanocomposites, *Composites Science and Technology*, 63(15), 2223-2253.
- [29] **Chen, G., Ushida, T., and Tateishi, T.** (2002). Scaffold design for tissue engineering, *Macromolecular Bioscience*, 2(2), 67-77.
- [30] **Wade, R. J., and Burdick, J. A.** (2014). Advances in nanofibrous scaffolds for biomedical applications: From electrospinning to self-assembly, *Nano Today*, 9(6), 722-742.
- [31] **Khatti, T., Naderi-Manesh, H., and Kalantar, S. M.** (2019). Application of ANN and RSM techniques for modeling electrospinning process of polycaprolactone, *Neural Computing and Applications*, 31(1), 239-248.
- [32] **Khan, G., Yadav, S. K., Patel, R. R., Kumar, N., Bansal, M., and Mishra, B.** (2017). Tinidazole functionalized homogeneous electrospun chitosan/poly (ϵ -caprolactone) hybrid nanofiber membrane: development, optimization and its clinical implications, *International Journal of Biological Macromolecules*, 103, 1311-1326.
- [33] **Neo, Y. P., Ray, S., Easteal, A. J., Nikolaidis, M. G., and Quek, S. Y.** (2012). Influence of solution and processing parameters towards the fabrication of electrospun zein fibers with sub-micron diameter, *Journal of Food Engineering*, 109(4), 645-651.
- [34] **Shimizu, A., Kato, H., Sato, T., and Kushida, M.** (2017). Preparation and characterization of oriented poly (vinyl alcohol)/carbon nanotube composite nanofibers, *Japanese Journal of Applied Physics*, 56(7S2), 07KD02.
- [35] **Veverková, I., and Lovětinská-Šlamborová, I.** (2016). Modified Silica Nanofibers with Antibacterial Activity, *Journal of Nanomaterials*, 2016, 1-6.
- [36] **Zamani, Y., Rabiee, M., Shokrgozar, M. A., Bonakdar, S., and Tahriri, M.** (2013). Response of human mesenchymal stem cells to patterned and randomly oriented poly (vinyl alcohol) nano-fibrous scaffolds surface-modified with Arg-Gly-Asp (RGD) ligand, *Applied Biochemistry and Biotechnology*, 171(6), 1513-1524.

- [37] **Sajeev, U., Anand, K. A., Menon, D., and Nair, S.** (2008). Control of nanostructures in PVA, PVA/chitosan blends and PCL through electrospinning, *Bulletin of Materials Science*, 31(3), 343-351.
- [38] **Wei, Y., Zhang, X., Song, Y., Han, B., Hu, X., Wang, X., Lin, Y., and Deng, X.** (2011). Magnetic biodegradable Fe₃O₄/CS/PVA nanofibrous membranes for bone regeneration, *Biomedical Materials*, 6(5), 055008.
- [39] **Franco, R. A., Sadiasa, A., and Lee, B. T.** (2014). Utilization of PVPA and its effect on the material properties and biocompatibility of PVA electrospun membrane, *Polymers for Advanced Technologies*, 25(1), 55-65.
- [40] **Tan, Z., Wang, H., Gao, X., Liu, T., and Tan, Y.** (2016). Composite vascular grafts with high cell infiltration by co-electrospinning, *Materials Science and Engineering: C*, 67, 369-377.
- [41] **Heseltine, P. L., Ahmed, J., and Edirisinghe, M.** (2018). Developments in pressurized gyration for the mass production of polymeric fibers, *Macromolecular Materials and Engineering*, 303(9), 1800218.
- [42] **Matharu, R. K., Porwal, H., Ciric, L., and Edirisinghe, M.** (2018). The effect of graphene–poly (methyl methacrylate) fibres on microbial growth, *Interface Focus*, 8(3), 20170058.
- [43] **Chun, J. Y., Kang, H. K., Jeong, L., Kang, Y. O., Oh, J.-E., Yeo, I.-S., Jung, S. Y., Park, W. H., and Min, B.-M.** (2010). Epidermal cellular response to poly (vinyl alcohol) nanofibers containing silver nanoparticles, *Colloids and Surfaces B: Biointerfaces*, 78(2), 334-342.
- [44] **Hong, K. H., Park, J. L., Sul, I. H., Youk, J. H., and Kang, T. J.** (2006). Preparation of antimicrobial poly (vinyl alcohol) nanofibers containing silver nanoparticles, *Journal of Polymer Science Part B: Polymer Physics*, 44(17), 2468-2474.
- [45] **Kim, G.-M., Asran, A. S., Michler, G. H., Simon, P., and Kim, J.-S.** (2008). Electrospun PVA/HAp nanocomposite nanofibers: biomimetics of mineralized hard tissues at a lower level of complexity, *Bioinspiration & Biomimetics*, 3(4), 046003.
- [46] **Lee, Y. J., and Lyoo, W. S.** (2009). Preparation and characterization of high-molecular-weight atactic poly (vinyl alcohol)/sodium alginate/silver nanocomposite by electrospinning, *Journal of Polymer Science Part B: Polymer Physics*, 47(19), 1916-1926.
- [47] **Du, L., Xu, H., Li, T., Zhang, Y., and Zou, F.** (2016). Fabrication of silver nanoparticle/polyvinyl alcohol/polycaprolactone hybrid nanofibers nonwovens by two-nozzle electrospinning for wound dressing, *Fibers and Polymers*, 17(12), 1995-2005.
- [48] **Hong, K. H.** (2007). Preparation and properties of electrospun poly (vinyl alcohol)/silver fiber web as wound dressings, *Polymer Engineering & Science*, 47(1), 43-49.

- [49] **Park, J. H., Kim, I. K., Choi, J. Y., Karim, M. R., Cheong, I. W., Oh, W., and Yeum, J. H.** (2011). Electrospinning fabrication of poly (vinyl alcohol)/waterborne polyurethane/silver composite nanofibre mats in aqueous solution for anti-bacterial exploits, *Polymers & Polymer Composites*, 19(9), 753.
- [50] **Hang, A. T., Tae, B., and Park, J. S.** (2010). Non-woven mats of poly (vinyl alcohol)/chitosan blends containing silver nanoparticles: fabrication and characterization, *Carbohydrate Polymers*, 82(2), 472-479.
- [51] **Segala, K., Nista, S. V. G., Cordi, L., Bizarria, M. T. M., Ávila Júnior, J. d., Kleinubing, S. A., Cruz, D. C., Brocchi, M., Lona, L. M. F., and Caballero, N. E. D.** (2015). Silver nanoparticles incorporated into nanostructured biopolymer membranes produced by electrospinning: a study of antimicrobial activity, *Brazilian Journal of Pharmaceutical Sciences*, 51(4), 911-921.
- [52] **Matharu, R. K., Ciric, L., and Edirisinghe, M.** (2018). Nanocomposites: suitable alternatives as antimicrobial agents, *Nanotechnology*, 29(28), 282001.
- [53] **Aswathy, B., Avadhani, G., Sumithra, I., Suji, S., and Sony, G.** (2011). Microwave assisted synthesis and UV-Vis spectroscopic studies of silver nanoparticles synthesized using vanillin as a reducing agent, *Journal of Molecular Liquids*, 159(2), 165-169.
- [54] **Huang, S., Wang, J., Zhang, Y., Yu, Z., and Qi, C.** (2016). Quaternized carboxymethyl chitosan-based silver nanoparticles hybrid: microwave-assisted synthesis, characterization and antibacterial activity, *Nanomaterials*, 6(6), 118.
- [55] **Velusamy, P., Su, C.-H., Kumar, G. V., Adhikary, S., Pandian, K., Gopinath, S. C., Chen, Y., and Anbu, P.** (2016). Biopolymers regulate silver nanoparticle under microwave irradiation for effective antibacterial and antibiofilm activities, *PloS One*, 11(6), e0157612.
- [56] **Oluwafemi, O. S., Mochochoko, T., Leo, A. J., Mohan, S., Jumbam, D. N., and Songca, S. P.** (2016). Microwave irradiation synthesis of silver nanoparticles using cellulose from Eichhornia crassipes plant shoot, *Materials Letters*, 185, 576-579.
- [57] **Cano, A., Cháfer, M., Chiralt, A., and González-Martínez, C.** (2016). Development and characterization of active films based on starch-PVA, containing silver nanoparticles, *Food Packaging and Shelf Life*, 10, 16-24.
- [58] **Gu, Y., Li, N., Gao, M., Wang, Z., Xiao, D., Li, Y., Jia, H., and He, H.** (2015). Microwave-assisted synthesis of BSA-modified silver nanoparticles as a selective fluorescent probe for detection and cellular imaging of cadmium (II), *Microchimica Acta*, 182(7-8), 1255-1261.
- [59] **Hu, B., Wang, S.-B., Wang, K., Zhang, M., and Yu, S.-H.** (2008). Microwave-assisted rapid facile “green” synthesis of uniform silver nanoparticles: self-assembly into multilayered films and their optical properties, *The Journal of Physical Chemistry C*, 112(30), 11169-11174.

- [60] **Božanić, D., Dimitrijević-Branković, S., Bibić, N., Luyt, A., and Djoković, V.** (2011). Silver nanoparticles encapsulated in glycogen biopolymer: Morphology, optical and antimicrobial properties, *Carbohydrate Polymers*, 83(2), 883-890.
- [61] **Zhao, X., Xia, Y., Li, Q., Ma, X., Quan, F., Geng, C., and Han, Z.** (2014). Microwave-assisted synthesis of silver nanoparticles using sodium alginate and their antibacterial activity, *Colloids and Surfaces A: Physicochemical and Engineering Aspects*, 444, 180-188.
- [62] **Zain, N. M., Stapley, A., and Shama, G.** (2014). Green synthesis of silver and copper nanoparticles using Ascorbic acid and Chitosan for antimicrobial applications, *Carbohydrate Polymers*, 112, 195-202.
- [63] **Nguyen, N. T., Nguyen, B. H., Ba, D. T., Pham, D. G., Van Khai, T., Nguyen, L. T., and Tran, L. D.** (2014). Microwave-assisted synthesis of silver nanoparticles using Chitosan: A novel approach, *Materials and Manufacturing Processes*, 29(4), 418-421.
- [64] **Valodkar, M., Modi, S., Pal, A., and Thakore, S.** (2011). Synthesis and antibacterial activity of Cu, Ag and Cu-Ag alloy nanoparticles: a green approach, *Materials Research Bulletin*, 46(3), 384-389.
- [65] **Sreeram, K., Nidhin, M., and Nair, B.** (2008). Microwave assisted template synthesis of silver nanoparticles, *Bulletin of Materials Science*, 31(7), 937-942.
- [66] **Kahrilas, G. A., Haggren, W., Read, R. L., Wally, L. M., Fredrick, S. J., Hiskey, M., Prieto, A. L., and Owens, J. E.** (2014). Investigation of antibacterial activity by silver nanoparticles prepared by microwave-assisted green syntheses with soluble starch, dextrose, and arabinose, *ACS Sustainable Chemistry & Engineering*, 2(4), 590-598.
- [67] **Joseph, S., and Mathew, B.** (2015). Facile synthesis of silver nanoparticles and their application in dye degradation, *Materials Science and Engineering: B*, 195, 90-97.
- [68] **Han, Y., Luo, Z., Yuwen, L., Tian, J., Zhu, X., and Wang, L.** (2013). Synthesis of silver nanoparticles on reduced graphene oxide under microwave irradiation with starch as an ideal reductant and stabilizer, *Applied Surface Science*, 266, 188-193.
- [69] **Raveendran, P., Fu, J., and Wallen, S. L.** (2006). A simple and “green” method for the synthesis of Au, Ag, and Au-Ag alloy nanoparticles, *Green Chemistry*, 8(1), 34-38.
- [70] **Silva, A. R., and Unali, G.** (2011). Controlled silver delivery by silver-cellulose nanocomposites prepared by a one-pot green synthesis assisted by microwaves, *Nanotechnology*, 22(31), 315605.
- [71] **Chen, J., Wang, J., Zhang, X., and Jin, Y.** (2008). Microwave-assisted green synthesis of silver nanoparticles by carboxymethyl cellulose sodium and silver nitrate, *Materials Chemistry and Physics*, 108(2-3), 421-424.
- [72] **Wang, B., Zhuang, X., Deng, W., and Cheng, B.** (2010). Microwave-assisted synthesis of silver nanoparticles in alkalic carboxymethyl chitosan solution, *Engineering*, 2(05), 387.

- [73] **Singh, S., Bharti, A., and Meena, V. K.** (2015). Green synthesis of multi-shaped silver nanoparticles: optical, morphological and antibacterial properties, *Journal of Materials Science: Materials in Electronics*, 26(6), 3638-3648.
- [74] **El-Rafie, M., Ahmed, H. B., and Zahran, M.** (2014). Facile precursor for synthesis of silver nanoparticles using alkali treated maize starch, *International Scholarly Research Notices*, 2014, (1-12).
- [75] **Yakout, S. M., and Mostafa, A. A.** (2015). A novel green synthesis of silver nanoparticles using soluble starch and its antibacterial activity, *International Journal of Clinical and Experimental Medicine*, 8(3), 3538.
- [76] **Martínez-Rodríguez, M., Garza-Navarro, M., Moreno-Cortez, I., Lucio-Porto, R., and González-González, V.** (2016). Silver/polysaccharide-based nanofibrous materials synthesized from green chemistry approach, *Carbohydrate Polymers*, 136, 46-53.
- [77] **Usman, A., Hussain, Z., Riaz, A., and Khan, A. N.** (2016). Enhanced mechanical, thermal and antimicrobial properties of poly (vinyl alcohol)/graphene oxide/starch/silver nanocomposites films, *Carbohydrate Polymers*, 153, 592-599.
- [78] **Van Phu, D., Duy, N. N., Lan, N. T. K., Du, B. D., and Hien, N. Q.** (2014). Study on antibacterial activity of silver nanoparticles synthesized by gamma irradiation method using different stabilizers, *Nanoscale Research Letters*, 9(1), 162.
- [79] **Kumar, A., and Jaiswal, M.** (2016). Design and in vitro investigation of nanocomposite hydrogel based in situ spray dressing for chronic wounds and synthesis of silver nanoparticles using green chemistry, *Journal of Applied Polymer Science*, 133(14), 43260.
- [80] **Cheon, J. Y., Kang, Y. O., and Park, W. H.** (2015). Formation of Ag nanoparticles in PVA solution and catalytic activity of their electrospun PVA nanofibers, *Fibers and Polymers*, 16(4), 840-849.
- [81] **Islam, M. S., and Yeum, J. H.** (2013). Electrospun pullulan/poly (vinyl alcohol)/silver hybrid nanofibers: preparation and property characterization for antibacterial activity, *Colloids and Surfaces A: Physicochemical and Engineering Aspects*, 436, 279-286.
- [82] **Zhang, Z., Wu, Y., Wang, Z., Zou, X., Zhao, Y., and Sun, L.** (2016). Fabrication of silver nanoparticles embedded into polyvinyl alcohol (Ag/PVA) composite nanofibrous films through electrospinning for antibacterial and surface-enhanced Raman scattering (SERS) activities, *Materials Science and Engineering: C*, 69, 462-469.
- [83] **Lin, S., Wang, R.-Z., Yi, Y., Wang, Z., Hao, L.-M., Wu, J.-H., Hu, G.-H., and He, H.** (2014). Facile and green fabrication of electrospun poly (vinyl alcohol) nanofibrous mats doped with narrowly dispersed silver nanoparticles, *International Journal of Nanomedicine*, 9, 3937.

- [84] **Mahanta, N., and Valiyaveettil, S.** (2012). In situ preparation of silver nanoparticles on biocompatible methacrylated poly (vinyl alcohol) and cellulose based polymeric nanofibers, *RSC Advances*, 2(30), 11389-11396.
- [85] **Cheng, Z., Zhang, F., Liu, W., Cui, L., and Kang, L.** (2015). A novel preparation for a PVA/l-histidine/AgNPs membrane and its antibacterial property, *RSC Advances*, 5(67), 54182-54187.
- [86] **Celebioglu, A., Aytac, Z., Umu, O. C., Dana, A., Tekinay, T., and Uyar, T.** (2014). One-step synthesis of size-tunable Ag nanoparticles incorporated in electrospun PVA/cyclodextrin nanofibers, *Carbohydrate Polymers*, 99, 808-816.
- [87] **Li, C., Fu, R., Yu, C., Li, Z., Guan, H., Hu, D., Zhao, D., and Lu, L.** (2013). Silver nanoparticle/chitosan oligosaccharide/poly (vinyl alcohol) nanofibers as wound dressings: a preclinical study, *International Journal of Nanomedicine*, 8, 4131.
- [88] **Xiao, S., Xu, W., Ma, H., and Fang, X.** (2012). Size-tunable Ag nanoparticles immobilized in electrospun nanofibers: synthesis, characterization, and application for catalytic reduction of 4-nitrophenol, *RSC Advances*, 2(1), 319-327.
- [89] **Vigneshwaran, N., Nachane, R., Balasubramanya, R., and Varadarajan, P.** (2006). A novel one-pot 'green' synthesis of stable silver nanoparticles using soluble starch, *Carbohydrate Research*, 341(12), 2012-2018.
- [90] **Zaheer, Z., Aazam, E. S., and Hussain, S.** (2016). Reversible encapsulation of silver nanoparticles into the helix of amylose (water soluble starch), *RSC Advances*, 6(65), 60513-60521.
- [91] **Valencia, G. A., de Oliveira Vercik, L. C., Ferrari, R., and Vercik, A.** (2013). Synthesis and characterization of silver nanoparticles using water-soluble starch and its antibacterial activity on *Staphylococcus aureus*, *Starch-Stärke*, 65(11-12), 931-937.
- [92] **Şimşek, M., Rzaev, Z. M., and Bunyatova, U.** (2016). Multifunctional electroactive electrospun nanofiber structures from water solution blends of PVA/ODA–MMT and poly (maleic acid-alt-acrylic acid): Effects of Ag, organoclay, structural rearrangement and NaOH doping factors, *Advances in Natural Sciences: Nanoscience and Nanotechnology*, 7(2), 025009.
- [93] **Rogojanu, A., Rusu, E., Olaru, N., Dobromir, M., and Dorohoi, D.** (2011). Development and characterization of poly (vinyl alcohol) matrix for drug release, *Digest Journal of Nanomaterials & Biostructures (DJNB)*, 6(2), 809-818.
- [94] **Destaye, A. G., Lin, C.-K., and Lee, C.-K.** (2013). Glutaraldehyde vapor cross-linked nanofibrous PVA mat with in situ formed silver nanoparticles, *ACS Applied Materials & Interfaces*, 5(11), 4745-4752.

- [95] **Sui, C., Li, C., Guo, X., Cheng, T., Gao, Y., Zhou, G., Gong, J., and Du, J.** (2012). Facile synthesis of silver nanoparticles-modified PVA/H₄SiW₁₂O₄₀ nanofibers-based electrospinning to enhance photocatalytic activity, *Applied Surface Science*, 258(18), 7105-7111.
- [96] **Munteanu, B. S., Aytac, Z., Pricope, G. M., Uyar, T., and Vasile, C.** (2014). Polylactic acid (PLA)/Silver-NP/VitaminE bionanocomposite electrospun nanofibers with antibacterial and antioxidant activity, *Journal of Nanoparticle Research*, 16(10), 2643.
- [97] **Zhao, Y., Zhou, Y., Wu, X., Wang, L., Xu, L., and Wei, S.** (2012). A facile method for electrospinning of Ag nanoparticles/poly (vinyl alcohol)/carboxymethyl-chitosan nanofibers, *Applied Surface Science*, 258(22), 8867-8873.
- [98] **Wang, R., Wang, Z., Lin, S., Deng, C., Li, F., Chen, Z., and He, H.** (2015). Green fabrication of antibacterial polymer/silver nanoparticle nanohybrids by dual-spinneret electrospinning, *RSC Advances*, 5(50), 40141-40147.
- [99] **Boaretti, C., Roso, M., Lorenzetti, A., and Modesti, M.** (2015). Synthesis and Process Optimization of Electrospun PEEK-Sulfonated Nanofibers by Response Surface Methodology, *Materials*, 8(7), 4096-4117.
- [100] **Gönen, S. Ö., Erol Taygun, M., and Küçükbayrak, S.** (2016). Evaluation of the factors influencing the resultant diameter of the electrospun gelatin/sodium alginate nanofibers via Box–Behnken design, *Materials Science and Engineering: C*, 58, 709-723.
- [101] **Pezeshki-Modaress, M., Mirzadeh, H., and Zandi, M.** (2015). Gelatin–GAG electrospun nanofibrous scaffold for skin tissue engineering: fabrication and modeling of process parameters, *Materials Science and Engineering: C*, 48, 704-712.
- [102] **Thirugnanasambandham, K., and Sivakumar, V.** (2016). Preparation of chitosan based nanofibers: Optimization and modeling, *International Journal of Chemical Reactor Engineering*, 14(1), 283-288.
- [103] **Stoddard, R., and Chen, X.** (2016). Electrospinning of ultra-thin nanofibers achieved through comprehensive statistical study, *Materials Research Express*, 3(5), 055022.
- [104] **Sachot, N., Castano, O., Planell, J. A., and Engel, E.** (2015). Optimization of blend parameters for the fabrication of polycaprolactone-silicon based ormoglass nanofibers by electrospinning, *Journal of Biomedical Materials Research Part B: Applied Biomaterials*, 103(6), 1287-1293.
- [105] **Pezeshki-Modaress, M., Zandi, M., and Mirzadeh, H.** (2015). Fabrication of gelatin/chitosan nanofibrous scaffold: process optimization and empirical modeling, *Polymer International*, 64(4), 571-580.
- [106] **Konwarh, R., Misra, M., Mohanty, A. K., and Karak, N.** (2013). Diameter-tuning of electrospun cellulose acetate fibers: A Box–Behnken design (BBD) study, *Carbohydrate Polymers*, 92(2), 1100-1106.

- [107] **Khan, G., Patel, R. R., Yadav, S. K., Kumar, N., Chaurasia, S., Ajmal, G., Mishra, P. K., and Mishra, B.** (2016). Development, optimization and evaluation of tinidazole functionalized electrospun poly (ϵ -caprolactone) nanofiber membranes for the treatment of periodontitis, *RSC Advances*, 6(102), 100214-100229.
- [108] **Khalili, S., Khorasani, S. N., Saadatkish, N., and Khoshakhlagh, K.** (2016). Characterization of gelatin/cellulose acetate nanofibrous scaffolds: prediction and optimization by response surface methodology and artificial neural networks, *Polymer Science Series A*, 58(3), 399-408.
- [109] **Jacobs, V., Patanaik, A., D Anandjiwala, R., and Maaza, M.** (2011). Optimization of electrospinning parameters for chitosan nanofibres, *Current Nanoscience*, 7(3), 396-401.
- [110] **Irani, M., Sadeghi, G. M. M., and Haririan, I.** (2017). The sustained delivery of temozolomide from electrospun PCL-Diol-b-PU/gold nanocomposite nanofibers to treat glioblastoma tumors, *Materials Science and Engineering: C*, 75, 165-174.
- [111] **Hossain, M. F., Gong, R. H., and Rigout, M.** (2016). Optimization of the process variables for electrospinning of poly (ethylene oxide)-loaded hydroxypropyl- β -cyclodextrin nanofibres, *The Journal of The Textile Institute*, 107(1), 1-11.
- [112] **Hakkak, F., Rafizadeh, M., Sarabi, A. A., and Yousefi, M.** (2015). Optimization of ionic conductivity of electrospun polyacrylonitrile/poly (vinylidene fluoride)(PAN/PVdF) electrolyte using the response surface method (RSM), *Ionics*, 21(7), 1945-1957.
- [113] **Gönen, S. Ö., Erol Taygun, M., and Küçükbayrak, S.** (2015). Effects of Electrospinning Parameters on Gelatin/Poly (ϵ -Caprolactone) Nanofiber Diameter, *Chemical Engineering & Technology*, 38(5), 844-850.
- [114] **Gönen, S. Ö., Erol Taygun, M., Aktürk, A., and Küçükbayrak, S.** (2016). Fabrication of nanocomposite mat through incorporating bioactive glass particles into gelatin/poly (ϵ -caprolactone) nanofibers by using Box–Behnken design, *Materials Science and Engineering: C*, 67, 684-693.
- [115] **Dott, C., Tyagi, C., Tomar, L. K., Choonara, Y. E., Kumar, P., du Toit, L. C., and Pillay, V.** (2013). A mucoadhesive electrospun nanofibrous matrix for rapid oramucosal drug delivery, *Journal of Nanomaterials*, 2013, 924947.
- [116] **Dhurai, B., Saraswathy, N., Maheswaran, R., Sethupathi, P., Vanitha, P., Vigneshwaran, S., and Rameshbabu, V.** (2013). Electrospinning of curcumin loaded chitosan/poly (lactic acid) nanofilm and evaluation of its medicinal characteristics, *Frontiers of Materials Science*, 7(4), 350-361.
- [117] **Dhurai, B., Nachimuthu, S., Kumar, G., and Babu, R.** (2013). Electrospinning of chitosan nanofibres loaded with curcumin for wound healing, *Journal of Polymer Materials*, 30(4), 471.

- [118] **Zarghami, A., Irani, M., Mostafazadeh, A., Golpour, M., Heidarinasab, A., and Haririan, I.** (2015). Fabrication of PEO/chitosan/PCL/olive oil nanofibrous scaffolds for wound dressing applications, *Fibers and Polymers*, 16(6), 1201-1212.
- [119] **Selvam, A. K., and Nallathambi, G.** (2015). Polyacrylonitrile/silver nanoparticle electrospun nanocomposite matrix for bacterial filtration, *Fibers and Polymers*, 16(6), 1327-1335.
- [120] **Akhtar, M. N., Sulong, A. B., Karim, S. A., Azhari, C. H., and Raza, M.** (2015). Evaluation of thermal, morphological and mechanical properties of PMMA/NaCl/DMF electrospun nanofibers: an investigation through surface methodology approach, *Iranian Polymer Journal*, 24(12), 1025-1038.
- [121] **Aliabadi, M., Irani, M., Ismaeili, J., and Najafzadeh, S.** (2014). Design and evaluation of chitosan/hydroxyapatite composite nanofiber membrane for the removal of heavy metal ions from aqueous solution, *Journal of the Taiwan Institute of Chemical Engineers*, 45(2), 518-526.
- [122] **Jeong, L., and Park, W. H.** (2014). Preparation and characterization of gelatin nanofibers containing silver nanoparticles, *International Journal of Molecular Sciences*, 15(4), 6857-6879.
- [123] **Gao, C., Gao, Q., Li, Y., Rahaman, M. N., Teramoto, A., and Abe, K.** (2013). In vitro evaluation of electrospun gelatin-bioactive glass hybrid scaffolds for bone regeneration, *Journal of Applied Polymer Science*, 127(4), 2588-2599.
- [124] **Naghizadeh, M., and Adabi, M.** (2014). Evaluation of effective electrospinning parameters controlling gelatin nanofibers diameter via modelling artificial neural networks, *Fibers and Polymers*, 15(4), 767-777.
- [125] **Tofoleanu, F., Balau, M. T., Brinza, F., Sulitanu, N., Sandu, I., Raileanu, D., Floristean, V., Hagi, B., Ionescu, C., and Sandu, I.** (2010). Electrospun Gelatin Nanofibers Functionalized with Silver Nanoparticles, *Journal of Optoelectronics and Advanced Materials*, 10(12), 3512-3516.
- [126] **Ardeshirylajimi, A., Farhadian, S., Jamshidi Adegani, F., Mirzaei, S., Soufi Zomorrod, M., Langroudi, L., Doostmohammadi, A., Seyedjafari, E., and Soleimani, M.** (2015). Enhanced osteoconductivity of polyethersulphone nanofibres loaded with bioactive glass nanoparticles in in vitro and in vivo models, *Cell Proliferation*, 48(4), 455-464.
- [127] **Baylan, N., and Çehreli, S.** (2019). Experimental and modeling study for the removal of formic acid through bulk ionic liquid membrane using response surface methodology, *Chemical Engineering Communications*, 1-14.

- [128] Aktürk, A., Erol Taygun, M., Karbancıoğlu Güler, F., Göller, G., and Küçükbayrak, S. (2019). Fabrication of Antibacterial Polyvinylalcohol Nanocomposite Mats with Soluble Starch Coated Silver Nanoparticles, *Colloids and Surfaces A: Physicochemical and Engineering Aspects*, 562, 255-262.
- [129] Lepry, W. C., Smith, S., Liverani, L., Boccaccini, A. R., and Nazhat, S. N. (2016). Acellular bioactivity of sol-gel derived borate glass-polycaprolactone electrospun scaffolds, *Biomedical Glasses*, 2(1), 88-98.
- [130] De Sá, K. D., Figueira, D. R., Miguel, S. P., Correia, T. R., Silva, A. P., and Correia, I. J. (2017). 3D scaffolds coated with nanofibers displaying bactericidal activity for bone tissue applications, *International Journal of Polymeric Materials and Polymeric Biomaterials*, 66(9), 432-442.
- [131] Liu, F., Wang, X., Chen, T., Zhang, N., Wei, Q., Tian, J., Wang, Y., Ma, C., and Lu, Y. (2020). Hydroxyapatite/silver electrospun fibers for anti-infection and osteoinduction, *Journal of Advanced Research*, 21, 91-102.
- [132] Cheng, X., Wei, Q., Ma, Y., Shi, R., Chen, T., Wang, Y., Ma, C., and Lu, Y. (2020). Antibacterial and osteoinductive biomacromolecules composite electrospun fiber, *International Journal of Biological Macromolecules*, 143, 958-967.
- [133] Lee, D., Lee, S. J., Moon, J.-H., Kim, J. H., Heo, D. N., Bang, J. B., Lim, H.-N., and Kwon, I. K. (2018). Preparation of antibacterial chitosan membranes containing silver nanoparticles for dental barrier membrane applications, *Journal of Industrial and Engineering Chemistry*, 66, 196-202.
- [134] Sumitha, M., Shalumon, K., Sreeja, V., Jayakumar, R., Nair, S. V., and Menon, D. (2012). Biocompatible and antibacterial nanofibrous poly(ϵ -caprolactone)-nanosilver composite scaffolds for tissue engineering applications, *Journal of Macromolecular Science, Part A*, 49(2), 131-138.
- [135] Kwak, H. W., Kim, J. E., and Lee, K. H. (2019). Green fabrication of antibacterial gelatin fiber for biomedical application, *Reactive and Functional Polymers*, 136, 86-94.
- [136] Baylan, N., and Çehreli, S. (2018). Ionic liquids as bulk liquid membranes on levulinic acid removal: A design study, *Journal of Molecular Liquids*, 266, 299-308.
- [137] Baylan, N., and Çehreli, S. (2019). Removal of acetic acid from aqueous solutions using bulk ionic liquid membranes: A transport and experimental design study, *Separation and Purification Technology*, 224, 51-61.
- [138] Owolabi, R. U., Usman, M. A., and Kehinde, A. J. (2016). Modelling and optimization of process variables for the solution polymerization of styrene using response surface methodology, *Journal of King Saud University-Engineering Sciences*, 30(1), 22-30.

- [139] **Sunandhakumari, V., Vidhyadharan, A., Alim, A., Kumar, D., Ravindran, J., Krishna, A., and Prasad, M.** (2018). Fabrication and In Vitro Characterization of Bioactive Glass/Nano Hydroxyapatite Reinforced Electrospun Poly (ϵ -Caprolactone) Composite Membranes for Guided Tissue Regeneration, *Bioengineering*, 5(3), 54.
- [140] **Foroughi, M. R., Karbasi, S., Khoroushi, M., and Khademi, A. A.** (2017). Polyhydroxybutyrate/chitosan/bioglass nanocomposite as a novel electrospun scaffold: Fabrication and characterization, *Journal of Porous Materials*, 24(6), 1447-1460.
- [141] **Li, C. W., Wang, Q., Li, J., Hu, M., Shi, S. J., Li, Z. W., Wu, G. L., Cui, H. H., Li, Y. Y., and Zhang, Q.** (2016). Silver nanoparticles/chitosan oligosaccharide/poly (vinyl alcohol) nanofiber promotes wound healing by activating TGF β 1/Smad signaling pathway, *International Journal of Nanomedicine*, 11, 373.
- [142] **Homayoni, H., Ravandi, S. A. H., and Valizadeh, M.** (2009). Electrospinning of chitosan nanofibers: processing optimization, *Carbohydrate Polymers*, 77(3), 656-661.
- [143] **Jose, M. V., Thomas, V., Johnson, K. T., Dean, D. R., and Nyairo, E.** (2009). Aligned PLGA/HA nanofibrous nanocomposite scaffolds for bone tissue engineering, *Acta Biomaterialia*, 5(1), 305-315.
- [144] **Ouis, M. A., Abdelghany, A. M., and ElBatal, H. A.** (2012). Corrosion mechanism and bioactivity of borate glasses analogue to Hench's bioglass, *Processing and Application of Ceramics*, 6(3), 141-149.
- [145] **Gönen, S. Ö., Erol Taygun, M., and Küçükbayrak, S.** (2016). Fabrication of bioactive glass containing nanocomposite fiber mats for bone tissue engineering applications, *Composite Structures*, 138, 96-106.
- [146] **Chen, J., Zeng, L., Chen, X., Liao, T., and Zheng, J.** (2018). Preparation and characterization of bioactive glass tablets and evaluation of bioactivity and cytotoxicity in vitro, *Bioactive Materials*, 3(3), 315-321.
- [147] **Shamsi, M., Karimi, M., Ghollasi, M., Nezafati, N., Shahrousvand, M., Kamali, M., and Salimi, A.** (2017). In vitro proliferation and differentiation of human bone marrow mesenchymal stem cells into osteoblasts on nanocomposite scaffolds based on bioactive glass (64SiO₂-31CaO-5P₂O₅)-poly-l-lactic acid nanofibers fabricated by electrospinning method, *Materials Science and Engineering: C*, 78, 114-123.
- [148] **Xu, X., and Zhou, M.** (2008). Antimicrobial gelatin nanofibers containing silver nanoparticles, *Fibers and Polymers*, 9(6), 685-690.
- [149] **Hossan, M. J., Gafur, M., Kadir, M., and Karim, M. M.** (2014). Preparation and characterization of gelatin-hydroxyapatite composite for bone tissue engineering, *International Journal of Engineering & Technology*, 14, 24-32.

- [150] **Duhoranimana, E., Karangwa, E., Lai, L., Xu, X., Yu, J., Xia, S., Zhang, X., Muhoza, B., and Habinshtuti, I.** (2017). Effect of sodium carboxymethyl cellulose on complex coacervates formation with gelatin: Coacervates characterization, stabilization and formation mechanism, *Food Hydrocolloids*, *69*, 111-120.
- [151] **Lip, L. W., Abdullah, T. K., and Zubir, S. A.** (2016). Effect of polyurethane (PU)–bioactive glass (BG) ratio on the development of BG reinforced PU scaffold, *AIP Conference Proceedings*, *1791(1)*, 020021.
- [152] **Ryszkowska, J. L., Auguścik, M., Sheikh, A., and Boccaccini, A. R.** (2010). Biodegradable polyurethane composite scaffolds containing Bioglass® for bone tissue engineering, *Composites Science and Technology*, *70(13)*, 1894-1908.
- [153] **Marsich, E., Bellomo, F., Turco, G., Travan, A., Donati, I., and Paoletti, S.** (2013). Nano-composite scaffolds for bone tissue engineering containing silver nanoparticles: preparation, characterization and biological properties, *Journal of Materials Science: Materials in Medicine*, *24(7)*, 1799-1807.
- [154] **Bakare, R., Hawthorne, S., Vails, C., Gugssa, A., Karim, A., Stubbs III, J., and Raghavan, D.** (2016). Antimicrobial and cell viability measurement of bovine serum albumin capped silver nanoparticles (Ag/BSA) loaded collagen immobilized poly (3-hydroxybutyrate-co-3-hydroxyvalerate)(PHBV) film, *Journal of Colloid and Interface Science*, *465*, 140-148.
- [155] **Hasan, A., Waibhaw, G., Saxena, V., and Pandey, L. M.** (2018). Nano-biocomposite scaffolds of chitosan, carboxymethyl cellulose and silver nanoparticle modified cellulose nanowhiskers for bone tissue engineering applications, *International Journal of Biological Macromolecules*, *111*, 923-934.
- [156] **Alt, V., Bechert, T., Steinrücke, P., Wagener, M., Seidel, P., Dingeldein, E., Domann, E., and Schnettler, R.** (2004). An in vitro assessment of the antibacterial properties and cytotoxicity of nanoparticulate silver bone cement, *Biomaterials*, *25(18)*, 4383-4391.
- [157] **Gao, Y., Hassanbhai, A. M., Lim, J., Wang, L., and Xu, C.** (2017). Fabrication of a silver octahedral nanoparticle-containing polycaprolactone nanocomposite for antibacterial bone scaffolds, *RSC Advances*, *7(17)*, 10051-10056.
- [158] **El-Kady, A. M., Rizk, R. A., El-Hady, B. M. A., Shafaa, M. W., and Ahmed, M. M.** (2012). Characterization, and antibacterial properties of novel silver releasing nanocomposite scaffolds fabricated by the gas foaming/salt-leaching technique, *Journal of Genetic Engineering and Biotechnology*, *10(2)*, 229-238.
- [159] **Qi, M. J., Qian, Y. F., Zhao, Y. P., and Ju, W.** (2015). Thermal behavior of electrospun gelatin and chitosan complex, *Thermal Science*, *19(4)*, 1323-1326.

- [160] **Islam, M. S., Rahman, M. M., Gafur, M. A., Mustafa, A. I., and Khan, M. A.** (2014). Preparation and characterization of cellulose-gelatin nanocomposite isolated from jute for biomedical application, *Materials Science*, *11*, 105-112.
- [161] **Sachot, N., Castano, O., Oliveira, H., Marti-Munoz, J., Roguska, A., Amedee, J., Lewandowska, M., Planell, J. A., and Engel, E.** (2016). A novel hybrid nanofibrous strategy to target progenitor cells for cost-effective in situ angiogenesis, *Journal of Materials Chemistry B*, *4*(43), 6967-6978.
- [162] **Lobo, A. O., Afewerki, S., de Paula, M. M. M., Ghannadian, P., Marciano, F. R., Zhang, Y. S., Webster, T. J., and Khademhosseini, A.** (2018). Electrospun nanofiber blend with improved mechanical and biological performance, *International Journal of Nanomedicine*, *13*, 7891.
- [163] **Chahal, S., Hussain, F. S. J., Kumar, A., Yusoff, M. M., and Rasad, M. S. B. A.** (2015). Electrospun hydroxyethyl cellulose nanofibers functionalized with calcium phosphate coating for bone tissue engineering, *RSC Advances*, *5*(37), 29497-29504.
- [164] **Andric, T., Taylor, B. L., Whittington, A. R., and Freeman, J. W.** (2015). Fabrication and characterization of three-dimensional electrospun scaffolds for bone tissue engineering, *Regenerative Engineering and Translational Medicine*, *1*(1-4), 32-41.
- [165] **Shkarina, S., Shkarin, R., Weinhardt, V., Melnik, E., Vacun, G., Kluger, P. J., Loza, K., Eppe, M., Ivlev, S. I., and Baumbach, T.** (2018). 3D biodegradable scaffolds of polycaprolactone with silicate-containing hydroxyapatite microparticles for bone tissue engineering: High-resolution tomography and in vitro study, *Scientific Reports*, *8*(1), 8907.
- [166] **Linh, N. T. B., and Lee, B.-T.** (2012). Electrospinning of polyvinyl alcohol/gelatin nanofiber composites and cross-linking for bone tissue engineering application, *Journal of Biomaterials Applications*, *27*(3), 255-266.
- [167] **De Mori, A., Peña Fernández, M., Blunn, G., Tozzi, G., and Roldo, M.** (2018). 3D printing and electrospinning of composite hydrogels for cartilage and bone tissue engineering, *Polymers*, *10*(3), 285.
- [168] **Seku, K., Reddy Ganapuram, B., Pejjai, B., Mangatayaru Kotu, G., and Golla, N.** (2018). Hydrothermal synthesis of Copper nanoparticles, characterization and their biological applications, *International Journal of Nano Dimension*, *9*(1), 7-14.
- [169] **Tokarek, K., Hueso, J. L., Kuśtrowski, P., Stochel, G., and Kyziol, A.** (2013). Green Synthesis of Chitosan-Stabilized Copper Nanoparticles, *European Journal of Inorganic Chemistry*, *2013*(28), 4940-4947.
- [170] **Sreeju, N., Rufus, A., and Philip, D.** (2016). Microwave-assisted rapid synthesis of copper nanoparticles with exceptional stability and their multifaceted applications, *Journal of Molecular Liquids*, *221*, 1008-1021.

- [171] **Pinto, R. J., Daina, S., Sadocco, P., Neto, C. P., and Trindade, T.** (2013). Antibacterial activity of nanocomposites of copper and cellulose, *BioMed Research International*, 2013, 1-6.
- [172] **Usman, M. S., El Zowalaty, M. E., Shameli, K., Zainuddin, N., Salama, M., and Ibrahim, N. A.** (2013). Synthesis, characterization, and antimicrobial properties of copper nanoparticles, *International Journal of Nanomedicine*, 8, 4467.
- [173] **Villanueva, M. E., del Rosario Diez, A. M. a., González, J. A., Pérez, C. J., Orrego, M., Piehl, L., Teves, S., and Copello, G. J.** (2016). Antimicrobial activity of starch hydrogel incorporated with copper nanoparticles, *ACS Applied Materials & Interfaces*, 8(25), 16280-16288.
- [174] **Dubey, R., Srivastava, P., Kapoor, I., and Singh, G.** (2012). Synthesis, characterization and catalytic behavior of Cu nanoparticles on the thermal decomposition of AP, HMX, NTO and composite solid propellants, Part 83, *Thermochimica Acta*, 549, 102-109.
- [175] **Jinu, U., Gomathi, M., Saiqa, I., Geetha, N., Benelli, G., and Venkatachalam, P.** (2017). Green engineered biomolecule-capped silver and copper nanohybrids using *Prosopis cineraria* leaf extract: enhanced antibacterial activity against microbial pathogens of public health relevance and cytotoxicity on human breast cancer cells (MCF-7), *Microbial Pathogenesis*, 105, 86-95.
- [176] **Olad, A., Alipour, M., and Nosrati, R.** (2017). The use of biodegradable polymers for the stabilization of copper nanoparticles synthesized by chemical reduction method, *Bulletin of Materials Science*, 40(5), 1013-1020.
- [177] **Wu, C., Mosher, B. P., and Zeng, T.** (2006). One-step green route to narrowly dispersed copper nanocrystals, *Journal of Nanoparticle Research*, 8(6), 965-969.
- [178] **Begletsova, N., Selifonova, E., Chumakov, A., Al-Alwani, A., Zakharevich, A., Chernova, R., and Glukhovskoy, E.** (2018). Chemical synthesis of copper nanoparticles in aqueous solutions in the presence of anionic surfactant sodium dodecyl sulfate, *Colloids and Surfaces A: Physicochemical and Engineering Aspects*, 552, 75-80.
- [179] **Regiel-Futyr, A., Dąbrowski, J. M., Mazuryk, O., Śpiewak, K., Kyzioł, A., Pucelik, B., Brindell, M., and Stochel, G.** (2017). Bioinorganic antimicrobial strategies in the resistance era, *Coordination Chemistry Reviews*, 351, 76-117.
- [180] **Musa, A., Ahmad, M. B., Hussein, M. Z., Mohd Izham, S., Shameli, K., and Abubakar Sani, H.** (2016). Synthesis of nanocrystalline cellulose stabilized copper nanoparticles, *Journal of Nanomaterials*, 2016, 2490906.

- [181] **Yallappa, S., Manjanna, J., Sindhe, M., Satyanarayan, N., Pramod, S., and Nagaraja, K.** (2013). Microwave assisted rapid synthesis and biological evaluation of stable copper nanoparticles using T. arjuna bark extract, *Spectrochimica Acta Part A: Molecular and Biomolecular Spectroscopy*, *110*, 108-115.
- [182] **Valodkar, M., Jadeja, R. N., Thounaojam, M. C., Devkar, R. V., and Thakore, S.** (2011). Biocompatible synthesis of peptide capped copper nanoparticles and their biological effect on tumor cells, *Materials Chemistry and Physics*, *128(1-2)*, 83-89.
- [183] **Valodkar, M., Rathore, P. S., Jadeja, R. N., Thounaojam, M., Devkar, R. V., and Thakore, S.** (2012). Cytotoxicity evaluation and antimicrobial studies of starch capped water soluble copper nanoparticles, *Journal of Hazardous Materials*, *201*, 244-249.
- [184] **Shabanzadeh, P., Yusof, R., Shameli, K., and Khanehzaei, H.** (2016). Simulation and modeling of synthesis Cu nanoparticles in sodium alginate media by means of expert systems, *Research on Chemical Intermediates*, *42(4)*, 2831-2843.
- [185] **Gutiérrez, J. A., Caballero, S., Díaz, L. A., Guerrero, M. A., Ruiz, J., and Ortiz, C. C.** (2018). High antifungal activity against Candida species of monometallic and bimetallic nanoparticles synthesized in nanoreactors, *ACS Biomaterials Science & Engineering*, *4(2)*, 647-653.
- [186] **Bonilla, J. J. A., Guerrero, D. J. P., Suárez, C. I. S., López, C. C. O., and Sáez, R. G. T.** (2015). In vitro antifungal activity of silver nanoparticles against fluconazole-resistant Candida species, *World Journal of Microbiology and Biotechnology*, *31(11)*, 1801-1809.
- [187] **Gómez-Sequeda, N., Torres, R., and Ortiz, C.** (2017). Synthesis, characterization, and in vitro activity against Candida spp. of fluconazole encapsulated on cationic and conventional nanoparticles of poly (lactic-co-glycolic acid), *Nanotechnology, Science and Applications*, *10*, 95.
- [188] **Jia, B., Mei, Y., Cheng, L., Zhou, J., and Zhang, L.** (2012). Preparation of copper nanoparticles coated cellulose films with antibacterial properties through one-step reduction, *ACS Applied Materials & Interfaces*, *4(6)*, 2897-2902.
- [189] **Cioffi, N., Torsi, L., Ditaranto, N., Sabbatini, L., Zambonin, P. G., Tantillo, G., Ghibelli, L., D'Alessio, M., Bleve-Zacheo, T., and Traversa, E.** (2004). Antifungal activity of polymer-based copper nanocomposite coatings, *Applied Physics Letters*, *85(12)*, 2417-2419.
- [190] **Ray, D., Pramanik, S., Mandal, R. P., Chaudhuri, S., and De, S.** (2015). Sugar-mediated 'green' synthesis of copper nanoparticles with high antifungal activity, *Materials Research Express*, *2(10)*, 105002.
- [191] **Cioffi, N., Torsi, L., Ditaranto, N., Tantillo, G., Ghibelli, L., Sabbatini, L., Bleve-Zacheo, T., D'Alessio, M., Zambonin, P. G., and Traversa, E.** (2005). Copper nanoparticle/polymer composites with antifungal and bacteriostatic properties, *Chemistry of Materials*, *17(21)*, 5255-5262.

- [192] **Wei, Y., Chen, S., Kowalczyk, B., Huda, S., Gray, T. P., and Grzybowski, B. A.** (2010). Synthesis of stable, low-dispersity copper nanoparticles and nanorods and their antifungal and catalytic properties, *The Journal of Physical Chemistry C*, 114(37), 15612-15616.
- [193] **Tantubay, S., Mukhopadhyay, S. K., Kalita, H., Konar, S., Dey, S., Pathak, A., and Pramanik, P.** (2015). Carboxymethylated chitosan-stabilized copper nanoparticles: a promise to contribute a potent antifungal and antibacterial agent, *Journal of Nanoparticle Research*, 17(6), 243.
- [194] **Musa, A., Ahmad, M. B., Hussein, M. Z., Saiman, M. I., and Sani, H. A.** (2016). Effect of gelatin-stabilized copper nanoparticles on catalytic reduction of methylene blue, *Nanoscale Research Letters*, 11(1), 438.
- [195] **Mallick, S., Sanpui, P., Ghosh, S. S., Chattopadhyay, A., and Paul, A.** (2015). Synthesis, characterization and enhanced bactericidal action of a chitosan supported core-shell copper-silver nanoparticle composite, *RSC Advances*, 5(16), 12268-12276.
- [196] **Mallick, S., Sharma, S., Banerjee, M., Ghosh, S. S., Chattopadhyay, A., and Paul, A.** (2012). Iodine-stabilized Cu nanoparticle chitosan composite for antibacterial applications, *ACS Applied Materials & Interfaces*, 4(3), 1313-1323.
- [197] **Megarajan, S., Vidhyalakshmi, M., Ahmed, K. B. A., Murali, V., Niranjani, B. R., Saisubramanian, N., and Anbazhagan, V.** (2016). N-lauryltyramine capped copper nanoparticles exhibit a selective colorimetric response towards hazardous mercury (II) ions and display true anti-biofilm and efflux pump inhibitory effects in E. coli, *RSC Advances*, 6(90), 87513-87522.
- [198] **Rastogi, L., and Arunachalam, J.** (2013). Synthesis and characterization of bovine serum albumin-copper nanocomposites for antibacterial applications, *Colloids and Surfaces B: Biointerfaces*, 108, 134-141.
- [199] **Bashir, O., Hussain, S., AL-Thabaiti, S. A., and Khan, Z.** (2015). Synthesis, optical properties, stability, and encapsulation of Cu-nanoparticles, *Spectrochimica Acta Part A: Molecular and Biomolecular Spectroscopy*, 140, 265-273.
- [200] **Singh, M., Sinha, I., Premkumar, M., Singh, A., and Mandal, R.** (2010). Structural and surface plasmon behavior of Cu nanoparticles using different stabilizers, *Colloids and Surfaces A: Physicochemical and Engineering Aspects*, 359(1-3), 88-94.
- [201] **Pourbeyram, S., and Mohammadi, S.** (2014). Synthesis and characterization of highly stable and water dispersible hydrogel-copper nanocomposite, *Journal of Non-Crystalline Solids*, 402, 58-63.
- [202] **Díaz-Visurraga, J., Daza, C., Pozo, C., Becerra, A., von Plessing, C., and García, A.** (2012). Study on antibacterial alginate-stabilized copper nanoparticles by FT-IR and 2D-IR correlation spectroscopy, *International Journal of Nanomedicine*, 7, 3597.

- [203] **Valdez, J., and Gómez, I.** (2016). One-Step Green Synthesis of Metallic Nanoparticles Using Sodium Alginate, *Journal of Nanomaterials*, 2016, 9790345.
- [204] **Thakore, S. I.** (2012). Role of Biopolymers in Green Nanotechnology, Products and Applications of Biopolymers, Casparus Johannes Reinhard Verbeek, IntechOpen, DOI: 10.5772/35553. Retrieved from: <https://www.intechopen.com/books/products-and-applications-of-biopolymers/role-of-biopolymers-in-green-nanotechnology>.
- [205] **Khan, A., Rashid, A., Younas, R., and Chong, R.** (2016). A chemical reduction approach to the synthesis of copper nanoparticles, *International Nano Letters*, 6(1), 21-26.
- [206] **Prabhu, B. M., Ali, S. F., Murdock, R. C., Hussain, S. M., and Srivatsan, M.** (2010). Copper nanoparticles exert size and concentration dependent toxicity on somatosensory neurons of rat, *Nanotoxicology*, 4(2), 150-160.
- [207] **Lee, I.-C., Ko, J.-W., Park, S.-H., Lim, J.-O., Shin, I.-S., Moon, C., Kim, S.-H., Heo, J.-D., and Kim, J.-C.** (2016). Comparative toxicity and biodistribution of copper nanoparticles and cupric ions in rats, *International Journal of Nanomedicine*, 11, 2883.
- [208] **Song, L., Connolly, M., Fernández-Cruz, M. L., Vijver, M. G., Fernández, M., Conde, E., de Snoo, G. R., Peijnenburg, W. J., and Navas, J. M.** (2014). Species-specific toxicity of copper nanoparticles among mammalian and piscine cell lines, *Nanotoxicology*, 8(4), 383-393.
- [209] **Alizadeh, S., Seyedalipour, B., Shafieyan, S., Kheime, A., Mohammadi, P., and Aghdami, N.** (2019). Copper nanoparticles promote rapid wound healing in acute full thickness defect via acceleration of skin cell migration, proliferation, and neovascularization, *Biochemical and Biophysical Research Communications*, 517(4), 684-690.
- [210] **Auffan, M., Rose, J., Bottero, J.-Y., Lowry, G. V., Jolivet, J.-P., and Wiesner, M. R.** (2009). Towards a definition of inorganic nanoparticles from an environmental, health and safety perspective, *Nature Nanotechnology*, 4(10), 634.
- [211] **Chen, Z., Meng, H., Xing, G., Chen, C., Zhao, Y., Jia, G., Wang, T., Yuan, H., Ye, C., and Zhao, F.** (2006). Acute toxicological effects of copper nanoparticles in vivo, *Toxicology Letters*, 163(2), 109-120.
- [212] **Eliza, M., Shahrudin, M., Noormaziah, J., and Rosli, W. W.** (2015). Carboxymethyl cellulose (CMC) from oil palm empty fruit bunch (OPEFB) in the new solvent dimethyl sulfoxide (DMSO)/tetrabutylammonium fluoride (TBAF), *Journal of Physics: Conference Series*, 622, 012026.
- [213] **Judawisastra, H., Sitohang, R., and Marta, L.** (2017). Water absorption and its effect on the tensile properties of tapioca starch/polyvinyl alcohol bioplastics. *IOP Conference Series: Materials Science and Engineering*, 223, 012066.

- [214] **Sawant, S. S., Bhagwat, A. D., and Mahajan, C. M.** (2016). Novel Facile Technique for Synthesis of Stable Cuprous Oxide (Cu₂O) Nanoparticles—an Ageing Effect, *Journal of Nano- and Electronic Physics*, 8(1), 01036.
- [215] **Kouti, M., and Matouri, L.** (2010). Fabrication of nanosized cuprous oxide using fehling's solution, *Scientia Iranica*, 17(1), 73.
- [216] **Badawy, S. M., El Khashab, R., and Nayl, A.** (2015). Synthesis, characterization and catalytic activity of Cu/Cu₂O nanoparticles prepared in aqueous medium, *Bulletin of Chemical Reaction Engineering & Catalysis*, 10(2), 169-174.
- [217] **Murtaza, M., Hussain, N., Ya, H., and Wu, H.** (2019). High purity copper nanoparticles via sonoelectrochemical approach, *Materials Research Express*, 6(11), 115058.
- [218] **El-Batal, A. I., Al-Hazmi, N. E., Mosallam, F. M., and El-Sayyad, G. S.** (2018). Biogenic synthesis of copper nanoparticles by natural polysaccharides and *Pleurotus ostreatus* fermented fenugreek using gamma rays with antioxidant and antimicrobial potential towards some wound pathogens, *Microbial Pathogenesis*, 118, 159-169.
- [219] **Rasool, U., Sah, S. K., and Hemalatha, S.** (2019). Effect of biosynthesized copper nanoparticles (Cu NPs) on the growth and biofilm formation of fluconazole-resistant *Candida Albicans*, *Journal of Microbiology, Biotechnology & Food Sciences*, 9(1), 21-24.
- [220] **Beltrán-Partida, E., Valdez-Salas, B., Valdez-Salas, E., Pérez-Cortéz, G., and Nedev, N.** (2019). Synthesis, Characterization, and In Situ Antifungal and Cytotoxicity Evaluation of Ascorbic Acid-Capped Copper Nanoparticles, *Journal of Nanomaterials*, 2019, 5287632.
- [221] **Kruk, T., Szczepanowicz, K., Stefańska, J., Socha, R. P., and Warszyński, P.** (2015). Synthesis and antimicrobial activity of monodisperse copper nanoparticles, *Colloids and Surfaces B: Biointerfaces*, 128, 17-22.
- [222] **Bogdanović, U., Dimitrijević, S., Škapin, S. D., Popović, M., Rakočević, Z., Leskovic, A., Petrović, S., Stoiljković, M., and Vodnik, V.** (2018). Copper-polyaniline nanocomposite: Role of physicochemical properties on the antimicrobial activity and genotoxicity evaluation, *Materials Science and Engineering: C*, 93, 49-60.
- [223] **Sheikh, F. A., Barakat, N. A., Kanjwal, M. A., Nirmala, R., Lee, J. H., Kim, H., and Kim, H. Y.** (2010). Electrospun titanium dioxide nanofibers containing hydroxyapatite and silver nanoparticles as future implant materials, *Journal of Materials Science: Materials in Medicine*, 21(9), 2551-2559.
- [224] **Kouhi, M., Morshed, M., Varshosaz, J., and Fathi, M. H.** (2013). Poly (ϵ -caprolactone) incorporated bioactive glass nanoparticles and simvastatin nanocomposite nanofibers: preparation, characterization and in vitro drug release for bone regeneration applications, *Chemical Engineering Journal*, 228, 1057-1065.

- [225] **Kim, H. W., Lee, H. H., and Chun, G. S.** (2008). Bioactivity and osteoblast responses of novel biomedical nanocomposites of bioactive glass nanofiber filled poly (lactic acid), *Journal of Biomedical Materials Research Part A*, 85(3), 651-663.
- [226] **Li, Q., Ge, L., Wan, W., Jiang, J., Zhong, W., Ouyang, J., and Xing, M.** (2015). Magnetically guided fabrication of multilayered iron oxide/polycaprolactone/gelatin nanofibrous structures for tissue engineering and theranostic application, *Tissue Engineering Part C: Methods*, 21(10), 1015-1024.
- [227] **Lin, H.-M., Lin, Y.-H., and Hsu, F.-Y.** (2012). Preparation and characterization of mesoporous bioactive glass/polycaprolactone nanofibrous matrix for bone tissues engineering, *Journal of Materials Science: Materials in Medicine*, 23(11), 2619-2630.
- [228] **Yunos, D., Ahmad, Z., and Boccaccini, A.** (2010). Fabrication and characterization of electrospun poly-DL-lactide (PDLA) fibrous coatings on 45S5 Bioglass® substrates for bone tissue engineering applications, *Journal of Chemical Technology and Biotechnology*, 85(6), 768-774.
- [229] **Castaño, O., Sachot, N. g., Xuriguera, E., Engel, E., Planell, J. A., Park, J.-H., Jin, G.-Z., Kim, T.-H., Kim, J.-H., and Kim, H.-W.** (2014). Angiogenesis in bone regeneration: tailored calcium release in hybrid fibrous scaffolds, *ACS Applied Materials & Interfaces*, 6(10), 7512-7522.
- [230] **Fernandes, J. S., Gentile, P., Martins, M., Neves, N. M., Miller, C., Crawford, A., Pires, R. A., Hatton, P., and Reis, R. L.** (2016). Reinforcement of poly-L-lactic acid electrospun membranes with strontium borosilicate bioactive glasses for bone tissue engineering, *Acta Biomaterialia*, 44, 168-177.
- [231] **Jo, J. H., Lee, E. J., Shin, D. S., Kim, H. E., Kim, H. W., Koh, Y. H., and Jang, J. H.** (2009). In vitro/in vivo biocompatibility and mechanical properties of bioactive glass nanofiber and poly (ϵ -caprolactone) composite materials, *Journal of Biomedical Materials Research Part B: Applied Biomaterials*, 91(1), 213-220.
- [232] **Santocildes-Romero, M. E., Goodchild, R. L., Hatton, P. V., Crawford, A., Reaney, I. M., and Miller, C. A.** (2016). Preparation of Composite Electrospun Membranes Containing Strontium-Substituted Bioactive Glasses for Bone Tissue Regeneration, *Macromolecular Materials and Engineering*, 301(8), 972-981.
- [233] **Singh, B., and Pramanik, K.** (2017). Development of novel silk fibroin/polyvinyl alcohol/sol-gel bioactive glass composite matrix by modified layer by layer electrospinning method for bone tissue construct generation, *Biofabrication*, 9(1), 015028.
- [234] **Hafezi, M., Safarian, S., Khorasani, M. T., and Osman, N. A. A.** (2016). Polyurethane/58S bioglass nanofibers: synthesis, characterization, and in vitro evaluation, *RSC Advances*, 6(42), 35815-35824.

- [235] **Palza, H., Galarce, N., Bejarano, J., Beltran, M., and Caviedes, P.** (2017). Effect of copper nanoparticles on the cell viability of polymer composites, *International Journal of Polymeric Materials and Polymeric Biomaterials*, 66(9), 462-468.
- [236] **Akturk, A., Karbancıoğlu Güler, F., Erol Taygun, M., Goller, G., and Küçükbayrak, S.** (2020). Synthesis and antifungal activity of soluble starch and sodium alginate capped copper nanoparticles, *Materials Research Express*, 6, 12.
- [237] **Onyekwere, O., Odiakaose, C., and Uyanga, K.** (2017). Multi Response Optimization of the Functional Properties of Rubber Seed–Shear Butter Based Core Oil Using D-Optimal Mixture Design, *Archives of Foundry Engineering*, 17(4), 207-223.
- [238] **Ghelich, R., Jahannama, M. R., Abdizadeh, H., Torknik, F. S., and Vaezi, M. R.** (2019). Central composite design (CCD)-Response surface methodology (RSM) of effective electrospinning parameters on PVP-B-Hf hybrid nanofibrous composites for synthesis of HfB₂-based composite nanofibers, *Composites Part B: Engineering*, 166, 527-541.
- [239] **Nezarati, R. M., Eifert, M. B., and Cosgriff-Hernandez, E.** (2013). Effects of humidity and solution viscosity on electrospun fiber morphology, *Tissue Engineering Part C: Methods*, 19(10), 810-819.
- [240] **Koh, W., Uthumporn, U., Rosma, A., Irfan, A., and Park, Y.** (2018). Optimization of a fermented pumpkin-based beverage to improve *Lactobacillus mali* survival and α -glucosidase inhibitory activity: A response surface methodology approach, *Food Science and Human Wellness*, 7(1), 57-70.
- [241] **Lu, Y., Li, L., Zhu, Y., Wang, X., Li, M., Lin, Z., Hu, X., Zhang, Y., Yin, Q., and Xia, H.** (2018). Multifunctional copper-containing carboxymethyl chitosan/alginate scaffolds for eradicating clinical bacterial infection and promoting bone formation, *ACS Applied Materials & Interfaces*, 10(1), 127-138.
- [242] **Zheng, K., Dai, X., Lu, M., Hüser, N., Taccardi, N., and Boccaccini, A. R.** (2017). Synthesis of copper-containing bioactive glass nanoparticles using a modified Stöber method for biomedical applications, *Colloids and Surfaces B: Biointerfaces*, 150, 159-167.
- [243] **Baino, F., Potestio, I., and Vitale-Brovarone, C.** (2018). Production and physicochemical characterization of Cu-doped silicate bioceramic scaffolds, *Materials*, 11(9), 1524.
- [244] **Zhao, S., Li, L., Wang, H., Zhang, Y., Cheng, X., Zhou, N., Rahaman, M. N., Liu, Z., Huang, W., and Zhang, C.** (2015). Wound dressings composed of copper-doped borate bioactive glass microfibers stimulate angiogenesis and heal full-thickness skin defects in a rodent model, *Biomaterials*, 53, 379-391.

- [245] **Wang, X., Cheng, F., Liu, J., Smått, J.-H., Gepperth, D., Lastusaari, M., Xu, C., and Hupa, L.** (2016). Biocomposites of copper-containing mesoporous bioactive glass and nanofibrillated cellulose: Biocompatibility and angiogenic promotion in chronic wound healing application, *Acta Biomaterialia*, 46, 286-298.
- [246] **Erol, M., Mouriño, V., Newby, P., Chatzistavrou, X., Roether, J., Hupa, L., and Boccaccini, A. R.** (2012). Copper-releasing, boron-containing bioactive glass-based scaffolds coated with alginate for bone tissue engineering, *Acta Biomaterialia*, 8(2), 792-801.





CURRICULUM VITAE

Name Surname : Ayşen Aktürk
Place and Date of Birth : İstanbul /February 1984
E-Mail : akturkay@itu.edu.tr

EDUCATION

- **B.Sc.** : 2008, Istanbul University, Faculty of Engineering, Chemical Engineering Department
- **M.Sc.** : 2011 Istanbul Technical University, Chemical and Metallurgical Faculty, Chemical Engineering Department

PROFESSIONAL EXPERIENCE AND REWARDS:

- 2010-date Chemical Engineer at Istanbul Technical University.
- 2009-2010 Quality Control and Laboratory Engineer at Koroza Packaging

PUBLICATIONS, PRESENTATIONS AND PATENTS ON THE THESIS:

- **Aktürk, A.,** Erol Taygun, M., Karbancıoğlu Güler, F., Göller, G., and Küçükbayrak, S. (2019). Fabrication of Antibacterial Polyvinylalcohol Nanocomposite Mats with Soluble Starch Coated Silver Nanoparticles. *Colloids and Surfaces A: Physicochemical and Engineering Aspects*, 562, 255-262.
- **Akturk, A.,** Erol Taygun, M., and Goller G. (2020). Optimization of The Electrospinning Process Variables For Gelatin/ Silver Nanoparticle/Bioactive Glass Nanocomposites for Bone Tissue Engineering. *Polymer Composites*, 41(6), 2411-2425.

- **Aktürk, A.,** Karbancıoğlu Güler, F., Erol Taygun, M., Goller, G., and Küçükbayrak, S. (2020). Synthesis and antifungal activity of soluble starch and sodium alginate capped copper nanoparticles. *Materials Research Express*, 6, 12.
- **Aktürk A., Erol Taygun M., Göller G., and Küçükbayrak S.,** 2016: Green Synthesis of Silver Nanoparticles by Statistical Experimental Design, Proceedings of the World Congress on Recent Advances in Nanotechnology (RAN'16), April 1-2, 2016 Prag, Czech Republic.
- **Aktürk A.,** Erol Taygun M., Göller G., and Küçükbayrak S., 2016: Nanocomposite Materials Containing Metal Nanoparticles for Tissue Engineering Applications, 18th International Metallurgy and Materials Congress 29 Sept. - 01 Oct. 2016, İstanbul, Turkey.
- **Aktürk A.,** Erol Taygun M., Göller G., and Küçükbayrak S., 2017: Fibrous Nanocomposite Scaffolds Containing Biopolymer Capped Silver Nanoparticles, International Porous Powder Materials, September 12-15th, 2017, Kuşadası, Aydın.
- **Aktürk A.,** Erol Taygun M., Göller G., and Küçükbayrak S., 2017: An Optimization Study To Fabricate Fibrous Nanocomposite Scaffolds Containing Silver Nanoparticles And Bioactive Glass, International Commission on Glass Annual Meeting and & 32nd Şişecam Glass Symposium, October 22-25th 2017, İstanbul, Turkey.
- **Aktürk A.,** Erol Taygun M., Göller G., and Küçükbayrak S, 2017 :Study on alginate and soluble starch capped silver nanoparticles obtained by using green synthesis, International Materials Technologies and Metallurgy Conference 2017 (MTM 2017), October 26-27, 2017, İstanbul, Turkey.

OTHER PUBLICATIONS, PRESENTATIONS AND PATENTS:

- Gönen, S. Ö., Erol Taygun, M., **Aktürk, A.,** and Küçükbayrak, S. (2016). Fabrication of nanocomposite mat through incorporating bioactive glass particles into gelatin/poly (ϵ -caprolactone) nanofibers by using Box–Behnken design, *Materials Science and Engineering: C*, 67, 684-693.
- Ozyuguran, A., **Aktürk, A.,** and Yaman, S. (2018). Optimal use of condensed parameters of ultimate analysis to predict the calorific value of biomass, *Fuel*, 214, 640-646.
- **Aktürk, A.,** Cenik, B., Aydoğdu, Z., Taygun, M. E., Güler, F. K., and Küçükbayrak, S. Fabrication and Characterization of Polyvinyl Alcohol/Gelatin/Silver Nanoparticle Nanocomposite Materials, *Eurasian Journal of Biological and Chemical Sciences*, 2(1), 1-6.
- **Aktürk, A.,** Tunca, N. Keskin, İ., Erol Taygun, M., Küçükbayrak, S. (2017): Fabrication of Nanocomposite Scaffolds Including Metal Nanoparticles In Tissue Engineering, International Materials Technologies and Metallurgy Conference 2017 (MTM 2017), October 26-27, 2017, İstanbul, Turkey.

- **Aktürk, A.**, Alemdar, Ç. Ekmen, E., Erol Taygun, M., Küçükbayrak, S. (2017): Nanocomposite Scaffolds Containing Metal Nanoparticles, International Materials Technologies and Metallurgy Conference 2017 (MTM 2017), October 26-27, 2017 İstanbul, Turkey.
- **Aktürk, A.**, Yetiş, Ö., Gül, S., Erol Taygun, M. and Küçükbayrak, S. (2018): Fabrication of ZnO Doped Gelatin/Alginate Nanofibers for Wound Dressing Applications, 5th International Conference on Materials Science and Nanotechnology For Next Generation (MSNG-2018) October 4-6, 2018, Cappadocia, Turkey.
- Kabak, Ö, **Aktürk, A.**, Erol Taygun, M, Küçükbayrak, S. (2018) The determination of photocatalytic and antibacterial performance of nanocomposite membranes doped with silver nanoparticles, 5th International Conference on Small and Decentralized Water and Waste Water Treatment Plants (SWAT 2018) August 26-29, 2018, Thessaloniki, Greece.
- Kabak, Ö, **Aktürk, A.**, Erol Taygun, M, Küçükbayrak, S. (2018). An Optimization Study for Photocatalytic and Antibacterial Nanocomposite TiO₂ Membranes Doped with Silver Nanoparticles, *International Symposium on Urban Water and Wastewater Management Proceedings Book*, 1115-1122.
- **Akturk, A.**, Yıldız, T., Erol Taygun, E., Küçükbayrak, S., (2019). Production of Nanoscaled Bioactive Glasses Doped with Silver, *The Proceedings of the 4th International Porous and Powder Materials Symposium and Exhibition (PPM 2019)*, 216-221.
- Kadakal, T., **Akturk, A.**, Karbancıoğlu Güler, F., Erol Taygun, E., Küçükbayrak, S. (2019). Production of Skin Mask Containing Vitamin A and Silver Nanoparticles, *International Materials Technologies and Metallurgy Conference Proceeding Book*, 158-161.
- **Akturk, A.**, Yıldız, T., Karbancıoğlu Güler, F., Erol Taygun, E., Küçükbayrak, S. (2019). Fabrication Of Nanofiber Scaffolds Doped with Nanoscaled Bioactive Glasses, *International Materials Technologies and Metallurgy Conference Proceeding Book*, 284-287.
- Erkoç, Ç., **Akturk, A.**, Karbancıoğlu Güler, F., Erol Taygun, E., Küçükbayrak, S. (2019). Fabrication And Characterization of Biopolymer/Salicylic Acid//ZnO Nanoparticle Multi Functional Nanofiber Material, *International Materials Technologies and Metallurgy Conference Proceeding Book*, 106-109.
- Dikmetaş, D. N., Gök, H., **Akturk, A.**, Karbancıoğlu Güler, F., Erol Taygun, E., Küçükbayrak, S. Fabrication PVA/Alginate Nanofibers Containing Zinc And Silver Nanoparticles For Wound Dressing Applications, *International Materials Technologies and Metallurgy Conference Proceeding Book*, 131-135.